Doklady Physics, Vol. 48, No. 3, 2003, pp. 103–104. Translated from Doklady Akademii Nauk, Vol. 389, No. 1, 2003, pp. 36–37.

PHYSICS

Modified Darcy Laws Allowing for Electromagnetic Fields

Kh. Kh. Imomnazarov

Presented by Academician A.S. Alekseev October 18, 2002

Received November 4, 2002

1. INTRODUCTION

The study of properties of conducting-fluid flows through a porous medium in the presence of an electromagnetic field involves a wide scope of scientific and technological knowledge, including earth science [1], biological mechanics [2], metallurgy [3, 4], etc.

In [5], the effect of a magnetic field on the filtration law in porous media was experimentally discovered. In [1], a modified Darcy law was obtained by introducing the Lorenz force into the right-hand side of the filtration law:

$$\mathbf{v} = \frac{k}{\tilde{\mu}}(-\nabla p + [\mathbf{J}, \mathbf{B}]). \tag{1}$$

Here, $\mathbf{v}$ is the velocity of a conducting fluid, $\mathbf{J}$ is the electric-current density, p is the pore pressure, $\mathbf{B}$ is the magnetic-field induction; k is the permeability, and $\tilde{\mu}$ is the viscosity of the fluid.

As is known to the author of the present paper, there exist three forms of modified Darcy law and Ohm's law that allow electrokinetic phenomena in porous media to be described. The first group of studies [6–10] propose to write out modified Darcy law and Ohm's law in the form

$$\mathbf{v} = -\frac{k}{\tilde{\mu}}\nabla p - L_1\nabla\phi, \tag{2}$$

$$\mathbf{J} = -L_2\nabla p - \sigma_l\nabla\phi. \tag{3}$$

The second group [11, 12] uses the following form of modified Darcy law and Ohm's law:

$$\mathbf{v} = -\frac{k}{\tilde{\mu}}\nabla p + L_1\mathbf{E}, \tag{4}$$

$$\mathbf{J} = L_2\nabla p + d_0\sigma_l\mathbf{E}. \tag{5}$$

Institute of Computational Mathematics and Mathematical Geophysics, Siberian Division, Russian Academy of Sciences, pr. Akademika Lavrent'eva 6, Novosibirsk, 630090 Russia
e-mail: imom@omzg.sscc.ru

The third group of studies [13] suggests a modified Darcy law and Ohm's law (in the isotropic case) in the form

$$\mathbf{v} = -\frac{k}{\tilde{\mu}}\nabla p + L_1\nabla\phi, \tag{6}$$

$$\mathbf{J} = L_2\nabla p - \sigma_l\nabla\phi. \tag{7}$$

In formulas (2)–(7), ϕ is the potential of the electric field $\mathbf{E}$; L_1 and L_2 are phenomenological coefficients; and σ_l is the conductivity of a fluid. The terms containing L_1 and L_2 are responsible for the electrokinetic effect. Based on the Onsager reciprocal relation, the authors of [14] assume

$$L_1 = L_2. \tag{8}$$

In the present paper, we show that equality (8) is invalid and establish thermodynamically consistent modified Darcy laws in the presence of electromagnetic fields.

2. THE GENERALIZED DARCY LAW WITH ALLOWANCE FOR MAGNETIC FIELD

We now consider the simplest situation with due regard to only kinetic processes associated with the energy loss related to the friction coefficient χ. In this case, we completely ignore quadratic effects with respect to the velocity. The equation of motion for a conducting fluid has the form [15]

$$\frac{\partial\mathbf{v}}{\partial t} = -\frac{\nabla p}{\rho} - \chi\rho_l(\mathbf{v} - \mathbf{u}) + \frac{\sigma_l}{\sigma\rho_l}[\mathbf{J}, \mathbf{B}]. \tag{9}$$

Here, $\mathbf{u}$ is the velocity of a conducting porous body possessing the conductivity σ_s; $\sigma = \sigma_l + \sigma_s$; $\rho = \rho_l + \rho_s$, ρ_l and ρ_s are the partial densities of the conducting fluid and a conducting elastic porous body, respectively.

In the time-independent case, $\dot{\mathbf{v}} = \mathbf{u} = 0$. In this case, the velocity of a conducting fluid is determined from the equation

$$\mathbf{v} = \frac{1}{\chi\rho\rho_l}\left(-\nabla p + \frac{\rho}{\rho_l}\frac{\sigma_l}{\sigma}[\mathbf{J}, \mathbf{B}]\right).$$

1028-3358/03/4803-0103$24.00

From here, with allowance for $\chi\rho\rho_l = \frac{\tilde{\mu}}{k}$ [15], we arrive at the modified Darcy law that takes the magnetic field into account:

$$\mathbf{v} = \frac{k}{\tilde{\mu}}\left(-\nabla p + \frac{\rho}{\rho_l}\frac{\sigma_l}{\sigma}[\mathbf{J}, \mathbf{B}]\right).$$

Comparing this formula with relationship (1), we can see that, on the right-hand side, the Lorenz force is added with a weight factor equal to

$$\frac{\frac{\rho_s}{\rho_l} + 1}{\frac{\sigma_s}{\sigma_l} + 1}.$$

3. THE GENERALIZED DARCY LAW WITH ALLOWANCE FOR ELECTRIC FIELD

We now consider the case when the production of the entropy in the system depends only on the kinetic coefficients χ of friction and σ of diffusion, as well as on the electrokinetic coefficient γ. In the linear approximation, the equations of motion for a fluid and the electric-current density in the steady-state mode ($\dot{\mathbf{v}} = \mathbf{u} = 0$, $\mathbf{B} = 0$) have the form

$$\rho_l \mathbf{v} = -\frac{\nabla p}{\chi\rho} - \frac{\gamma}{\chi}\mathbf{E}, \tag{10}$$

$$\mathbf{J} = \gamma\rho_l \mathbf{v} + \sigma\mathbf{E}, \tag{11}$$

where $\mathbf{E}$ is the intensity of the electric field. In this case, the kinetic coefficients χ, σ, and γ satisfy the inequality [14, 15]

$$\sigma\chi - \gamma^2 > 0.$$

Substituting Eq. (10) into Eq. (11), we obtain

$$\mathbf{J} = -\frac{\gamma}{\chi\rho}\nabla p + \frac{\sigma\chi - \gamma^2}{\chi}\mathbf{E}.$$

From this formula and formula (10) with allowance for $\mathbf{E} = -\nabla\phi$ we arrive at the modified Darcy law and Ohm's law stipulated by the electrokinetic coefficient γ:

$$\mathbf{v} = -\frac{\nabla p}{\chi\rho\rho_l} + \frac{\gamma}{\chi\rho_l}\nabla\phi, \tag{12}$$

$$\mathbf{J} = -\frac{\gamma}{\chi\rho}\nabla p - \frac{\sigma\chi - \gamma^2}{\chi}\nabla\phi. \tag{13}$$

It is worth noting that, in contrast to the cross phenomenological coefficients suggested previously in [2, 6–13], those entering into the modified Darcy law and Ohm's law are not equal to each other. Moreover, as distinct from [2, 6–13], the coefficients in the definition of the electric-current density depend on the friction factor (permeability and viscosity of a fluid) and on the partial densities of both a conducting elastic porous body and a conducting fluid. When the electrokinetic coefficient disappears, formulas (12) and (13) are transformed into the well-known Darcy law and Ohm law's, respectively.

ACKNOWLEDGMENTS

The author is grateful to V. N. Dorovskiĭ for fruitful discussions of this paper.

This work was supported by the Russian Foundation for Basic Research, project no. 02-05-64939, and Novosibirsk regional administration.

REFERENCES

1. N. Rudraiah, B. K. Ramaiah, and B. M. Rajasekhar, Int. J. Eng. Sci. **13**, 1 (1975).
2. M. E. Levenston, E. H. Frank, and A. J. Grodzinsky, J. Appl. Mech. **66**, 323 (1999).
3. P. J. Prescott and F. P. Incropera, J. Heat Transfer **115**, 302 (1993).
4. P. Lehmann, R. Moreau, D. Camel, and T. Bolcato, Acta Mater. **46**, 1067 (1998).
5. J. McWhirter, M. Crawford, and D. Klein, Fusion Technol. **34**, 187 (1998).
6. B. Nourbehecht, *Irreversible Thermodynamic Effects in Inhomogeneous Media and Their Application in Certain Geoelectric Problems*, PhD Thesis (Mass. Inst. of Technol., Cambridge, Mass., 1963).
7. C. L. Carnahan, Tech. Rep. Univ. Nevada, Ser. Hydrology and Water Resources **24** (1975).
8. D. V. Fitterman, J. Geophys. Res. **83**, 5923 (1978).
9. T. Ishido, J. Geotherm. Res. Soc. Jpn. **3**, 87 (1981).
10. S. R. Pride, Phys. Rev. B **50** (21), 15678 (1994).
11. N. I. Migunov, Izv. Akad. Nauk SSSR, Fiz. Zemli, No. 5, 52 (1978).
12. V. N. Nikolaevskiĭ, *Geomechanics and Fluid Dynamics with Application to Problems of Gas and Oil Beds* (Nedra, Moscow, 1996).
13. E. H. Frank and A. J. Grodzinsky, J. Biomech. **20**, 629 (1987).
14. S. R. de Groot and P. Mazur, *Nonequilibrium Thermodynamics* (North-Holland, Amsterdam, 1962; Mir, Moscow, 1964).
15. V. N. Dorovsky and H. H. Imomnazarov, Math. Comput. Model. **20** (7), 91 (1994).

Translated by G. Merzon

Doklady Physics, Vol. 48, No. 3, 2003, pp. 105–107. Translated from Doklady Akademii Nauk, Vol. 389, No. 1, 2003, pp. 38–40.

PHYSICS

Rotation of the Speckle Pattern in an Absorbing Optical Fiber When Changing the Circular-Polarization Sign of Propagating Light

N. R. Sadykov

Presented by Academician V.V. Osiko August 24, 2002

Received August 23, 2002

In this paper, the effect of the rotation of the speckle pattern for circularly polarized light outgoing from a low-mode optical fiber is predicted for the case when the sign of the T circular polarization changes. It is shown that, for a spin particle with a nonzero mass, the effect is caused by the spin–orbit interaction. For an optical-fiber waveguide, the absorption coefficient and the gamma-radiation T dose necessary for obtaining this absorption coefficient are determined.

Recently, a number of unique polarization effects depending on the photon helicity have been predicted and experimentally observed. Among them, we should mention the Magnus optical effect [1–4], the effect of the Barry topological phase for a photon [5, 6], the Rytov–Vladimirskiĭ effect [7, 8], and the effect of the speckle-pattern rotation for a T twisted multimode optical fiber [9, 10].

In this paper, we predict a new effect close to those listed in [1–10]. This is the rotation of the speckle pattern in the absorbing optical fiber when the sign of the circular polarization is reversed. In contrast to the Magnus optical effect, for the effect under consideration, the magnitude of the speckle-pattern rotation when changing the sign of the circular polarization $\sigma = \pm 1$ is proportional to the optical-fiber length z squared.

In the wave description, the allowance for the polarization contribution H grad(div**E**) in the scalar wave equation results (for a multimode optical fiber with an insignificant absorption) in rotation of the speckle pattern under the change in the sign of σ [1, 2].

We now consider an optical fiber with a relatively large attenuation $n = n' + in''$, where n' and n'' are the real and imaginary parts of the refractive index, $n'' \ll n'$. With account of the polarization term, the wave equation can be written out as

$$\left(\Delta_\perp + n^2(r)k^2 - \beta^2 + i\frac{\partial\beta}{\partial z}\right)\mathbf{E}$$

$$= in''\nabla_\perp\left\{\mathbf{E}\nabla_\perp\left(\frac{1}{n'}\right)\right\} + \nabla_\perp(\mathbf{E}\nabla_\perp \ln n'), \qquad (1)$$

where z is the longitudinal coordinate. In deriving Eq. (1), we allowed for $\nabla_\perp \ln n = \nabla_\perp \ln n' + in''\nabla_\perp\left(\frac{1}{n'}\right)$.

The last term on the right-hand side of Eq. (1) makes it possible to describe the Magnus optical effect in the wave approximation [2]. Therefore, we disregard this term. We seek a solution for the circularly polarized mode in the following form:

$$\mathbf{E}_{mN} = \frac{\mathbf{e}_1 + i\sigma\mathbf{e}_2}{\sqrt{2}}\Psi_{mN}e^{im\varphi + i\beta_{mN}^{(0)}z},$$
$$(\Delta_\perp + n^2k^2)\Psi_{mN} = (\beta_{mN}^{(0)})^2\Psi_{mN}. \qquad (2)$$

After simple transformations, we found from Eqs. (1) and (2)

$$\frac{\partial\beta_{mN}}{\partial z} = -n''\iint\Psi_{mN}(\mathbf{e}_\perp^*\nabla_\perp\Psi_{mN}^*)\left(\mathbf{e}_\perp\nabla_\perp\frac{1}{n'}\right)dS_\perp, \qquad (3)$$

where $\mathbf{e}_\perp = \frac{1}{\sqrt{2}}(\mathbf{e}_1 + i\sigma\mathbf{e}_2)$.

For an optical fiber with a parabolic profile of the refractive index

$$n^2 = n_{co}^2\left(1 - 2\Delta\left(\frac{r}{\rho_0}\right)^2\right) \qquad (4)$$

we obtain

$$\int\beta_{mN}dz = -n''\frac{\Delta}{\rho_0^2 n_{co}}\sigma m z^2. \qquad (5)$$

Russian Federal Nuclear Center, All-Russia Scientific Research Institute of Technical Physics, Snezhinsk, Chelyabinskaya oblast, 456070 Russia

1028-3358/03/4803-0105$24.00

Since an arbitrary input radiation can be represented in the form of a linear combination of directed circularly polarized modes, we obtain according to formula (5) that the speckle patterns for various σ will be T rotated with respect to each other by the angle

$$\Delta\varphi = |2\delta\varphi|, \quad \delta\varphi = \sigma n'' \frac{\Delta}{n_{co}\rho_0^2} z^2. \tag{6}$$

Indeed, for $z \neq 0$, it follows for an arbitrary mode that $\varphi \longrightarrow \varphi - \frac{\sigma n'' \Delta z^2}{\rho_0^2 n_{co}}$; i.e., the intensity distribution for various σ are similar but are shifted by the angle $\Delta\varphi$ [see (6)].

In the case of the optical Magnus effect for optical fiber (4), the T quantity $\delta\varphi$ is a linear function of σ:

$$\delta\varphi = \frac{\sigma\lambda\Delta}{2\pi n_{co}\rho_0^2 z}. \tag{7}$$

We now estimate the quantity n'' and the optical-fiber length z for which the effect under consideration can be observed experimentally. Let $\Delta = 0.01$, $n_{co} = 1.5$, $\rho = 5$ μm, $\lambda = 0.63$ μm, $z = 10$ cm, $\Delta\varphi = 0.2$ rad. According to (6), we obtain for such parameters $n'' = 3.75 \times 10^{-8}$, which corresponds at $\lambda = 0.63$ μm to the attenuation coefficient $\alpha = \frac{4\pi n''}{\lambda} \approx 7.5 \times 10^{-3}$ cm^{-1}. This can be attained when the optical fiber is exposed to gamma-ray radiation. In order to accomplish this, following [12], the optical fiber should be subjected to the exposure with a dose of ~250 Gy. In this case, in accordance with (7), the speckle patterns for various σ in the case of the optical Magnus effect are rotated by the angle $\Delta\varphi = |2\delta\varphi| \approx 0.53$ rad. This implies that the magnitude of the rotation angle for the speckle pattern for irradiated and nonirradiated optical fibers of equal lengths will differ by the angle determined by equality (6).

A similar effect can be considered for a particle with the spin of $\frac{1}{2}$ and nonzero mass, which moves in a weakly scattering medium. For a nonmeridional trajectory of the particle, the wave function in the paraxial approximation has the form

$$\Psi = \tilde{\Psi}\exp(-\beta''s + i\int\beta' dz),$$

where s is the natural parameter measured along the particle trajectory and z is the cylindrical coordinate. Correspondingly, we arrive at the following scalar wave equation, which includes spin–orbit interaction and is written in the cylindrical coordinate system:

$$i\frac{\partial\beta_2'}{\partial z}\tilde{\Psi} + \Delta_\perp\tilde{\Psi} + \left[\frac{2M}{h^2}(E - u(\rho) - i\frac{\beta''}{\beta_1'}\frac{h^2}{4M^2c^2}\frac{1}{\rho}\frac{du}{d\rho}\hat{\boldsymbol{\sigma}}\hat{\mathbf{l}}\right)\Big]\tilde{\Psi} = 0. \tag{8}$$

Here, $\beta' = \beta_1' + \beta_2'(z)$, $\beta_1' = \text{const}$, $\beta_1' \gg \beta_2'$. When deriving Eq. (8), we took into account the fact that, for $\Psi \sim \exp(-\beta''z)$, the quantity $\hat{\boldsymbol{\sigma}}\hat{\mathbf{l}}$ yields the following correction to the wave equation:

$$\delta\{(\hat{\boldsymbol{\sigma}}\hat{\mathbf{l}})\Psi\} = \left\{i\frac{\beta''}{\beta_1'}\hat{\boldsymbol{\sigma}}\hat{\mathbf{l}}\tilde{\Psi}\right\}\exp(-\beta''z). \tag{9}$$

Assuming $l \gg 1$, we obtain from Eq. (8) for a particle polarized along the *OZ* axis

$$\frac{\partial\beta_2'}{\partial z} = \frac{\sigma m}{2Mc^2}\frac{1}{\rho}\frac{du}{d\rho}\frac{\beta''}{\beta_1'},$$

where $\hat{\sigma}_z\Psi = \sigma\Psi$, $\hat{l}_z\Psi = m\Psi$, $\sigma = \pm 1$, and m is the projection of the orbital angular momentum.

As is seen from relationships (1) and (8), the quantity $\frac{2M}{h^2}(E-u)$ plays the same role that the quantity $n^2k^2 = \frac{\omega^2 n^2}{c^2}$ plays in optics. With allowance for this fact, Eq. (9) takes the form

$$\frac{\partial\beta_2'}{\partial z} = \frac{\sigma m}{M^2c^2}h^2\beta''\beta_1'\frac{\Delta}{\rho^2}, \tag{10}$$

where, in accordance with (4), we took into account the fact that

$$\frac{1}{\beta_1'}\frac{du}{d\rho} = -\frac{h^2}{M}\frac{d\beta_1}{d\rho}.$$

Thus, for a nonrelativistic particle, the effect is weaker by the value $\sim\frac{v^2}{c^2}$ than in the case of a photon. This is not L surprising as far as the spin–orbit interaction for a particle with a nonzero mass is an effect on the order of $\sim\frac{1}{c^2}$.

The phenomena considered above for the case of an optical fiber could be employed in measuring γ-radiation fields doses in the range 10^2–10^4 Gy.

REFERENCES

1. B. Ya. Zel'dovich and V. S. Liberman, Kvant. Élektron. (Moscow) **17**, 493 (1990).
2. A. V. Dooghin, B. Ya. Zel'dovich, N. D. Kundikova, and V. S. Liberman, Pis'ma Zh. Éksp. Teor. Fiz. **53**, 186 (1991) [JETP Lett. **53**, 197 (1991)].
3. A. V. Dooghin, B. Ya. Zel'dovich, N. D. Kundikova, and V. S. Liberman, Zh. Éksp. Teor. Fiz. **100**, 1474 (1991) [Sov. Phys. JETP **73**, 816 (1991)].
4. N. R. Sadykov, Kvant. Élektron. (Moscow) **20**, 1137 (1993).
5. M. V. Berry, Proc. R. Soc. London, Ser. A **392**, 45 (1984).
6. S. Pancharot, Proc. Indian Acad. Sci. **44**, 247 (1956).
7. S. M. Rytov, Dokl. Akad. Nauk SSSR **18** (4/5), 263 (1938).
8. V. V. Vladimirskiĭ, Dokl. Akad. Nauk SSSR **21** (3), 222 (1941).
9. I. V. Kataevskaya and N. D. Kundikova, Kvant. Élektron. (Moscow) **22**, 959 (1995).
10. N. R. Sadykov, Izv. Vyssh. Uchebn. Zaved., Fiz., No. 10, 58 (1999).
11. A. N. Gur'yanov, V. M. Kim, V. M. Mashinskiĭ, *et al.*, Tr. Inst. Obshch. Fiz. Akad. Nauk SSSR **23**, 94 (1990).
12. A. Snyder and J. Love, *Optical Waveguide Theory* (Chapman and Hall, London, 1983; Radio i Svyaz', Moscow, 1987).

Translated by T. Galkina

Doklady Physics, Vol. 48, No. 3, 2003, pp. 108–111. Translated from Doklady Akademii Nauk, Vol. 389, No. 1, 2003, pp. 41–44.

PHYSICS

On the Nature of Ball Lightning

V. P. Torchigin

Presented by Academician A.F. Andreev December 2, 2002

Received October 22, 2002

The hypothesis that ball lightening is not associated with electricity is substantiated. It is intense light from usual lightening that falls in a spherical air layer with increased pressure and circulates in this layer for a long time. Compressed air whose refractive index exceeds that of the environment presents an optical thin-film guide for circulating light and confines light propagating in it. Circulating intense light induces increased pressure in the air due to electrostriction. Thus, compressed air confines light, whereas light prevents the equalization of the pressure of compressed air. Figure 1 shows the variation in pressure and intensity along the section of such a self-restricting spherical layer (SRSL). The SRSL is a kind of the well-studied planar self-restricting layer, where the distribution of intensity along the section of the layer has the form $I = I_0\cosh^{-1}(\eta x)$ [1]. It is known that this layer is stable.

It is difficult to imagine that light can circulate in air for several seconds. Indeed, a 1-cm-thick air layer at normal atmospheric pressure scatters a 2.7×10^{-7} fraction of the white light passing through it [2]. Therefore, the intensity of light passing through a 100-km-thick air layer decreases by a factor of $e^{2.7} \simeq 15$. Light travels 100 km in 0.3 ms. This time interval is comparable to the lifetime of an SRSL and is shorter than the lifetime of ball lightening by at least four orders of magnitude. However, more careful analysis shows that the molecular scattering of light in real gases, and in particular, air, at extremely high pressures decreases sharply. The intensity I of scattered light for molecular scattering is determined by Einstein's formula [2]

$$I = I_0\frac{\pi V}{2\lambda^4 L^2}\left(\rho\frac{d\varepsilon_0\varepsilon}{d\rho}\right)_T^2\beta_T kT(1+\cos^2\Theta), \qquad (1)$$

where I_0 is the intensity of light falling on a gas volume V; λ is the light wavelength; L is the distance from the volume V to the point where the intensity of scattered light is measured; $\beta_T = -\frac{1}{V}\left(\frac{dV}{dp}\right)_T$ is the isothermal compressibility of the gas; ρ, p, T, and ε are the density, pressure, temperature, and dielectric constant of the gas, respectively; ε_0 is the permittivity of free space; k is Boltzmann's constant; and Θ is the scattering angle of light. According to this formula, the scattering of light in real gases described by the van der Waals equation tends to zero at extremely high pressures [3], because molecular scattering is proportional to gas compressibility, which tends to zero with increasing pressure for real gases. The molecular scattering of light at a pressure of 25 GPa is lower than that at normal atmospheric pressure by four orders of magnitude.

We now analyze the stability of the SRSL. The electrostriction pressure induced by light propagating in an optical medium is determined by the expression [2]

$$\Delta p = \rho\frac{d\varepsilon_0\varepsilon}{d\rho}\frac{E^2}{2}, \qquad (2)$$

where E is the amplitude of the electric field in the light wave. Since the energy density of light in air is determined as $w = \varepsilon_0\varepsilon\frac{E^2}{2}$, Eq. (2) can be represented as $\Delta p \simeq \Delta\varepsilon(p)w$, $\Delta\varepsilon(p) = \sigma(\varepsilon_n - 1)$, where $\varepsilon_n = 1.00055$ is the

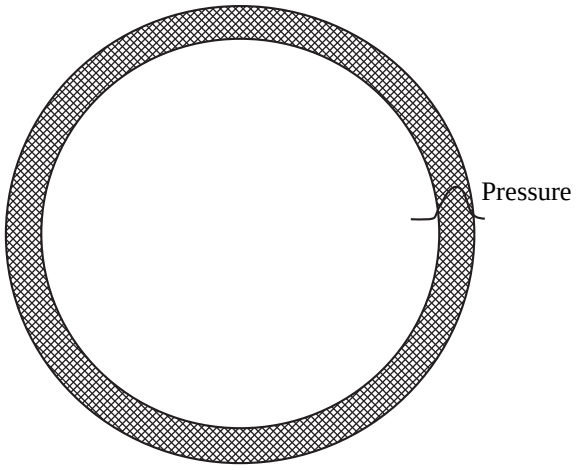

Fig. 1. Schematic representation of the SRSL.

Institute of Informatics, Russian Academy of Sciences, ul. Vavilova 30/6, Moscow, 117900 Russia
e-mail: v_torchigin@mail.ru

1028-3358/03/4803-0108$24.00

dielectric constant of air at normal pressure and σ determines the air compression degree.

The SRSL is in equilibrium when the total energy is minimal, i.e., when

$$\frac{dE_l}{dV} + \frac{dE_g}{dV} = 0, \quad (3)$$

where E_l and E_g are the energies of the light and gas, respectively. In this case, $\frac{dE_g}{dV} = p$ is the pressure of the compressed gas.

To determine the volume dependence of the energy of light, it is necessary to take into account that the energy density of light w increases with a decrease in the refractive index [4] and $E_l \sim n^{-1}$. The refractive index n depends on the air compression degree as $n = (1 + \Delta\varepsilon)^{1/2}$, $\Delta\varepsilon = \sigma(\varepsilon_n - 1)$. Therefore, the volume dependence of the energy of light is represented as

$$E_l = E_n\left(1 - 0.5(\varepsilon_n - 1)\frac{V_n}{V}\right),$$

where E_n and V_n are the energy of light and volume occupied by the compressed gas at normal pressure. In this case,

$$dE_l = 0.5E_n(\varepsilon_n - 1)\frac{V_n}{V}\frac{dV}{V}$$

$$= 0.5w_l(\varepsilon_n - 1)\frac{V_n}{V}dV = 0.5w_l\sigma(\varepsilon_n - 1)dV,$$

where $w_l = \frac{E_n}{V}$ is the energy density of light in compressed air. Equilibrium condition (3) can be represented in the form $p = 0.5\, w_l\sigma(\varepsilon_n - 1)$.

The table presents the energy density of air w_g for various pressures p and various energy densities of light w_l inducing this pressure. According to the table, the energy density of compressed air is much higher than the energy density of light. However, this difference decreases with an increase in light intensity. This means that the energy of the SRSL is predominantly the energy of compressed air. The energy density of light is equal to 405 kJ/cm^3 at an air pressure of 21.9 GPa. If the thickness of the SRSL is equal to $h = 1$ μm, a 20-cm-diameter SRSL has a volume of about 0.1 cm^3 and contains a light energy of 40.5 kJ and a compressed-air energy of 200 kJ. These estimates of the energy of the SRSL completely agree with the available estimates of 10^5–10^6 J for the energy of a 20-cm-diameter ball lightening. The energy density is rather large.

When radiation circulates inside the SRSL, the radiation momentum $P = \frac{E}{c}$, where E is the energy of light, varies. A fraction of electrostriction pressure is spent on

Table

p, atm	w_l, kJ/cm^3	w_g, kJ/cm^3
219	0.81	205
728	1.744	621
2190	4.46	1040
21900	40.9	1670
219000	405	2140

the generation of centripetal pressure $p_c = \frac{wh}{R_0}$, where h is the thickness of the SRSL, which ensures the circulation of P along a closed circular trajectory of radius R_0. The equilibrium condition for the spherical layer can be written in the form $\Delta p = p + \frac{p_c}{2\pi}$. For thin layers such that $\frac{h}{R_0} \ll \frac{1}{200}$, we have $p_c \ll p$.

In conclusion, let us show that all the mysterious and surprising features of the behavior of ball lightening are explained quite simply. We will take into account that each element of the surface of the SRSL in the inhomogeneous atmosphere is obviously subjected to an additional force proportional to the projection of the gradient of the refractive index on the outer normal to this surface. In particular, if the gradient is constant in the region where the SRSL is located, the SRSL moves along the gradient under the action of the resulting force. If air pressure is identical at all points of the atmospheric volume under consideration, the refractive index is inversely proportional to temperature, and the SRSL moves towards the temperature gradient.

When approaching a hole in a wall, where the temperature gradient is directed towards the motion of the SRSL (Fig. 2a), the following effect arises. Due to radiation, the SRSL heats the wall regions that hinder its penetration to the hole (H in Fig. 2). Walls heat air near them due to heat conductivity. As a result, the temperature gradient in these regions is directed to the walls, and the regions of the SRSL that are situated near the hole axis are subjected to forces repulsing these regions from the walls. On the other hand, the regions of the SRSL that are situated near the hole axis are subjected to forces that tend to draw these regions toward the hole. These opposite forces applied to different regions of the SRSL deform the SRSL, whose restoring forces are weak, and the SRSL takes the shape shown in Fig. 2b. As the SRSL penetrates the hole, the following feedback mechanism arises. The closer the SRSL to the walls of the hole, the more air in the region between the SRSL and the wall of the hole is heated, and the stronger the SRSL is repulsed from this region. As a result, the elongated deformed SRSL is situated equidistantly

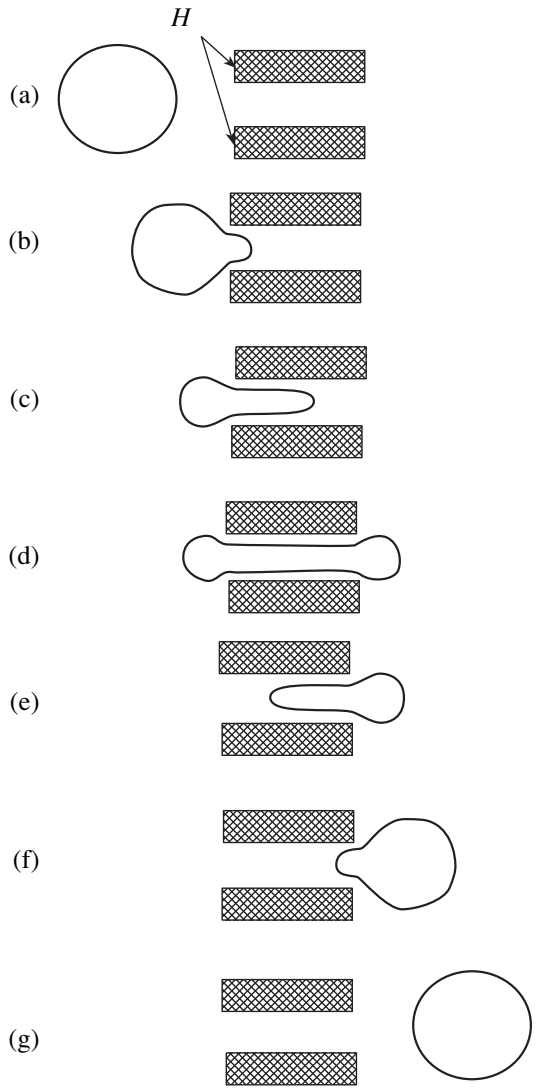

Fig. 2. Stages of the SRSL passing through a hole.

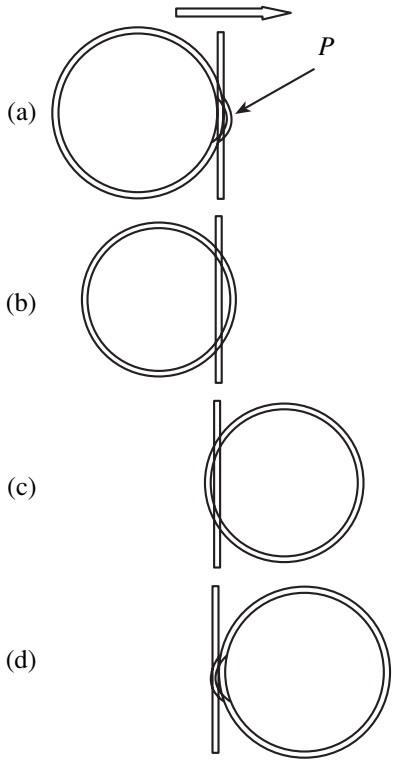

Fig. 3. Stages of the SRSL passing through window glass.

from the walls of the hole, whose cross section can have an arbitrary shape. Since the forces associated with the original gradient of air density along the hole axis continue to act, the SRSL continues to be drawn to the hole. Figures 2b–2f show the stages of the penetration of the SRSL through the hole in the wall.

Ball lightening can penetrate through window glass, sometimes destroying them. In this case, the destruction is located at the place where the ball lightening penetrates. As is known, a plasma cannot penetrate through glass, whereas light passes through glass. The penetration of the SRSL through a plane glass plate can be represented as follows. When light touches the plate, light penetrates into glass and undergoes total internal reflection from the opposite side of the plate, because the refractive index of air inside the SRSL is higher than that on the other side of the plate. In the range of the total internal reflection at the interface between air and opposite side of the plate, an intense light field arises and induces increased air pressure, which leads to an increase in air density. This region is indicated by the arrow with letter *P* in Fig. 3a. As a result, portions of light radiation penetrate into this region of increased pressure and form an SRSL on the other side of the plate, as is shown in Fig. 3b. If the densities of atmospheric air are somewhat different on the different sides of the plate, the SRSL moves towards the side where the density is higher according to the effect described above. As is seen, the SRSL easily passes through glass, as is shown in Figs. 3c and 3d. In fact, only the light easily passes and forms a compressed-air layer on the other side. The compressed air located in the SRSL does not pass through glass.

The above-mentioned weakness of the forces restoring the spherical shape of the SRSL is manifested not only when traversing holes. For sufficiently large sphere radii *R*, there is nonuniformity of air density along the height of the SRSL. Indeed, if the SRSL is located at constant height, its equator is in the air layer with the maximum density. In this case, the gradient of air density above and below the SRSL is directed towards its center and leads to the deformation of the SRSL, which takes the shape of a spheroid oblate in the vertical direction or of a flying plate.

It is known that the color of ball lightening can vary from white and yellow to green. The variation in the color of the SRSL is explained as follows. In an SRSL,

which is an equilibrium system of intense radiation and air compressed by this radiation, the energies of radiation and compressed gas are balanced. This balance can be violated when forming the SRSL. When approaching the steady state and restoring balance, gas and radiation exchange energy. If air (radiation) returns a fraction of its energy to radiation (air), the average frequency of radiation increases (decreases), and the radiation spectrum is shifted towards short (long) wavelengths. Thus, the color of the SRSL indicates the conditions of its origin. We note that the SRSL is a peculiar transformer of the energy of light to the energy of a gas and vice versa.

REFERENCES

1. H. Haus, *Waves and Fields in Optoelectronics* (Prentice-Hall, Englewood Cliffs, 1984; Mir, Moscow, 1988).
2. G. S. Landsberg, *Optics* (Nauka, Moscow, 1976).
3. *Handbook of Physical Quantities*, Ed. by I. S. Grigoriev and E. Z. Melikhov (Énergoatomizdat, Moscow, 1991; CRC Press, Boca Raton, 1997).
4. V. P. Torchigin, Zh. Tekh. Fiz. **66** (4), 128 (1996) [Tech. Phys. **41**, 365 (1996)].

Translated by R. Tyapaev

Doklady Physics, Vol. 48, No. 3, 2003, pp. 112–115. Translated from Doklady Akademii Nauk, Vol. 389, No. 1, 2003, pp. 45–48.

PHYSICS

Determination of the EAS Cascade-Curve Shape by the Radio Method

V. A. Tsarev and V. A. Chechin

Presented by Academician E. L. Feĭnberg July 18, 2002

Received July 19, 2002

In this paper, the possibility of determining the shape of the cascade curve of extensive air showers (EAS) by the radio method is shown. This is essential for increasing the reliability of the detection of ultrahigh-energy cosmic-ray particles in order to obtain information on their nature.

The problem of ultrahigh-energy cosmic rays (UHECR) is one of the challenges to modern high-energy astrophysics [1–4]. As a consequence of the Greisen–Zatsepin–Kuzmin effect [1, 2], cosmic rays with energies $E \geq 5 \times 10^{19}$ eV could not be observed in the vicinity of the Earth. Nevertheless, they are observed. Their flux is extremely low ($\sim 10^{-2}$ year^{-1} km^{-2} sr^{-1} for $E \geq 10^{20}$ eV). Detectors dedicated to experimental studies of these particles are currently under construction. In this case, the area being scanned ranges from 6000 km^2 (for the ground-based Auger observatory [5]) to $\sim 10^5$ km^2 (for satellite-borne detection of fluorescent light in the framework of the OWL and EUSO projects [6]).

In [7–12], it was proposed to detect the UHECR from satellites and balloons using radio emission generated in the Earth's atmosphere by horizontal T EAS initiated by such particles. This provides a means for scanning over a very large area, up to $(1.5–2) \times 10^7$ km^2, and makes possible a high UHECR detection rate with a reasonable accuracy of the determination of their energy E_0 and arrival angles (θ, φ). Preliminary estimates show that the realization of the radio method using satellites would be by one or two orders of magnitude less expensive than the construction and operation of the detectors discussed in [5, 6]. At the same time, it is commonly supposed that the radio method has certain limitations compared to traditional methods.

First, when using a radio receiver without coincidence with other EAS detectors, the identification of a detected signal with a radio pulse from an EAS is usually based on two things. These are the expected signal-to-background ratio $\left(\frac{S}{B} > 1\right)$ and the typical short duration of an EAS-initiated pulse ($\tau \approx 10^{-7}$–10^{-6} s [10]), which differs from the much longer typical duration of natural and artificial radio-noise pulses. Although this situation resembles that for the EAS detection (only) by Cherenkov T flares (this method is widely used in modern experimental practice), the mentioned signature for the EAS radio-pulse separation casts some doubts in the context of the variable character of the time dependence of man-made noise.

Second, the EAS detection by ground-based shower arrays (when they allow detection of different EAS components, e.g., electron–photon and muon components) or by fluorescent-light detectors (when the shape of the EAS cascade curve can be determined) provides information for separating EAS initiated by protons and nuclei.

When detecting EAS by the radio method from satellites or balloons, it is not feasible to simultaneously detect various shower components. In this case, only the integral value of a radio signal is detected (during the time of the total pulse duration), and information on the shower development is absent. At first glance, these limitations seem to be inevitable, but this is not true. Below, it is shown that a radio pulse contains information that allows researchers to determine the cascade-curve shape and, consequently, distinguish between proton-initiated and nucleus-initiated showers, as well as obtain a clear signature for selecting an EAS signal against the noise background.

We assume that the distance R between a radio receiver and an EAS is known. (R can be determined from the height H of the receiver position above the Earth's surface and the opening angle $\Delta\theta$ of the antenna's directivity diagram [11].) In any case, this distance is much larger than the EAS development length L. In addition, we assume that all shower particles move in parallel to the EAS axis and ignore for a moment the shower disk size. Then, the EAS development can be considered as a motion with a velocity v close to the velocity of light c of a compact shower body with a variable particle number $N_{\text{tot}}(t)$. We now suppose that a point A corresponds to the shower origin.

Lebedev Physical Institute, Russian Academy of Sciences, Leninskiĭ pr. 53, Moscow, 117924 Russia

1028-3358/03/4803-0112$24.00

In this case, t is the time elapsed between the moments of the signal arrival at the receiver (located at a point Q) from the point A and a certain point B of the shower. This time is related to the time t' required for the shower disk to travel a path between these points by the following relation:

$$t = \frac{r_{AB}}{v} + (r_{BQ} - r_{AQ})\frac{\mu}{c} \approx t'G,$$
$$G = 1 - \beta\mu\cos\alpha \approx \frac{\alpha^2}{2} - \delta. \quad (1)$$

Here, $\beta = \frac{v}{c}$, $\mu = 1 + \delta$ is the atmospheric refractive index for radio waves ($\delta \approx 3 \times 10^{-4}$ for the normal atmosphere), and α is the radiation observation angle with respect to the shower axis. If $\alpha_C = \arccos\frac{1}{\beta\mu}$ is the Cherenkov radiation angle, then $t = 0$ for $\alpha = \alpha_C$, i.e., the signals from different points of the shower arrive at the receiver simultaneously. This corresponds to the condition of Cherenkov radiation. For $\alpha < \alpha_C$, the signals arrive at an observer in antichronological order; i.e., they come earlier from later stages of the EAS development. For larger values of the observation angle, the signals from various parts of the shower come to the receiver in the proper order. (The form of the dependence $t(\alpha)$ weakly changes with energy, since the cascade length depends upon the EAS energy logarithmically.) Using this dependence, we can find the EAS energy E_0 by simultaneous measurements of both radio-signal magnitude and duration [7–12].

We now suppose that the time variation of a radio pulse (which depends on $N_{tot}(t)$) is also measured. Then, as is seen from Eq. (1) for $\alpha > \alpha_C$, a possibility arises to scan the shower development, i.e., to obtain an information on the temporal development of the shower and, consequently, on the cascade-curve shape $N_{tot}(t) = N_{tot}\left(\frac{x}{c}\right)$. As already was noted, the cascade-curve shape carries important information on the nature of the primary particle that initiated the shower. Hence, the knowledge of the cascade-curve shape allows discrimination between primary protons and nuclei. Furthermore, the EAS-produced signals can be separated from background ones by comparison of the measured dependence $N_{tot}(t)$ with the typical shape of the EAS cascade curve (which is reasonably well known from both numerous experiments and results of mathematical modeling). As is evident from Eq. (1), the t dependence of the radio-signal amplitude is conveniently measured for the largest possible values of the angle α when the observed signal duration is sufficiently long.

Finite longitudinal and transverse dimensions of the shower disk result in an additional difference in the signal arrival time τ_1, which is on the order of 2×10^{-8} s for high-energy EAS. This value should be compared with a typical observed radio pulse duration

$$\tau_{EAS} \approx \frac{L}{c}(1 - \beta\mu\cos\alpha)$$

related to the EAS development. For $\alpha \geq 0.05$, we have $\tau_{EAS} \geq 2 \times 10^{-7}$ s [10]; i.e., the time interval in which the t dependence of radio pulses can be measured exceeds the spreading due to finite disk dimensions by about a factor of 10. It was shown in [7–12] that, in the case when a system of two (or more) receivers is used, the delay-time measurements make it possible to determine the azimuth angle of the signal arrival with high accuracy. A similar system is also convenient for the measurements under consideration of the EAS cascade-curve shape. Properly choosing the distance between the receivers, we can provide conditions when at least one of two receivers is oriented at an angle α, which lies in an interval favorable for the measurements of the angle $\alpha_C < \alpha < \alpha_{max}$. Here, α_{max} is determined by registration conditions (background, ionosphere transparency).

We now obtain relations between the desired dependence $N_{tot}(t)$ and the measured field $H(t) = E(t)$. To do this, we use the results of the EAS radio-pulse calculations, which were obtained in [7–12]. First, we consider only the contribution of the EAS electron excess [13]. We choose the origin at a point O in the shower axis. Let $\mathbf{R}_0$ be the radius vector of the observation point, $\mathbf{n} = \frac{\mathbf{R}_0}{|\mathbf{R}_0|}$, $\mathbf{r}_0(t')$ is the radius vector of the shower-disk center, and $\mathbf{r}' = \mathbf{r} - \mathbf{r}_0(t')$. The shower development time t' is related to the observed time t of the signal arrival at the point Q by the following relation (we assume $\mu = 1$, $v \approx \text{const} \approx c$):

$$t'\left(1 - \frac{\mathbf{vn}}{c}\right) = \tau + \frac{\mathbf{r}'\mathbf{n}}{c}, \quad \tau = t - \frac{R_0}{c}. \quad (2)$$

The electric current corresponding to the motion of electron-excess particles can be represented in the form

$$\mathbf{j}(\mathbf{r}, t') = eN(t')\mathbf{v}f(\mathbf{r}'). \quad (3)$$

Here, $N(t') = \eta N_{tot}(t')$ is the number of the EAS excess electrons, $N_{tot}(t')$ is the total number of shower particles as a function of the EAS development time (EAS longitudinal profile), and the coefficient $\eta \approx 0.2$ is approximately t'-independent. The function $f(\mathbf{r}')$ describes the particle distribution in the shower disk, and it is normalized to unity:

$$\int f(\mathbf{r} - \mathbf{r}_0(t'))d\mathbf{r} = 1$$

for an arbitrary t'. Taking into account relationships (2) and (3), we can express the vector potential and radia-

tion fields produced by the current (3) at the observation point in the following form:

$$\mathbf{A}(R_0, t) \approx (cR_0)^{-1}\int \mathbf{j}(\mathbf{r}, t')d\mathbf{r}$$

$$= \frac{e\mathbf{v}}{cR_0}\int N(t')\left(1-\frac{\mathbf{vn}}{c}\right)^{-1} f(\mathbf{r}')d\mathbf{r}', \quad (4)$$

$$\mathbf{H}\left(\tau+\frac{R_0}{c}\right) = c^{-1}\left[\left(\frac{\partial \mathbf{A}}{\partial \tau}\right)\times \mathbf{n}\right]$$

$$= e[\mathbf{v}\times\mathbf{n}]\left\{c^2R_0\left(1-\frac{\mathbf{nv}}{c}\right)^2\right\}^{-1} I\left(\tau, \frac{\mathbf{nv}}{c}\right), \quad (5)$$

$$I\left(\tau, \frac{\mathbf{nv}}{c}\right) = \int N'(t')f(\mathbf{r}')d\mathbf{r}';\ \ N'(x) \equiv \frac{dN(x)}{dx}. \quad (6)$$

We introduce the cylindrical coordinate system $\mathbf{r}'$ with the z axis directed along the vector $\mathbf{n}$: $\mathbf{r}' = (z; \boldsymbol{\rho})$. Then the argument of N' depends only on the single spatial variable z, and

$$I(\tau) = \int N'(t')S(z)dz,$$
$$S(z) = \int f(z, \boldsymbol{\rho}')d\boldsymbol{\rho}' = \int f(\mathbf{r}')\delta(z-\mathbf{r}'\mathbf{n})d\mathbf{r}'. \quad (7)$$

The relation for $S(z)$ has a simple physical sense and determines the area of the shower-disk cross section by a plane perpendicular to the unit vector $\mathbf{n}$. The waves produced by the charges residing at this cross section arrive at the observation point in the same phase. Relations (5)–(7) establish a link between the observed t dependence of the radiation field and the desired dependence $N(t)$, which we are interested in. Evidently, in the general case, an unambiguous reconstruction of the EAS space–time structure from only the function $\mathbf{H}(\tau)$ is impossible. However, in the actual situation, the function $f(\mathbf{r}')$, which describes the shower-disk spatial structure, is reasonably well known from experiments and modeling of the EAS development. Moreover, as is seen below, for $\alpha \gg \alpha_C$, the t dependence for the pulse is predominantly determined by the EAS longitudinal development, and the particle-distribution shape within the shower disk turns outs to be of little significance for finding the cascade curve. Thus, relations (5)–(7) allow us to find the function $N(t')$ from the measured dependence $H(t)$. In particular, in the point-charge approximation, we arrive at

$$\mathbf{H}\left(\tau+\frac{R_0}{c}\right) = e[\mathbf{v}\times\mathbf{n}]$$

$$\times\left\{c^2R_0\left(1-\frac{\mathbf{nv}}{c}\right)^2\right\}^{-1} N'\left[\frac{\tau}{1-\mathbf{nv}/c}\right]. \quad (5a)$$

The simplest method for finding cascade-curve parameters consists in using in expression (7) an explicit parameterization for $N(t)$ and $f(\mathbf{r}')$ and determining unknown parameters of the model. We suppose that the charge distribution in the disk is of the form

$$f(\mathbf{r}') = \{\pi^{3/2}\sigma_1\sigma_2^{1/2}\}^{-1}\exp\left(-\frac{\rho'^2}{\sigma_1}-\frac{z'^2}{\sigma_2}\right). \quad (8)$$

Then, the integral entering into relationship (7) can be calculated explicitly:

$$S(z) = (\pi\sigma)^{-1/2}\exp\left(-\frac{z^2}{\sigma}\right),$$
$$\sigma = \sigma_1\cos^2\alpha + \sigma_2\sin^2\alpha. \quad (9)$$

We now take into account a separation of positively and negatively charged particles by geomagnetic field at a certain distance $\pm\frac{d}{2}$ from the EAS axis. For definiteness, we assume that this separation takes place in a plane passing through $\mathbf{n}$ and $\mathbf{v}$. Then,

$$f_d(r') = 2^{-1}\left(1+\frac{1}{\eta}\right)f\left(x'+\frac{d}{2}, y', z'\right)$$
$$+ 2^{-1}\left(1-\frac{1}{\eta}\right)f\left(x'-\frac{d}{2}, y', z'\right), \quad (10)$$

$$S_d(z) = 2^{-1}\left(1+\frac{1}{\eta}\right)S\left[z+\frac{d}{2}\sin\alpha\right]$$
$$+ 2^{-1}\left(1-\frac{1}{\eta}\right)S\left[z-\frac{d}{2}\sin\alpha\right]. \quad (11)$$

We also use the Gaussian form for the cascade curve $N(t')$:

$$N(t') = N_{\max}\eta\exp\left(-\frac{t'}{T^2}\right). \quad (12)$$

Here, t' is measured from the moment when the cascade reaches its maximum. Then,

$$I(\tau) = N_{\max}\eta\left(1-\frac{\mathbf{nv}}{c}\right)^2 T(\sigma+\sigma_T)^{-3/2}$$
$$\times(-2\tau)\exp\left[-\frac{\tau^2}{\sigma+\sigma_T}\right]. \quad (13)$$

In (13), $\frac{\sigma_T}{c^2} = T^2\left(1-\frac{\mathbf{nv}}{c}\right)^2$ corresponds to the pulse duration squared that is related to the EAS longitudinal development time T, while $\frac{\sigma}{c^2}$ is the duration squared that is related to the finite dimensions of the shower disk. To take into account the charge separation by virtue of geomagnetic effects, the replacement $z \longrightarrow z \pm \frac{d}{2}\sin\alpha$ should be made in (13). This corresponds to

the substitution $\tau \longrightarrow \tau - \left(\pm\frac{d}{2c}\right)\sin\alpha$ in the expression for $I(\tau)$:

$$I_d(\tau) = 2^{-1}\left(1+\frac{1}{\eta}\right)I\left[\tau - \frac{d}{2c}\sin\alpha\right] + 2^{-1}\left(1-\frac{1}{\eta}\right)I\left[\tau + \frac{d}{2c}\sin\alpha\right]. \quad (14)$$

Since $\eta < 1$, I_d is the difference of two bipolar pulses, which are identical in their shape but differ in the amplitudes $\left(\text{factors } 1 \pm \frac{1}{\eta}\right)$ and are shifted in time by $\left(\frac{d}{c}\right)\sin\alpha$ with respect to each other. For radiation angles $\alpha \approx \alpha_C \approx (2\delta)^{1/2}$, $\sigma_T \approx 0$, and the t' dependence in (14) is entirely determined by the shower-disk parameters. For $\alpha \gg \alpha_C$, the value σ_T prevails, and the t dependence is determined by the EAS longitudinal development. In this case, the cascade-curve shape can be found without detailed knowledge of the form of the function $f(\mathbf{r}')$, just as is done in the point-charge approximation [see formula (5a)].

The foregoing relations were obtained in the t representation. Similar formulas can also be derived for Fourier components. In a number of cases, this may be useful in some instances (e.g., for taking into account a signal distortion during its propagation in a medium).

Thus, the relations obtained allow reconstruction of the EAS profile function from the measured time dependence or frequency dependence of the radiation field or of the emission intensity. This information can be used for both more reliable picking out of a desired signal from the background noise and finding the nature of the primary particle that initiated the EAS.

ACKNOWLEDGMENTS

The authors are grateful to Academician E. L. Feĭnberg for critical comments and interest in this work.

REFERENCES

1. G. T. Zatsepin and V. A. Kuz'min, Pis'ma Zh. Éksp. Teor. Fiz. **4**, 114 (1966) [JETP Lett. **4**, 78 (1966)].
2. K. Greisen, Phys. Lett. **16**, 748 (1966).
3. A. V. Olinto, Phys. Rep. **333**, 329 (2000).
4. X. Bertou, M. Baratov, and A. Letessier-Selvon, Int. J. Mod. Phys. A **15**, 2182 (2000).
5. J. W. Cronin, Rev. Mod. Phys. **71**, 165 (1999).
6. L. Scarsi and O. Catalano, in *Proceedings of the XXVII ICRC, 2001*, Vol. 2HE, p. 839.
7. K. M. Pichkhadze, V. G. Sysoev, V. A. Tsarev, and V. A. Chechin, Kratkie Soobshch. Fiz., No. 12, 9 (2000).
8. V. A. Tsarev and V. A. Chechin, Kratkie Soobshch. Fiz., No. 4, 42 (2001).
9. V. A. Chechin, N. G. Polukhina, and V. A. Tsarev, in *Proceedings of the XI Lomonosov Conference on Elementary Particles, Moscow, 2001*.
10. V. A. Tsarev and V. A. Chechin, Dokl. Akad. Nauk **383** (4), 486 (2002) [Dokl. Phys. **47**, 275 (2002)].
11. V. A. Tsarev, Kratkie Soobshch. Fiz., No. 11, 26 (2001).
12. V. A. Chechin, E. L. Feinberg, K. A. Kotelnikov, *et al.*, in *Proceedings of the V International Conference on Particle and Fundamental Physics in Space (Space Part), La Biodola, Isola d'Elba, 2002* (in press).
13. G. A. Askar'yan, Zh. Éksp. Teor. Fiz. **41**, 616 (1961) [Sov. Phys. JETP **14**, 441 (1962)]; **48**, 988 (1965) [Sov. Phys. JETP **21**, 658 (1965)].

Translated by V. Tsarev

Doklady Physics, Vol. 48, No. 3, 2003, pp. 116–118. Translated from Doklady Akademii Nauk, Vol. 389, No. 2, 2003, pp. 177–179.

PHYSICS

Interface Between Direct and Reverse Flows Inside a High-Frequency Inductive Discharge

A. V. Gerasimov* and A. P. Kirpichnikov

Presented by Academician V.E. Alemasov September 25, 2002

Received October 11, 2002

Analysis of the energy-balance equation in a high-frequency inductive discharge (HFID) indicates that the three velocity components of a plasma-generating gas are equal to zero at least at one point in the axis of any HFID and that axial temperature is maximal at this point [1].

However, it is possible to show that this physical phenomenon is only a particular case of a more general law inherent in the HFID as a whole.

Indeed, the total energy-balance equation (nonsimplified for the central part of the plasmoid) for the high-frequency inductive plasma evidently has the form

$$\frac{1}{r}\frac{\partial}{\partial r}\left(\lambda r\frac{\partial T}{\partial r}\right) + \frac{\partial}{\partial z}\left(\lambda\frac{\partial T}{\partial z}\right) + \sigma E_\varphi^2 = Q_R(r, z) + \rho c_p\left(v_r\frac{\partial T}{\partial r} + v_z\frac{\partial T}{\partial z}\right), \quad (1)$$

where T is the temperature; λ is the heat-conductivity coefficient; ρ is the density; c_p is the specific heat capacity; Q_R is the radiation energy density; v_r and v_z are the radial and longitudinal components of the velocity field in the discharge, respectively; E_φ is the electric-field intensity in the discharge; and σ is the conductivity in the discharge.

According to Eq. (1), the longitudinal velocity $v_z(r, z)$ in the discharge is described by the formula

$$v_z(r, z) = \frac{\frac{1}{r}\frac{\partial}{\partial r}\left(\lambda\frac{\partial T}{\partial r}\right) + \frac{\partial}{\partial z}\left(\lambda\frac{\partial T}{\partial z}\right) + \sigma E_\varphi^2 - Q_R(r, z) - \rho c_p v_r\frac{\partial T}{\partial r}}{\rho c_p\frac{\partial T}{\partial z}}. \quad (2)$$

Let us consider a family of coaxial cylindrical surfaces whose axes coincide with the HFID axis and that fill the entire inner volume of the plasmoid. Each surface corresponds to a certain radial coordinate r. Since this coordinate is continuous, the number of these surfaces is infinite. The surfaces corresponding to $r = 0$ and $r = R$ (R is the radius of a tube bounding the discharge) coincide with the plasmoid axis and with the wall of the discharge chamber, respectively.

Next, on each of these ancillary cylindrical surfaces, we consider a circle that corresponds to the maximum temperature on this surface (this is always possible, because the heat source, the plasmoid, has a finite length). Due to the continuity of this family of surfaces, these circles in turn form a certain cylindrically symmetric surface of revolution whose axis coincides with the plasmoid axis. This surface can be described by the equation:

$$\left.\frac{\partial T}{\partial z}\right|_{\Omega_0} = 0.$$

Further, following the method proposed in [1], we consider a locus Ω_0 satisfying the condition $\left.\frac{\partial T}{\partial z}\right|_{\Omega_0} = 0$; i.e., the surface Ω_0 inside the HFID is such that temperature at its points is maximal for each fixed r.

At all points of this surface, the denominator in Eq. (2) is equal to zero. Therefore, the numerator of this expression is also equal to zero, because the velocity v_z as a continuous physical quantity must be limited. Applying the l'Hópital's rule to Eq. (1), we find

Kazan State Technological University,
ul. Karla Marksa 68, Kazan, 420012 Tatarstan, Russia
** e-mail: gerasimov@kstu.ru*

1028-3358/03/4803-0116$24.00 © 2003 MAIK "Nauka/Interperiodica"

$$v_z\big|_{\Omega_0} = \frac{\frac{1}{r}\frac{\partial}{\partial z}\left[\frac{\partial}{\partial r}\left(\lambda r\frac{\partial T}{\partial r}\right)\right] + \frac{\partial^2\lambda}{\partial z^2}\frac{\partial T}{\partial z} + 2\frac{\partial\lambda}{\partial z}\frac{\partial^2 T}{\partial z^2} + \lambda\frac{\partial^3 T}{\partial z^3} + \frac{\partial}{\partial z}\left[\sigma E_\varphi^2 - Q_R(r,z) - \rho c_p v_r\frac{\partial T}{\partial r}\right]}{\frac{\partial}{\partial z}(\rho c_p)\frac{\partial T}{\partial z} + \rho c_p\frac{\partial^2 T}{\partial z^2}} = \left.\frac{\lambda\frac{\partial^3 T}{\partial z^3}}{\rho c_p\frac{\partial^2 T}{\partial z^2}}\right|_{\Omega_0}, \quad (3)$$

because, at $T(r, z) = T(\Omega_0)$,

$$\left.\frac{\partial\lambda(T)}{\partial z}\right|_{\Omega_0} = \left.\frac{\partial\lambda T}{\partial T}\frac{\partial T}{\partial z}\right|_{\Omega_0} = 0,$$

$$\left.\frac{\partial\rho(T)}{\partial z}\right|_{\Omega_0} = \left.\frac{\partial\rho(T)}{\partial T}\frac{\partial T}{\partial z}\right|_{\Omega_0} = 0,$$

$$\left.\frac{\partial c_p(T)}{\partial z}\right|_{\Omega_0} = \left.\frac{\partial c_p(T)}{\partial T}\frac{\partial T}{\partial z}\right|_{\Omega_0} = 0,$$

and both expressions in square brackets in the numerator of Eq. (3) have the form

$$R_1 = \frac{\partial}{\partial r}\left(\lambda r\frac{\partial T}{\partial r}\right),$$
$$R_2 = \sigma E_\varphi^2 - Q_R(r,z) - \rho c_p v_r\frac{\partial T}{\partial r} \quad (4)$$

and depend only on temperature and its radial rather than axial derivatives. Therefore, at $T = T(\Omega_0)$, we have

$$\left.\frac{\partial R_1}{\partial z}\right|_{\Omega_0} = \left.\frac{\partial R_2}{\partial z}\right|_{\Omega_0} = 0.$$

In Eq. (3), $\left.\frac{\partial^2 T}{\partial z^2}\right|_{\Omega_0} \neq 0$, and consequently $v_z(\Omega_0)$ is a finite quantity.

In view of Eqs. (4), Eq. (2) can be rewritten in the form

$$v_z(r,z) = \frac{\frac{R_1}{r} + \frac{\partial\lambda}{\partial z}\frac{\partial T}{\partial z} + \lambda\frac{\partial^2 T}{\partial z^2} + R_2}{\rho c_p\frac{\partial T}{\partial z}}$$
$$= \frac{\frac{R_1}{r} + \frac{\partial\lambda}{\partial T}\left(\frac{\partial T}{\partial z}\right)^2 + \lambda\frac{\partial^2 T}{\partial z^2} + R_2}{\rho c_p\frac{\partial T}{\partial z}}. \quad (5)$$

At all points of the surface Ω_0, the denominator of this expression is equal to zero and changes its sign when passing the surface Ω_0, because

$$\frac{\partial T}{\partial z} > 0 \quad \text{at} \quad z < z(\Omega_0),$$

$$\frac{\partial T}{\partial z} < 0 \quad \text{at} \quad z > z(\Omega_0).$$

It is evident that the numerator of this expression must obviously be equal to zero at these points, because v_z is a continuous quantity and is finite at points of this surface, in view of Eq. (3). In this case, however, all the terms in the numerator do not change their signs when passing the surface Ω_0 (R_1 and R_2), because they depend only on temperature and its radial (rather than axial) derivatives. The term $\lambda\frac{\partial^2 T}{\partial z^2}$ is negative to both the right and the left of this surface, whereas the sign of the term $\frac{\partial\lambda}{\partial T}\left(\frac{\partial T}{\partial z}\right)^2$ is determined by the sign of the derivative $\frac{\partial\lambda}{\partial T}$, which is negative in the temperature range under investigation [2, 3].

As is seen, none of the terms in the numerator of Eq. (5) for $v_z(r, z)$ changes its sign when passing the surface Ω_0. Since all the terms of the numerator are continuous and smooth, it retains its sign in the neighborhood of this surface; i.e., it tends to zero both on the right and on the left sides of the surface Ω_0 with the same sign. In turn, this means that the longitudinal velocity of the plasma-generating gas changes its sign at all points of the surface Ω_0, i.e., is equal to zero at points on this surface:

$$v_z(r,z)\big|_{\Omega_0} = 0. \quad (6)$$

Expression (6) physically means that the surface Ω_0 separates opposite flows of the plasma-generating gas.

In this case, according to Eq. (3),

$$\left.\frac{\partial^3 T}{\partial z^3}\right|_{\Omega_0} = 0$$

at the points of the surface Ω_0. Therefore, in the first approximation, temperature T as a function of z near the surface Ω_0 behaves as an even-power function in z:

$$T(r,z) \approx T(\Omega_0) + az^2 + bz^4,$$

where a and b are certain functions on r.

Thus, the main result obtained in this study can be formulated as follows. Inside the plasmoid of a HFID under atmospheric pressure, the regions of direct and inverse flow are separated by a certain surface (in view

of the cylindrical symmetry of the problem, it is a surface of revolution and is generally not a plane). This surface is a locus of those points at which temperature in the discharge is maximal.

As is seen, the effect of the fixed point in the high-frequency discharge, which was established in [1], is only a particular case of the more general physical phenomenon. This is a surface whose axis has zero velocity and that separates the direct and reverse flows in the discharge chamber of a high-frequency plasmatron.

This result is evidently attributed to the fact that heat that is mainly released in the discharge region, where the temperature is maximal, is removed by convective thermal flows to the end parts of the plasmoid.

This effect must probably be inherent in a wider class of objects having an inner heat source limited along the longitudinal coordinate.

REFERENCES

1. A. V. Gerasimov and A. P. Kirpichnikov, Teplofiz. Vys. Temp. **37** (3), 504 (1999).
2. A. S. Predvoditelev *et al.*, *Thermodynamic Functions of Air for Temperatures from 1000 to 12000 K and for Pressures from 0.001 to 1000 atm.* (Izd. Akad. Nauk SSSR, Moscow, 1960).
3. *Atlas of Gasodynamic Functions for High Velocities and High Temperatures of Air Flow*, Ed. by A. S. Predvoditelev (Gosénergoizdat, Moscow–Leningrad, 1961).

Translated by Yu. Vishnyakov

Doklady Physics, Vol. 48, No. 3, 2003, pp. 119–122. Translated from Doklady Akademii Nauk, Vol. 389, No. 3, 2003, pp. 324–327.

PHYSICS

Stimulation of the Partial Oxidation of Methane in a Microwave Discharge

Academician V. D. Rusanov, A. I. Babaritskiĭ, E. N. Gerasimov, M. A. Deminskiĭ, S. A. Demkin, V. K. Zhivotov, A. S. Moskovskiĭ, B. V. Potapkin, R. V. Smirnov, and M. I. Strelkova

Received November 1, 2002

The partial oxidation of methane by atmospheric oxygen,

$$2CH_4 + O_2 + 3.76N_2 = 2CO + 4H_2 + 3.76N_2 \qquad (1)$$

is a promising method of producing hydrogen or syngas for the needs of energy, chemical technology, transport, etc. Fundamental interest is focused on the kinetic features of the process, which requires the initiation of combustion and catalytic promotion by some methods. Below, we will analyze process (1) in a microwave discharge. Methods of stimulating the conversion of hydrocarbons that are based on the catalytic effect of a plasma including a microwave-discharge plasma were reported in [1–5, 8].

Since the content of methane in the original reagents of reaction (1) is equal to about 30% and lies beyond the limits of the ignition of the methane–air mixture (5–15% under normal conditions), reaction (1) requires the additional stimulation of methane combustion either by increasing the temperature of reagents or by some kind of initiation. A microwave discharge in use acts on the system in both these directions. First, it efficiently introduces additional thermal energy even to strongly heated reagents due to the high temperature of the plasma. Second, the plasma produces active particles promoting the oxidation of methane in chain reactions and initiates combustion.

The partial oxidation of methane (1) was studied experimentally in two types of microwave discharge: a pulsed periodic regime (streamer pseudocorona discharge [1–5, 8] with a wavelength of 3 cm, pulse power up to 300 kW, average power up to 300 W, a pulse duration of 1 μs, and a repetition frequency of 1 kHz) and a continuous regime (coaxial torch discharge with a frequency of 2.45 GHz and power in the range 1–5 kW). Original reagents could be heated up to 500–900°C and were supplied to a discharge chamber combined with the methane combustion zone. The composition of reaction products was analyzed by chromatography. The combustion criterion was the absence of oxygen in the reaction products.

Figure 1 shows the experimental upper bounds of the regions of methane combustion with and without the discharge for ratios of reagents close to partial oxidation (1) and for total energy contributions from the preliminary heating and discharge that correspond to the heating of reagents up to 500–900°C. The ratio of reagents was described by the parameter $S = \dfrac{Q_{CH_4}}{2Q_{O_2}}$ characterizing the deviation of the composition of reagents from the stoichiometry of partial oxidation;

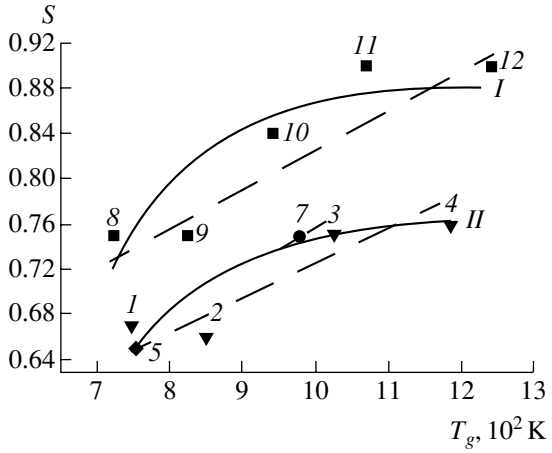

Fig. 1. Boundaries of the combustion region. Experimental points: (*1–4*) for the pulsed setup without a discharge, (*5*) for the steady setup without a discharge, (*7*) for the pulsed setup with preliminary heating and discharge, (*8–12*) for the steady setup with a discharge, without preliminary heating, and with the O_2 content in the process products of (*9*, *12*) 0 and (*8*, *10*, *11*) 0.5–1%. Dashed lines are the linear approximations of experimental dependences, solid lines are the model calculations for (*I*) a methane dissociation degree of 0.25%, E = 12984 K, and ε_2 = –245 kJ/mol and (*II*) E = 14268 K, ε_2 = –353 kJ/mol, and without methane dissociation.

Hydrogen Energy & Plasma Technology Institute, Russian Research Centre Kurchatov Institute, pl. Akademika Kurchatova 1, Moscow, 123182 Russia

1028-3358/03/4803-0119$24.00 © 2003 MAIK “Nauka/Interperiodica”

this parameter is equal to 1 for reaction (1) and decreases to 0.25 with an increase in oxygen content for the complete combustion of methane to produce CO_2 and H_2O. The total energy contribution ε is determined as

$$\varepsilon = \varepsilon_{ph} + \varepsilon_{dis} = \frac{1}{Q}\left(\int_{T_0}^{T_{ph}} C_p(T)dT + W_{dis}\right) = \frac{1}{Q}\int_{T_0}^{T_g} C_p(T)dT, \quad (2)$$

where T_{ph} is the temperature of preliminary heating, W_{dis} is the discharge power, the effective temperature T_g of reagents is determined by the sum of the energy contributions from preliminary heating ε_{ph} and discharge ε_{dis}, and Q is the consumption of reagents. The ratios CO_2/CO and H_2O/H_2 of process products depend on S ($0.25 < S < 1$), and the thermal effect increases with a decrease in S compared to reaction (1), which facilitates the ignition of the combustible mixture.

Figure 1 shows the bounds obtained for the combustion region and experimental points important for the construction of these bounds in the S–T_g coordinates. Combustion arose in particular when transiting between points *1* and *2*, and *3* and *4* (increase in ε_{ph}). Point *5* corresponds to the onset of combustion and is obtained by decreasing the parameter S to the ignition instant with fixed preliminary heating. Since experimental points *1–4* and *5*, which were obtained at different setups, can be approximated by one line, the resulting boundary is independent of the features of a specific setup and is predominantly determined by the properties of the process itself. When the discharge is turned on (points *7–12* in Fig. 1), the combustion boundary is shifted towards lower temperatures and energy contributions. The positive energy effect of the pulsed discharge (point *7*) compared to the equivalent thermal energy contribution is approximately equal to 0.5 J/cm^3. An even stronger effect (up to 2 J/cm^3) was obtained with continuous discharge (points *8–12*).

The above results can be treated in the framework of Semenov's elementary theory [6], where the existence condition of the steady combustion regime is written in the form

$$C_p\rho\frac{dT}{dt} = Q_+ - Q_- = 0, \quad \frac{dQ_+}{dT} = \frac{dQ_-}{dT}, \quad (3)$$

where $Q_+ = \frac{q}{\tau}$ is the energy release in flame, q is the specific heat of the reaction in the combustion zone, $\tau = \tau_0\exp\left(-\frac{E}{T}\right)$ is the characteristic time of the reaction, and Q is the heat transfer from the flame.

The heat transfer is the sum $Q_- = Q_{conv} + Q_{cond}$ of convective $Q_- = Q_{conv} + Q_{cond}$, $Q_{cond} = \alpha\frac{S}{V}(T - T_0)$, $Q_{conv} = \frac{\dot{m}C_p(T - T_g)}{V}$ and conductive losses, where α is the heat transfer coefficient; S and V are the effective area and volume parameters, respectively; T_0 is the temperature of the wall responsible for the conductive heat transfer; T_g is the temperature of reagents entering the flame; $\dot{m} = u\rho S$ is the rate at which reagents enter the flame; and u is the velocity of flame propagation with respect to the gas. A solution of system (3) specifies the existence conditions of the flame under the assumption that reagents are instantaneously mixed in the flame when $T_g \ll E$:

$$\exp\left(-\frac{E}{T_{ef}\left(1 + \frac{T_{ef}}{E}\right)}\right) = \frac{q_{cr}}{q}\left(\frac{T_{ef}}{E}\right)^2, \quad (4)$$

where $q_{cr} = (\alpha + u\rho C_p)\frac{ES\tau_0}{V}$ is the minimum energy release in the flame for which the steady combustion regime is possible, $\beta = \frac{\alpha}{u\rho C_p}$ is the ratio of conductive-to-convective losses, and $T_{ef} = \frac{\beta T_0 + T_g}{1 + \beta}$.

The energy release q in Eq. (4) depends on the composition of the combustible mixture $\left(0.25 < S < 1\right)$ and, for pressure P = const, can be represented in the form

$$q(S) = \frac{n_L 300}{TN_A}\frac{\varepsilon_1 - |\varepsilon_2| + 4S|\varepsilon_2|}{2(2S + 5)}, \quad (5)$$

where n_L is the Loschmidt number. Formula (5) is derived under the assumption that the combustion of a fraction of the methane in oxygen in the flame front for $0.25 < S < 1$, $CH_4 + 2O_2 = CO_2 + 2H_2O$ (with reaction enthalpy ε_1 = 800 kJ/mol) is accompanied by the decomposition of the remaining methane into products with process enthalpy $\varepsilon_2 < 0$.

The effective energy E of combustion activation in the expression $\tau = \tau_0\exp\left(-\frac{E}{T}\right)$ for induction time is determined by kinetic calculations of the ignition of the original mixture for various initial temperatures and various S values (Fig. 2). The role of the plasma in com-

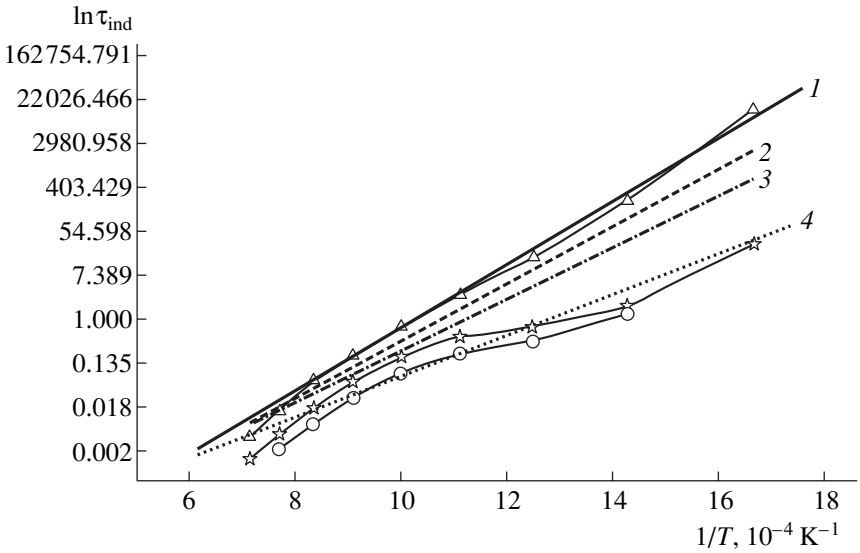

Fig. 2. Combustion induction time τ_{ind} calculated for the methane–air mixture vs. initial temperature T under adiabatic conditions: approximations (*1*) $4.05 \times 10^{-7}\exp\frac{14268}{T}$ for methane dissociation degree α = 0%, (*2*) $8 \times 10^{-7}\exp\frac{12984}{T}$ for α = 0.25%, (*3*) $1.8 \times 10^{-6}\exp\frac{11700}{T}$ for α = 0.5%, and (*4*) $6.93 \times 10^{-6}\exp\frac{9242}{T}$ for α = 1.0%; and (triangles) α = 0%, virtually independent of S, (stars) S = 1 and α = 1%, and (circles) S = 0.6 and α = 1%.

bustion initiation was simulated: calculation was carried out for the partial dissociation of methane into radicals (the dissociation degree was taken to be 0, 0.25, 0.5, and 1%; see Fig. 2). The plasma stimulation of combustion was assumed to reduce to the generation of active particles (radicals and ions). These particles are formed both through the radical mechanism ($CH_4 = CH_3 + H$), e.g., through reactions on the surface of soot particles (C_xH_y), and through ion–molecule reactions (e.g., in reactions with CH_3^+, and $C_2H_5^+$ ions). Calculations were carried out with the special software package Khimicheskiĭ Verstak. The kinetic scheme consisted of more than 400 reactions based on the mechanism that was proposed in [7] and agrees well with experiment in the temperature range 500–1500 K.

Uniting Eq. (5) and solution (4) with an approximation of induction time (Fig. 2), we obtain the theoretical boundaries of the combustion region in S–T_g coordinates (lines *I* and *II* in Fig. 1). Calculations of the thermal case (line *II*) were carried out under the condition that the induction time is given by the approximation $\tau = 4.05 \times 10^{-7} \times \exp\frac{E}{T}$, where $E = E_{therm}$ = 14268 K (Fig. 2), and the energy release of combustion is ε_1 = 800 kJ/mol. The best agreement with experimental results is achieved for a methane-decomposition enthalpy of $\varepsilon_2 = \varepsilon_{2(therm)}$ = –353 kJ/mol. This ε_2 value lies in the range of the possible enthalpy values of methane decomposition processes, in particular, ε_2 = –358 kJ/mol for $CH_4 = \frac{1}{3}C_3 + 2H_2$.

The processing of experiments carried out on the setup with a continuous discharge under the assumption that the plasma generation of active particles affects combustion provides good agreement with experiment (line *II* in Fig. 1) when 0.25% of the methane is dissociated. In this case, $E = E_{dis}$ = 12984 K, and the change in the effective activation energy is $E_{therm} - E_{dis}$ = 1290 K. The enthalpy of the endothermic process is equal to $\varepsilon_2 = \varepsilon_{2(therm)}$ = –245 kJ/mol, which corresponds to the change in enthalpy as soon as in the $CH_4 = \frac{1}{6}C_6 + 2H_2$ reaction. It is seen that the plasma effect promotes both combustion, by reducing its effective activation energy, and decomposition of methane in flame (at lower temperature T_g) similarly to [1–5, 8].

The mechanism for generating active particles by plasma was discussed previously [8]. Even a relatively low effective degree of 0.25% of methane decomposition significantly accelerates the process due to the chain reaction of methane combustion. This value is actually attainable in experiment: the generation of radicals in methane requires ~5–10 eV [8], and the required plasma power is no more than $W \sim$ 70–150 W. Let us consider the mechanism for generating active particles when methane and its derivatives (acetylene) are decomposed on the surface of soot particles, $CH_4 + C(s) = C(s) + C_xH_y$. The growth rate of the

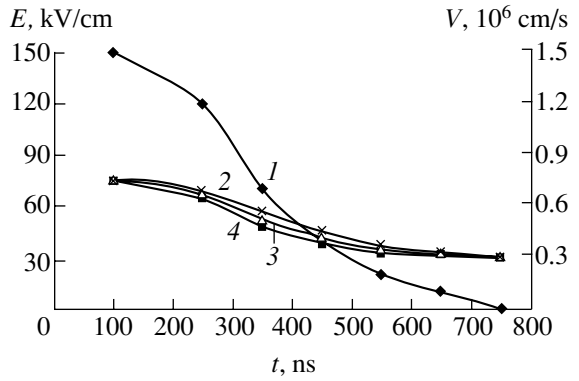

Fig. 3. Time dependence of (*1*) the propagation velocity of the microwave streamer and (*2*, *3*, and *4* for $\beta = 3$, 4, and 5, respectively) the electric field in the streamer head for a radiation pulse duration of 1 μs.

mass of a soot particle is determined as $\frac{dm}{dt} = kSP_{CH_4}$ (g/s), where the rate constant $k = 3.75 \times 10^{-5}\exp\left(-\frac{132\ \text{kJ}}{RT}\right)$ [g/(cm^2 s Pa] is taken from the analysis of experiments on growing pyrocarbon. The contribution of these reactions to the methane balance is $\frac{d[CH_4]}{dt} = -\frac{kSP_{CH_4}n_sN_A}{\mu} = -\frac{kSn_{CH_4}n_sRT}{\mu}$ (cm^{-3} s^{-1}). The characteristic frequency of decomposition on the surface of soot particles is determined by the formula $\omega = kS\frac{RT}{\mu}n_s$ (1/s). Under the assumption that each particle consists of N carbon atoms with the characteristic size $a \sim 1.3$ Å and that the concentration of soot particles is such that $n_s < n^0_{CH_4}N$, the upper bound of this frequency is $\omega \le k\frac{4\pi a^2}{N^{1/3}}\frac{RT}{\mu}n_{CH_4} = (1\text{–}5) \times 10^{-3}$ 1/s. This decomposition rate provides a relative conversion to radicals $1 - \exp(-\omega\tau) \sim 0.05\text{–}0.3\%$ during the time τ for which the particle is in the reactor; i.e., the value necessary for the explanation of experimental data can in principle be achieved.

The significant difference between the efficiencies of the stimulation of combustion by pulsed and continuous discharges is most likely attributable to the different efficiencies of the generation of active particles in the pulsed and continuous modes. The mechanism of dissociation on soot particles for short pulses (1 μs) is inefficient. Let us consider the mechanism of dissociation by an electron impact by using the electric field in the head of the pulsed microwave streamer (Fig. 3), which is determined from photos of the pulsed discharge in air by an image converter. The length of the streamer and its propagation velocity (V in Fig. 3) are measured at various times from the onset of the microwave pulse. In the model proposed in [9], the velocity V is related to the field E in the streamer head as

$$V = 2(D(\nu_i - \nu_a))^{1/2},$$
$$\nu_i - \nu_a = \nu_a\left(\left(\frac{E}{E_{br}}\right)^{\beta} - 1\right), \quad (6)$$

where D is the diffusion coefficient, ν_i is the ionization frequency, ν_a is the adhesion frequency, E_{br} is the breakdown field, and $\beta = 3\text{–}5$ for $E_{br} < E < 5E_{br}$. Substituting the field value $E = 75$ kV/cm at the pulse onset [5] into Eq. (6), one can recalculate the velocity obtained for streamer propagation to the estimated time dependence of the field E (lines *2*–*4* in Fig. 3). The electric field is in the range 30–75 kV/cm, and the concentration of electrons in the streamer is $\sim 10^{12}\text{–}10^{14}$ cm^{-3} [5]. The dissociation rate constant k_d by electron impact for methane $CH_{24} + e \longrightarrow CH_3 + H + e$ is equal to $10^{-11}\text{–}10^{-9}$ cm^3/s (it depends strongly on the number of excited methane atoms). For a 1-μs-long pulse, the fraction of formed radicals is determined from the balance between methane dissociation and recombination of radicals $\delta = \sqrt{\frac{k_d n_e}{k_r n_{CH_4}}} \sim 10^{-3}\text{–}10^{-4}$. Taking into account that the relative pulse duration of the pulsed discharge is equal to 10^3, one obtains a value of $\sim 10^{-6}\text{–}10^{-7}$ for the fraction of decomposed methane, which slightly affects combustion stimulation.

REFERENCES

1. V. D. Rusanov, K. Étivan, A. I. Babaritskiĭ, *et al.*, Dokl. Akad. Nauk **354**, 213 (1997).
2. S. V. Potekhin, B. V. Potapkin, M. A. Deminskiĭ, *et al.*, Khim. Vys. Énerg. **33** (1), 59 (1997).
3. V. D. Rusanov, A. I. Babaritskiĭ, E. N. Gerasimov, *et al.*, Dokl. Akad. Nauk **366** (3), 323 (1999) [Dokl. Phys. **44**, 283 (1999)].
4. A. I. Babaritskiĭ, E. N. Gerasimov, S. A. Demkin, *et al.*, Zh. Tekh. Fiz. **70** (11), 36 (2000) [Tech. Phys. **45**, 1411 (2000)].
5. V. D. Rusanov, A. I. Babaritskiĭ, M. B. Bibikov, *et al.*, Dokl. Akad. Nauk **377** (6), 749 (2001) [Dokl. Phys. **46**, 242 (2001)].
6. I. N. Semenov, *Chain Reactions* (Goskhimtekhizdat, Moscow, 1934).
7. H. Wang and M. Frenklach, in *Proceedings of XXIII Fall Technical Meeting of the Eastern Section of the Combustion Institute, 1990*.
8. A. I. Babaritskiĭ, I. E. Baranov, S. A. Demkin, *et al.*, Khim. Vys. Energ. **33** (6), 458 (1999).
9. V. B. Gil'denburg, I. S. Gushchin, S. A. Dvinin, and A. V. Kim, Zh. Éksp. Teor. Fiz. **97** (4), 1151 (1990) [Sov. Phys. JETP **70**, 645 (1990)].

Translated by R. Tyapaev

Doklady Physics, Vol. 48, No. 3, 2003, pp. 123–125. Translated from Doklady Akademii Nauk, Vol. 389, No. 3, 2003, pp. 328–331.

TECHNICAL PHYSICS

Mechanical Properties of a Material at Ultrahigh Strain Rates Induced by a Laser Shock Wave

D. Batani[1], V. I. Vovchenko[2], G. I. Kanel[3], A. V. Kilpio[2], I. K. Krasyuk[2,*], I. V. Lomonosov[3], Corresponding Member of the RAS P. P. Pashinin[2], A. Yu. Semenov[2,], Academician V. E. Fortov[3], and E. V. Shashkov[2]**

Received December 23, 2002

In this study, the dynamic strength of the AMg6M aluminum alloy at high strain rates is investigated. A method of determining the time when spallation occurs in an opaque material is developed. It is shown that the material is deformed and destroyed through different mechanisms depending on the strain rate. The ultimate value of the dynamic strength of the material under investigation is measured.

1. EXPERIMENT

To determine the dynamic strength of a material, we used the phenomenon of spallation, which arises when the front of a shock wave is reflected from the free surface of a target made of the material under investigation [1]. The shock wave was generated by pulsed laser radiation acting on the face of the target.

Experiments were carried out with two Nd:glass laser setups: Kamerton and Sirius (General Physics Institute, Russian Academy of Sciences). The basic parameters of the Kamerton are 0.53-μm wavelength, 100-J maximum pulse energy, and 2.5-ns pulse duration [2]. The parameters of the Sirius are 1.06-μm wavelength, 60-J maximum pulse energy, and triangular-pulse duration varying between 5 and 80 ns [3].

Laser radiation was focused on a 1-mm-diameter spot on the target. Targets were plates made of the AMg6M aluminum alloy with thickness from 180 to 460 μm. To decrease edge effects, the back of a target had a shoulder 100 μm in height and 1 mm in diameter. To determine the time t_{sp} of spallation, the arrival time of the spall layer t_{arr} at an electric-contact detector was measured by a Tektronix TDS-744A oscilloscope. The target–detector distance was varied between 110 and 880 μm. The spall strength and the time when the spall layer was separated from the target were obtained using the thickness of the spall layer h_{sp} and time t_{arr}, which were measured in each experiment. The features of the shock-wave hardening were studied in experiments with artificial spall layers. In this case, an 8–50-μm-thick aluminum foil was attached with a slight force on the back of the target.

2. SIMULATION

The velocity of a material layer that was separated from the target in the process of spallation was calculated by numerical simulation for each experiment. We developed a one-dimensional unsteady hydrodynamic code [4, 5] based on the numerical calculation of differential equations representing the laws of conservation of mass, momentum, and energy with the wide-range semiempirical equation of state of the material under investigation [6]. The shape of a pressure pulse was assumed to coincide with that of a laser pulse. The relationship between the amplitude of the pressure pulse P_a and the laser pulse intensity I was specified by the similarity relation [7] in the form

$$P_a = AI^m,$$

where the coefficient A and exponent m are determined by particular conditions of the laser action [8].

3. DETERMINATION OF THE SPALLATION TIME t_{sp}

In a target region undamaged after the laser action, the average position of the spallation plane S and the average thickness of the spall layer h_{sp} were measured

[1] *Dipartimento di Fisica "G. Occhialini" and INFM, Universita' degli Studi di Milano-Bicocca, Piazza della Scienza 3, Milano, 20126 Italy*

[2] *General Physics Institute, Russian Academy of Sciences, ul. Vavilova 38, Moscow, 119991 Russia*

[3] *High Energy Density Research Center, IVTAN Scientific Association, Russian Academy of Sciences, ul. Izhorskaya 13/19, Moscow, 127412 Russia*

* *e-mail: krasyuk@kapella.gpi.ru*

** *e-mail: say@lpl.gpi.ru*

1028-3358/03/4803-0123$24.00

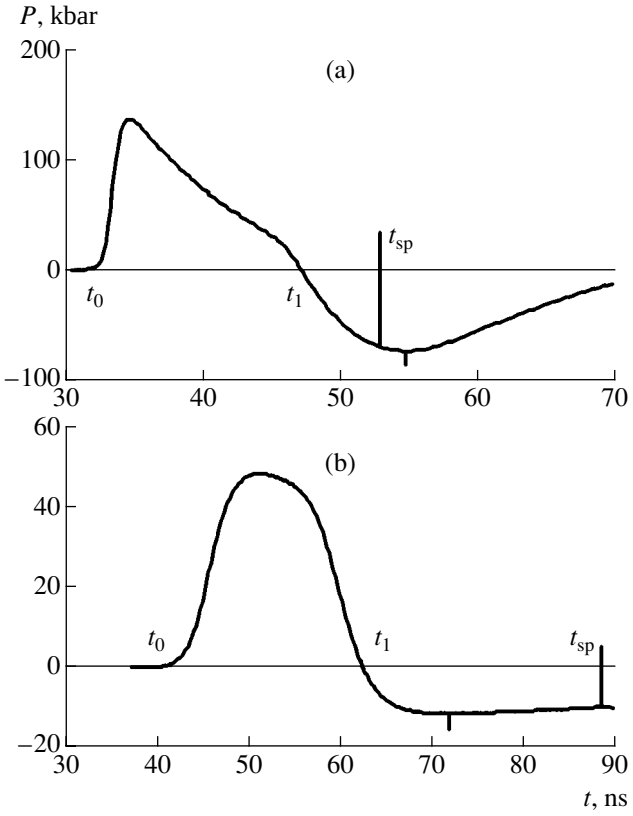

Fig. 1. Pressure profiles in the spallation plane for the (a) dynamic and (b) quasistationary regimes.

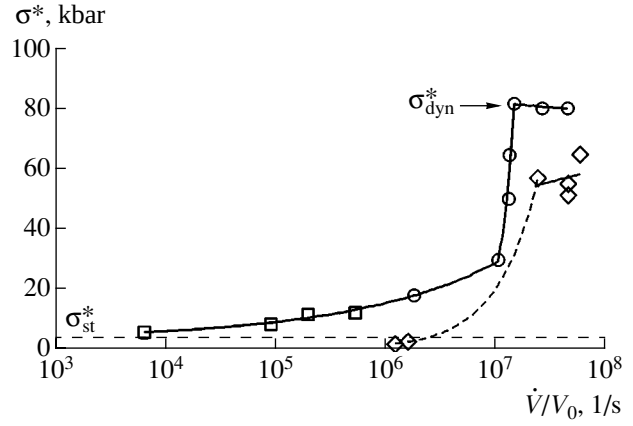

Fig. 2. Spall strength of the AMg6M aluminum alloy as a function of the strain rate in the dynamic regime: (○) laser experiments, (□) explosion experiments [10], and ◇ artificial spall layer.

with a microscope. The spallation time t_{sp} was determined from the nonlinear equation

$$t_{sp} + \frac{L}{v_{sp}} = t_{arr}.$$

Here, L is the distance from the back of the target, where the electric-contact detector was mounted, and the velocity of the spall layer v_{sp} is calculated by the formula

$$v_{sp} = \frac{\int_{t_0}^{t_{sp}} P(t)dt}{m_{sp}},$$

where the pressure profile $P(t)$ in the spallation plane S is calculated numerically, $m_{sp} = \rho_0 h_{sp}$ is the mass per unit area of the spall layer, and the time t_0 corresponds to the onset of the pressure pulse acting in the spallation plane (Fig. 1). Next, we determined the spall strength of the material σ^* by the formula $\sigma^* = P(t_{sp})$. The strain rate of the material in the spallation plane at the time t_{sp}, which can be found by the formula

$$\frac{\dot{V}}{V_0} = \frac{dV/dt}{V_0} = -\frac{d\rho/dt}{\rho_0},$$

was calculated numerically. Here, V is the specific volume, ρ is the density, and the subscript 0 denotes their initial values.

Note that the fracture of the material has a complicated time-extended kinetic character [9]. In this study, it was assumed for simplicity that the spallation occurs instantly when the negative pressure reaches the dynamic strength of the material.

4. RESULTS

In our experiments, we observed two basic modes of deformation in the material under investigation that led to its fracture. They can be defined as dynamic and quasistationary modes. The qualitative difference between these mechanisms is as follows. In the former case, load increases linearly up to fracture. In the latter case, the material expanded rapidly and was then destroyed under a nearly constant load (Fig. 1). Both mechanisms are competitive. The mechanism for which spallation occurs earlier begins first under the given conditions of the shock-wave loading of a sample.

Dynamic deformation mode. The experimental spall strength of the material σ^* as a function of the strain rate $\frac{\dot{V}}{V_0}$ is shown in Fig. 2, where the results of previous explosion experiments [10] are also shown. It is seen that the dynamic strength of the material increases monotonically in this mode up to a strain rate of 10^7 s^{-1} and can be described by the empirical relation

$$\sigma^*[\text{kbar}] = 0.74\left(\frac{\dot{V}}{V_0}\,[1/\text{s}]\right)^{2/9}.$$

Next, the spall strength increases sharply up to $\sigma^*_{dyn} = 80$ kbar and then remains virtually unchanged. This behavior indicates that the dynamic strength of the

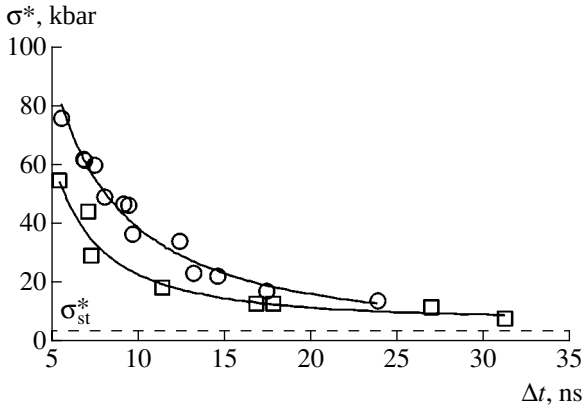

Fig. 3. Spall strength of the AMg6M aluminum alloy as a function of the duration of the tensile stress in the quasistationary regime: (○) laser experiments and (□) artificial spall layer.

material under investigation reaches its ultimate value. A theoretical estimate of the ultimate dynamic strength $\sigma^*_{dyn} \approx 100$ kbar [10] corresponds to the approximation of the simultaneous rupture of all bonds in a solid.

As expected (see, e.g., [11]), the results of experiments with artificial spall layers (except the first two points on the lower curve in Fig. 2) show that the material is hardened in the contact plane between the artificial layer and target surface. The static strength of the material measured in the limit $\frac{\dot{V}}{V_0} \longrightarrow 0$ as $t \longrightarrow \infty$ is equal to $\sigma^*_{st} = 3.4$ kbar [12] and is shown by the horizontal straight line in Fig. 2.

Quasistationary deformation mode. In the experiments, the material is deformed at the initial stage at a rate $\frac{\dot{V}}{V_0}$ exceeding 5×10^7 s^{-1}, and then the material is in an expanded state for a time interval $\Delta t = t_{sp} - t_1$ under a nearly constant load until the fracture of the material (Fig. 1b). Here, t_1 is the time when the pressure becomes negative. The experimental spall strength as a function of the duration of a quasistationary negative pressure pulse is shown in Fig. 3. Data processing by the method of least squares shows that the dynamic strength of the material in this case is almost inversely proportional to the duration Δt of the negative pressure pulse:

$$\sigma^*[\text{kbar}] = 7 \times 10^2 (\Delta t\ [\text{ns}])^{-5/4}.$$

For small Δt values, the spall strength in the quasistationary mode tends to the maximum spall strength in the dynamic mode accessible at large $\frac{\dot{V}}{V_0}$ values. At $\Delta t \longrightarrow 80$ ns, the spall strength tends to its static value $\sigma^*_{st} = 3.4$ kbar. The results of experiments with artificial spall layers (Fig. 3) corroborate that the material is also considerably hardened under the shock-wave action in this case.

Thus, the results of our investigations indicate that, for the first time, we have determined the time of spallation. This made it possible to establish that the material is deformed and destroyed through different mechanisms at high strain rates. The ultimate dynamic strength of the AMg6M aluminum alloy was measured.

ACKNOWLEDGMENTS

This study was performed under the Program of the Russian Academy of Sciences “Physics and Chemistry of the Extreme State of Matter” and was supported by the Russian Foundation for Basic Research, project nos. 00-02-17873 and 00-02-17060.

REFERENCES

1. Ya. B. Zel’dovich and Yu. P. Raizer, *Physics of Shock Waves and High-Temperature Hydrodynamic Phenomena*, 2 vols. (Nauka, Moscow, 1966; Academic, New York, 1966, 1967).
2. A. V. Kilpio, D. G. Kochiev, A. A. Malyutin, *et al.*, Tr. Inst. Obshch. Fiz. Ross. Akad. Nauk **36**, 202 (1992).
3. V. I. Vovchenko, I. K. Krasyuk, P. P. Pashinin, *et al.*, Tr. Inst. Obshch. Fiz. Ross. Akad. Nauk **36**, 5 (1992).
4. A. Yu. Semenov, Zh. Vychisl. Mat. Mat. Fiz. **37** (11), 1376 (1997) [Comput. Math. Math. Phys. **37** (11), 1334 (1997)].
5. A. G. Kulikovskii, N. V. Pogorelov, and A. Yu. Semenov, *Monographs and Surveys in Pure and Applied Mathematics*, Vol. 118: *Mathematical Aspects of Numerical Solution of Hyperbolic Systems* (Chapman & Hall/CRC, Boca Raton, Fl., 2001; Fizmatlit, Moscow, 2001).
6. A. V. Bushman and V. E. Fortov, Usp. Fiz. Nauk **140** (2), 177 (1983) [Sov. Phys. Usp. **26**, 465 (1983)].
7. S. I. Anisimov, A. M. Prokhorov, and V. E. Fortov, Usp. Fiz. Nauk **142** (3), 395 (1984) [Sov. Phys. Usp. **27**, 181 (1984)].
8. V. I. Vovchenko, I. K. Krasyuk, P. P. Pashinin, and A. Yu. Semenov, Dokl. Akad. Nauk **338** (3), 322 (1994) [Phys. Dokl. **39**, 633 (1994)].
9. G. I. Kanel, S. V. Razorenov, A. V. Utkin, and V. E. Fortov, *Shock-Wave Phenomena in Condensed Media* (Yanus-K, Moscow, 1996).
10. G. I. Kanel and V. E. Fortov, Usp. Mekh. **10** (3), 3 (1987).
11. G. I. Kanel, S. V. Razorenov, A. V. Utkin, and V. E. Fortov, Mekh. Tverd. Tela, No. 5, 173 (1999).
12. *Handbook of Physical Quantities*, Ed. by I. S. Grigoriev and E. Z. Meilikhov (Énergoatomizdat, Moscow, 1991; CRC Press, Boca Raton, Fl., 1997).

Translated by Yu. Vishnyakov

Doklady Physics, Vol. 48, No. 3, 2003, pp. 126–130. Translated from Doklady Akademii Nauk, Vol. 389, No. 1, 2003, pp. 49–54.

MECHANICS

Physical Features of High-Velocity Interaction of Elongated Technogenic Fragments with Constructions

A. V. Radchenko*, Academician V. E. Fortov, and I. E. Khorev*****

Received October 3, 2002

During the last four decades, the extension of humanity's activity in space has been accompanied by the continuous increase in the accumulation of various fragments in the Earth's environment. Among these fragments are satellites that have ceased operation, the last stage of rockets, elements of systems that separate satellites from rockets, acceleration blocks, wreckage of satellites and rockets formed as a result of accidental or planned explosions, etc. All these fragments accumulated in near-Earth orbits make up the so-called space garbage, whose excessive abundance presents a real and current danger for various spacecraft and for the lives of astronauts [1, 2]. Fragments of technogenic garbage have wide spectra of masses, shapes, and velocities of their collisions with launched space objects. The possible velocities of overtaking and head-on collisions with active spacecraft vary in a wide interval (from 0 to 15 km/s). It is physically clear that the frontal impact of dense high-strength elongated fragments with a spacecraft is most dangerous.

This work is devoted to the physicomathematical simulation of the processes of high-velocity impact of elongated fragments with various targets imitating the protection of space objects.

Experimental investigations were carried out on special benches with gunpowder and light-gas ballistic setups for throwing various models of technogenic fragments, with further analysis of saved samples [3, 4]. The velocity of impacting bodies was measured by an inductive velocity transmitter with an accuracy of 0.2%. As fragments we used high-strength steel (HRC = 64–68) elongated pointed impacting bodies with diameter d =10.9 mm, length $l = 3.3d$, and weight 19.5 g. The head part of the impacting bodies, with a height of $h = 2.4d$, was formed by the arc with radius $r = 6.2d$. In order to conserve the integrity of impacting bodies being thrown and to increase their piercing and penetrating capabilities, they were placed in a soft bimetallic shell with a diameter of 12.7 mm. The total weight of a fragment was equal to 31.6 g. Monolithic and shielded obstacles of various strengths were used as targets. Steel plates with Brinell hardnesses of HB = 170, 300, and 440 kgf/mm^2 were used as massive obstacles. Steel and lead plates of various thicknesses were used as shields.

The first run of experiments was carried out for studying the features of the penetration of high-strength elongated fragments into massive targets in a wide range of collision velocities. Figure 1 shows the experimental dependence of the crater (penetration) depth L_k on the impact velocity for obstacles with HB = (*1*, circles) 170, (*2*, crosses) 300, and (*3*, triangles) 440 kgf/mm^2. As follows from the results, the velocity dependences of the crater depth are complex and consist of three substantially different regions.

(i) The collision region with relatively low velocities. In this region, impacting bodies penetrating into a

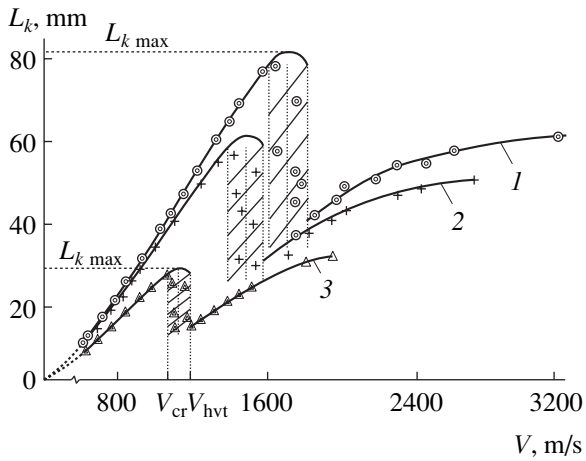

Fig. 1. Crater depth vs. the impact velocity of a technogenic fragment for obstacles with HB = (*1*, circles) 170, (*2*, crosses) 300, and (*3*, triangles) 440 kgf/mm^2.

* *Institute of Strength Physics and Materials Science, Siberian Division, Russian Academy of Sciences, Akademicheskiĭ pr. 2/1, Tomsk, 634055 Russia*
e-mail: andrew@tsc.tomsk.ru

** *Institute of High Temperatures Scientific Association (IVTAN), Russian Academy of Sciences, Izhorskaya ul. 13/19, Moscow, 127412 Russia*
e-mail: fortov@ras.ru

*** *Tomsk University of Control Systems and Radioelectronics, pr. Lenina 40, Tomsk, 634050 Russia*

1028-3358/03/4803-0126$24.00

target are only elastically deformed and do not fail. In penetration curves $L_k(V_0)$, this behavior corresponds to the region of sharp increase in the crater depth with an increase in the impact velocity up to a certain maximum depth $L_{k\max}$ determined by the ratio of the strength parameters of a fragment–obstacle pair [4].

(ii) The region of critical interaction velocities. For impact velocities $V_0 > V_{cr}$, penetration depth for all obstacles does not increase with collision velocity in a narrow range of interaction velocities. For $V_0 = V_{cr}$, impacting bodies begin to be irreversibly deformed and to undergo brittle failure. This behavior was first observed and reported in [5, 6], where it was shown that the relative penetration depth of copper, steel, and tungsten carbide balls into a lead half-space decreases due to the deformation (flattening) of the balls and that the transverse diameter increases, which leads to a sharp increase in the resistance force and, therefore, to a decrease in penetration depth. This behavior corresponds to the local bend in the penetration curves. Experiments indicate that initial failure usually arises in the base of the head part of a fragment or in sections close to it [4]. As collision velocity increases, the failure nucleation site propagates to the impacting body vertex. Since the strength parameters of the impacting body and obstacle are statistically distributed, various technological factors exist, and impacting bodies inevitably undergo nutation, the failure process is stabilized in a certain range of impact velocities (it is shaded in Fig. 1). In this case, crater depth decreases sharply until velocity reaches the value V_{hvt}, called the high-velocity threshold in [4].

(iii) The region of hydrodynamic collision velocities. In this region ($V_0 > V_{hvt}$), penetration depth increases again with impact velocity, and this increase retards as velocity increases. The curve $L(V_0)$ has a point of inflection, and its upper branch (realized in experiments) is convex, in contrast to the first region. The failure of the impacting body has the character of stable wear, and the process of crater formation can be treated as "inflowing" of a variable-mass body into an obstacle.

As follows from the extrapolation of line *1* to the region of high impact velocities in Fig. 1, the maximum penetration depth (80 mm) reached for an impact velocity of 1.6 km/s will be reached again only for a comparatively high collision velocity of 7 km/s (about orbital velocity) even for the lowest strength obstacle. Therefore, high-strength elongated fragments are most dangerous in frontal impacts with comparatively low collision velocities (overtaking courses) up to 2–2.5 km/s.

It is known that the most efficient protection against high-velocity impacts with compact fragments is a shielded construction, i.e., the use of thin shields placed in front of the basic obstacle (Whipple effect) [7]. In this case, the shield breaks an impacting body into smaller fragments, and a dispersed impact with a significantly smaller penetration depth occurs instead of a concentrated impact.

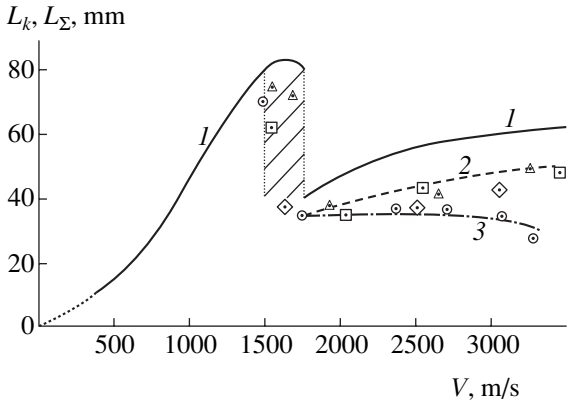

Fig. 2. Total penetration depth vs. the impact velocity of a technogenic fragment on shielded obstacles with HB = (*1*, circles) 170, (*2*, crosses) 300, and (*3*, triangles) 440 kgf/mm^2.

The second run of experiments was carried out to reveal the effect of shields on the damage of massive obstacles by the same elongated fragments in a frontal impact. Steel plates (HB = 170 kgf/mm^2) 5, 10, and 15 mm in thickness and 5-mm-thick lead plates were used as shields. To ensure the outlet of a whole impacting body from a shield, shields were placed at a distance of 50 mm from the face surface of a massive obstacle. Figure 2 shows the results for the estimated total penetration depth L_Σ (shield thickness plus penetration depth into massive targets) compared to the first-run experiments on the penetration of the same fragments into unshielded targets. The experiments show that the total penetration depth into shielded obstacles [line *2*, shield thickness of (square) 5, (triangle) 10, and (diamond) 15 mm] is smaller (by 20% on average) than the penetration depth into unshielded targets (line *1*) for hydrodynamic velocities and that the shield thickness does not substantially affect the total penetration depth. Lead shields (line *3*; squares correspond to a 5-mm-thick lead shield) were found to have an increased efficiency for high impact velocities of about 3 km/s, which is associated with the increased destructive capability of dense materials (lead, tungsten, gold, uranium, etc.). In the collision region with relatively low velocities, i.e., until the onset of the failure of impacting bodies, lines *1–3* coincide with each other. It was shown that fragments begin to fail on lead shields at lower collision velocities than on steel shields, because the density of lead is higher, and a lead obstacle therefore acts with a higher resistance force against the penetration of an impacting body [5, 6].

Since such experiments are expensive, it is of interest to simulate this complex process on a computer in order to obtain missing information immediately from the region of high-velocity deformation and failure of interacting bodies.

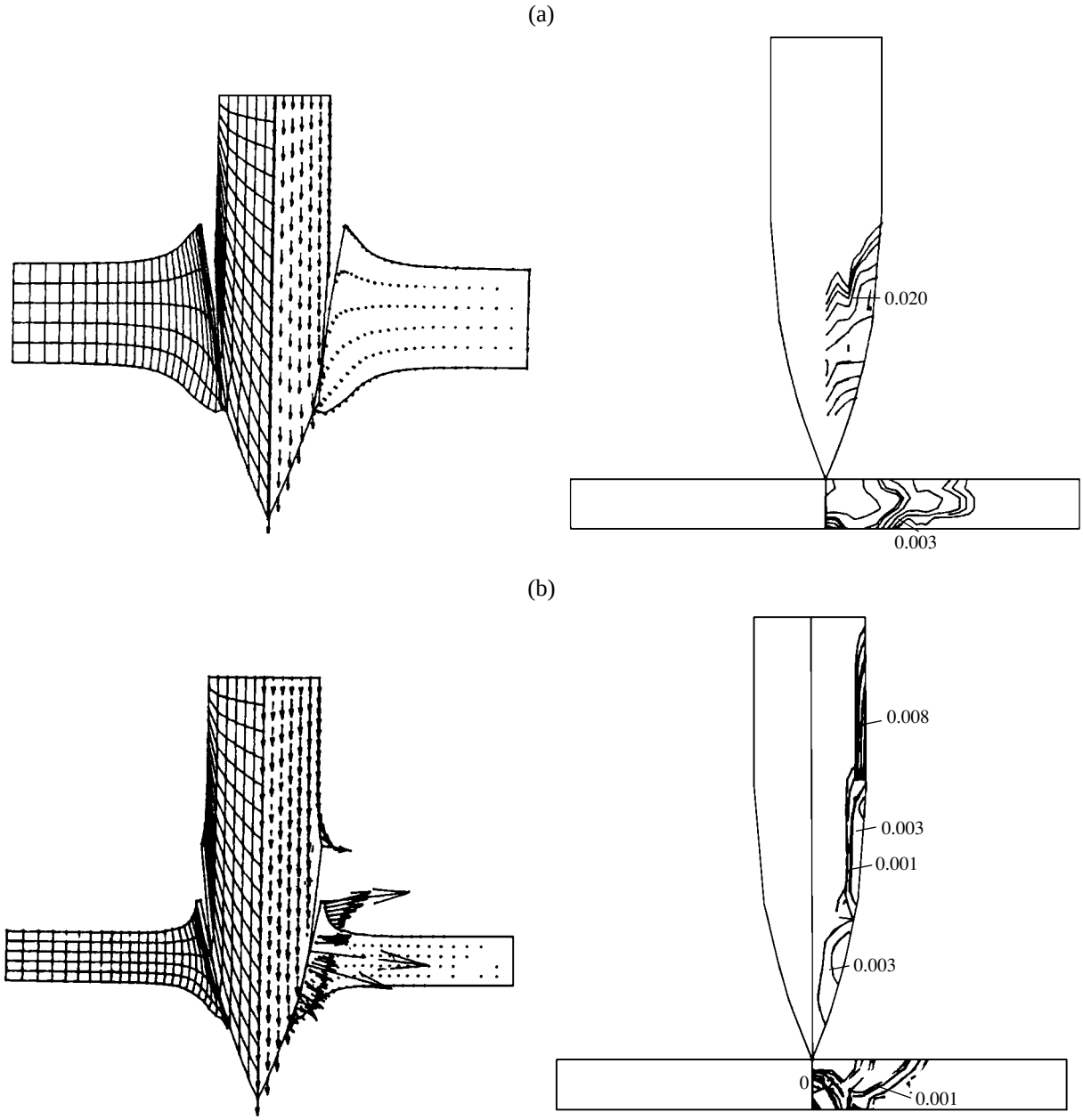

Fig. 3. Configurations of an impacting body and shield with the contours of the specific volume of cracks for an impact velocity of (a) 0.8 and (b) 1.5 km/s and a shield thickness of (a) 10 and (b) 5 mm at t = (a) 37 and (b) 12 μs.

The behavior of interacting bodies is mathematically described by using the model of a damaged medium, which implies the presence of microcavities (pores and cracks) [8–10]. The total volume W of this medium is the sum of the volume W_c of the undamaged part of the medium with the density ρ_c and the volume W_* of microcavities, where density is taken to be equal to zero. The average density of the damaged medium is related to the introduced parameters as $\rho = \rho_c \frac{W_c}{W}$. The degree of medium damage is characterized by the specific volume of microdamages $V_* = \frac{W_*}{W\rho}$. The set of equations describing the unsteady adiabatic motion of this medium involves the equations of continuity, motion, energy, and the master equation of the variation of the specific volume of microdamages [9]. Numerical simulation is carried out by the modified finite-element method in the axisymmetric formulation [10–13].

Figure 3 shows configurations calculated for an elongated fragment and shields with the contours of the specific volume of cracks for an impact velocity of (a) 0.8 and (b) 1.5 km/s and a shield thickness of (a) 10

and (b) 5 mm. Analysis of contours for the specific volume of cracks shows that the degree of damage for a collision velocity of 0.8 km/s is insufficient for the appearance of macrocracks responsible for the division of the head of an impacting body into parts. As impact velocity increases, the development of damage of the fragment-head material changes its qualitative character. The evolution of microdamages in the impacting body indicates that the nucleation site of damage rises to 11 μs. It is located in the head part on the symmetry axis and appears due to the interaction between off-loading waves propagating from the lateral surfaces of the head of the impacting body that partially penetrates beyond the rear surface of the plate. To a time of 12 μs, damage nucleation sites appear over the entire lateral surface of the impacting body, and the degree of the damage of its material is maximal over the perimeter of the base of the head. Cracks nucleating on the lateral surface of the fragment propagate rapidly in depth. The development of cracks is accompanied by intense shear deformations resulting in the division of the head of the impacting body into fragments. Thus, calculations show that the failure of an impacting body penetrating through shields is most intense near the base of its head due to simultaneous intense tensile and shear deformations.

Figure 4a shows the time dependences of the resistance forces against the penetration of the impacting body (line *1*) with a velocity of 0.8 km/s into 10-mm-thick shields and with a velocity of (*2*) 1.5, (*3*) 2, and (*4*) 2.5 km/s into 5-mm-thick shields. For a velocity of 0.8 km/s, the resistance force increases monotonically until 18 μs due to the monotonic increase in the contact area between the head of the impacting body and the shield. From 18 to 26 μs, the resistance force decreases rapidly by 60%, because the head of the impacting body emerges from the rear side of the shield. From 26 to 29 μs, the resistance force increases again by 50% due to intense off-loading waves in the head of the impacting body, which penetrates behind the rear surface of the shield. After 29 μs, as the head of the impacting body leaves the shield, the resistance force decreases rapidly. The resistance force changes its behavior when the impact velocity increases by a factor of 2 or more. Lines *2*–*4* involve four characteristic regions. In the first region, the resistance force increases due to an increase in the body–shield contact area. In the second region, whose length decreases with an increase in velocity, the dependence of the resistance force is sinusoidal curves whose half-period varies from 4 μs for a velocity of 1.5 km/s to 1 μs for a velocity of 2.5 km/s. The behavior of the resistance force in this region is considerably determined by wave effects in the shield and impacting body. In the third region, the resistance force decreases by more than half, because the head of the impacting body penetrates behind the rear side of the shield. In the last, fourth, region, the resistance force increases rapidly. For a maximum impact velocity of 2.5 km/s, this increase begins at the earliest time of 7.5 μs and is the fastest. Comparison between Figs. 3 and 4 shows that the fourth region of the dependence of the resistance force coincides with the onset of the stage of intense fragment deformation. This deformation leads to the failure of the head of the fragment. In Fig. 3 (for a velocity of 1.5 km/s), the generatrix of the surface of the impacting body has a pronounced bend in the base of its head, which is caused by an increase induced in the volume of this part due to the off-loading of the material.

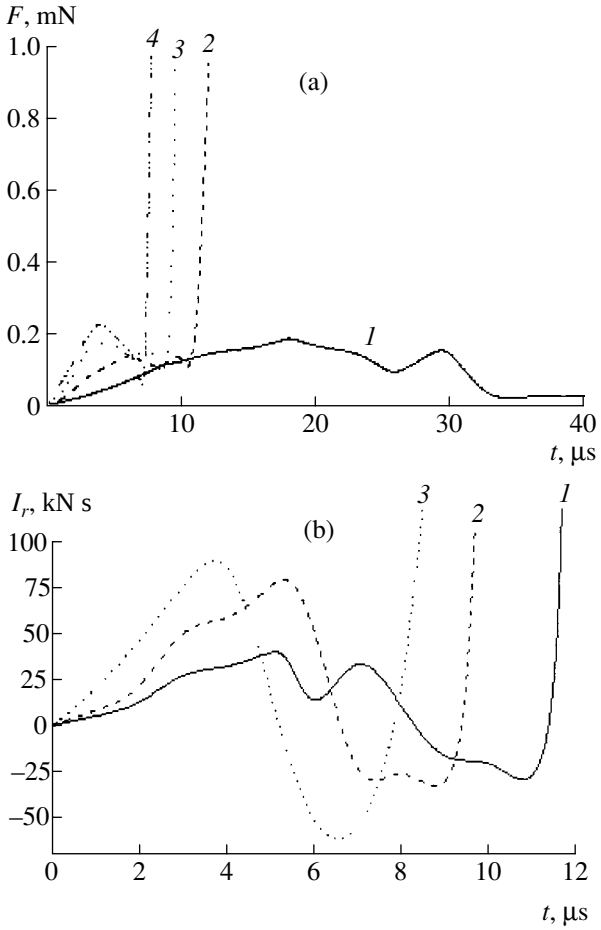

Fig. 4. Time dependences of (a) the resistance force of the shield and (b) the rate of variation of the radial momentum of the impacting body (line *1*) with a velocity of 0.8 km/s for 10-mm-thick shields and with a velocity of (*2*) 1.5, (*3*) 2, and (*4*) 2.5 km/s for 5-mm-thick shields.

The effect of various factors on the penetration of a fragment into a 5-mm-thick plate can be clearly revealed by analyzing the time dependence of the derivative of the radial momentum of the impacting body (Fig. 4b, where lines *1*, *2*, and *3* correspond to velocities 1.5, 2, and 2.5 km/s, respectively). These curves illustrate the radial vibrations of the material in the process of penetration and the wave character of the body–shield interaction. There are three characteristic time regions in these curves: in the first, second, and third regions, the radial momentum increases monotonically,

decreases, and increases rapidly, respectively. The variation rate of the derivative of the radial momentum is maximal in the third region. These three time regions are most pronounced in curve *3* for a collision velocity of 2.5 km/s. Comprehensive analysis of the above calculations shows that the derivative of the radial momentum changes its sign at the second stage due to the intense off-loading wave in the head of the impacting body, which has penetrated beyond the rear side of the shield. As a result, after a short-term decrease in interaction intensity, which is caused by disagreement between the radial vibrations of the shield and impacting body, they gain opposing radial velocities in the contact region, and a head-on collision occurs. This collision leads to a sharp increase in the interaction force, which is manifested in the unusual sharp increase in all time dependences of the resistance forces. In this interval, the maximum diameter of the cylindrical part of the impacting body increases sharply by 8–10%. The contact area increases as diameter squared, and the mass of the shield material that resists the penetration of the impacting body is proportional to the third power of the diameter. As a result, this behavior leads to a short-term (0.5–1 μs) sharp increase in the resistance force. As was mentioned above, this increase in the interaction force is responsible for rapid accumulation of damage in the head of the fragment and finally for its fragmentation.

Thus, complex experimental and theoretical investigations of the interaction of high-strength elongated fragments with shielded obstacles show conclusively that models of the piercing of shielded obstacles must take into account the failure of not only obstacles but also impacting bodies. Special attention must be concentrated on the development of physicomathematical models of the joint interaction of the flux of fragments and fragments of the impacting body with an obstacle after shield piercing [13].

ACKNOWLEDGMENTS

This work was supported by the Russian Foundation for Basic Research, project nos. 00-01-00552 and 00-01-00766.

REFERENCES

1. E. I. Grinberg, Priroda (Moscow), No. 8, 12 (1992).
2. M. N. Vlasov and S. V. Krichevskiĭ, *Ecological Danger of Space Activity* (Nauka, Moscow, 1999).
3. *Ballistic Sets and Their Application in Experimental Research*, Ed. by N. A. Zlatin and G. I. Mishin (Nauka, Moscow, 1974).
4. V. M. Zakharov and I. E. Khorev, in *Proceedings of II All-Russia Conference on Detonation, Chernogolovka, 1981*, p. 153.
5. F. F. Vitman and N. A. Zlatin, Zh. Tekh. Fiz. **33** (8), 982 (1963) [Sov. Phys. Tech. Phys. **8**, 730 (1964)].
6. L. V. Belyakov, F. F. Vitman, and N. A. Zlatin, Zh. Tekh. Fiz. **33** (8), 990 (1963) [Sov. Phys. Tech. Phys. **8**, 736 (1964)].
7. F. I. Whipple, *Vistas in Astronautics 1958* (Pergamon Press, New York, 1958), pp. 115–119.
8. V. A. Gorel'skiĭ, A. V. Radchenko, and I. E. Khorev, Izv. Ross. Akad. Nauk, No. 6, 185 (1998).
9. G. I. Kanel, S. V. Razorenov, A. V. Utkin, and V. E. Fortov, *Shock-Wave Phenomena in Condensed Media* (Yanus-K, Moscow, 1996).
10. G. R. Johnson, J. Appl. Mech. **44** (3), 95 (1977).
11. A. V. Radchenko, S. V. Kobenko, I. N. Marzenyuk, *et al.*, Int. J. Impact Eng. **23**, 745 (1999).
12. A. V. Radchenko and S. V. Kobenko, Dokl. Akad. Nauk **373** (4), 479 (2000) [Dokl. Phys. **45**, 397 (2000)].
13. I. E. Khorev, S. A. Zelepugin, A. A. Konyaev, *et al.*, Dokl. Akad. Nauk **369** (4), 481 (1999) [Dokl. Phys. **44**, 818 (1999)].

Translated by R. Tyapaev

Doklady Physics, Vol. 48, No. 3, 2003, pp. 131–133. Translated from Doklady Akademii Nauk, Vol. 389, No. 2, 2003, pp. 180–183.

MECHANICS

Developing the Concept of the Strain Rate Intensity Factor in Plasticity Theory

S. E. Aleksandrov*, R. V. Goldshteĭn, and E. A. Lyamina

Presented by Academician A.Yu. Ishlinskiĭ November 18, 2002

Received November 29, 2002

In the theory of ideal plasticity, the strain rate intensity factor was introduced in [1] on the basis of analysis of the singular behavior of a velocity field near a maximum friction surface on which the following condition is satisfied:

$$\tau_f = k_0, \tag{1}$$

where τ_f are the specific friction forces and k_0 = const is the yield point in the case of simple shear. In [2], it was shown that there is a fairly complete formal analogy between the strain rate intensity factor in plasticity theory and the stress intensity factor in elasticity theory. In particular, the strain rate intensity factor K_e is determined from the following representation of the equivalent strain rate near a maximum friction surface:

$$\xi_{eq} = \frac{K_e}{s^{1/2}} + o\left(\frac{1}{s^{1/2}}\right), \tag{2}$$

where s is the distance along the normal from the friction surface. From Eq. (2), it follows that the strain rate intensity factor has the dimension

$$K_e\ [\mathrm{m}^{1/2}\ \mathrm{s}^{-1}]. \tag{3}$$

An equivalent strain rate is used in numerous models that are generalizations of a rigid/perfectly plastic material and, in particular, in master equations describing the evolution of different properties of the material. From Eq. (2), it follows that the equivalent strain rate increases rapidly when approaching the friction surface. Therefore, the properties of the material must be characterized by a significant gradient near this surface, which is in good agreement with many experimental data [3, 4]. It should be noted that, if the value of ξ_{eq} is sufficiently large, the resistance of the material in the process of inelastic deformation depends on ξ_{eq} even for cold treatment [5]. Since $\xi_{eq} \longrightarrow \infty$ as $s \longrightarrow 0$, master equations are meaningless for material points moving along the friction surface. In the theory of cracks, which is based on linear elasticity theory, an analogous situation arises when the behavior of a solution is analyzed near the crack tip. Since stresses tend to infinity at the crack tip, any criterion for stresses predicts fracture, and any condition of yielding predicts the formation of a plastic zone near the crack tip for arbitrarily small loads. One of the possible methods of predicting fracture at the crack tip in the framework of linear plasticity theory is extensively used in applications and includes a fracture criterion based on the stress intensity factor [6, 7]. The stress intensity factor can also be applied to evaluate the size of the plastic zone [7], as well as to construct similarity conditions for both brittle and plastic fracture [8]. In this study, we suggest that the last method be generalized and that the strain rate intensity factor be used to estimate layer thickness near a maximum friction surface, where intense processes caused by a high strain rate occur. An approach that is based on classical boundary-layer theory and considers a rigid/perfectly plastic material was developed in [9, 10] to obtain solutions near friction surfaces. However, the singular character of the velocity field near maximum friction surfaces was not taken into account in those studies. The effect of such a behavior was not analyzed in the framework of the above theories.

One of the simple viscoplastic models is determined by the yielding condition

$$k = k_0\left(1 + \frac{\xi_{eq}}{\xi_0}\right) \tag{4}$$

and the yielding law related to this condition. In this equation, ξ_0 = const is a certain characteristic strain rate. For an infinitesimal strain rate, Eq. (4) tends to the yielding condition of an ideal plastic material. In addition, relation (4) coincides with this condition for $\xi_0 \longrightarrow \infty$. Thus, when the ideal plastic model is applicable, ξ_0 must be sufficiently large. From Eq. (4), it follows that ξ_0 has the dimension

$$\xi_0\ [\mathrm{s}^{-1}]. \tag{5}$$

From Eqs. (3) and (5), the characteristic length for a

Institute for Problems of Mechanics,
Russian Academy of Sciences,
pr. Vernadskogo 101, Moscow, 117526 Russia
** e-mail: salex@ipmnet.ru*

1028-3358/03/4803-0131$24.00

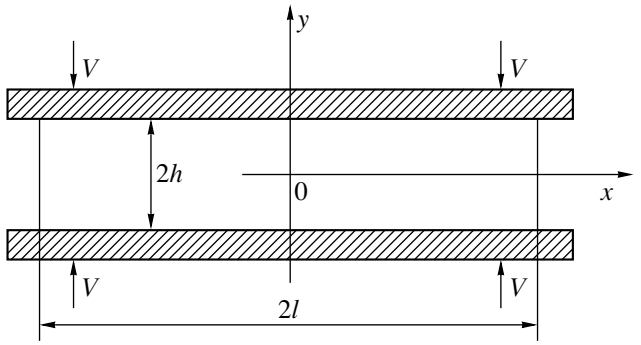

Fig. 1.

given process and a given material can be determined as

$$L = \left(\frac{K_e}{\xi_0}\right)^2. \quad (6)$$

Hence, it is seen that the characteristic length is small for large ξ_0 values, which is in qualitative agreement with the available experimental data. For example, it was shown in [4] that, for the plane extrusion of an aluminum alloy, the thickness of a layer in which significant structural modifications of the material occur is about 200 μm for a characteristic thickness of the deformed zone of 3 mm. Assuming (by analogy with fracture mechanics) that there is a certain critical value K_e^{cr} of the factor K_e and taking $K_e = K_e^{cr}$, we find from Eq. (6) that the characteristic length for this material is

$$L_m = \left(\frac{K_e^{cr}}{\xi_0}\right)^2. \quad (7)$$

In most cases, the parameters of viscoplastic models are obtained at elevated temperatures. To apply the method proposed, it is necessary to know the quantity ξ_0 in the processes of the cold pressing of metals. Experimental investigations of the behavior of stress–strain curves in a wide range of the strain rate under conditions of cold deformation were generalized in [5]. Using these curves and assuming that relation (4) is valid, one can estimate ξ_0. In particular, the data presented for aluminum in [5] for the equivalent strain rate in the range $10^{-4} \le \xi_{eq} \le 10^4$ show that, for the deformations developed when the stress–strain curves tend to the horizontal asymptotes, ξ_0 is about 2×10^4 s^{-1}. Using this value and the strain rate intensity factor found from the model of an ideal plastic material, one can evaluate the thickness of the layer of large shear strains from Eq. (6). If K_e^{cr} can be found from an independent experiment, Eq. (7) makes it possible to determine L_m.

As an example, we consider one of the well-known problems in classical plasticity theory: compression of a layer between rough plates (the Prandtl problem). The solution to this problem is available, for example, in [11]. The geometry of the process is schematically shown in Fig. 1. It is assumed that the maximum friction law is valid on the plate surfaces $y = \pm h$. In the Cartesian coordinate system xy, the velocity-vector components u_x and u_y are determined by the equations

$$\frac{u_x}{V} = \frac{\pi}{2} - \frac{l}{h} + \frac{x}{h} - 2\left(1 - \frac{y^2}{h^2}\right)^{1/2}, \quad \frac{u_y}{V} = -\frac{y}{h}. \quad (8)$$

Here, V is the velocity of the plates, l is the half-width of the plastic layer, and h is the half-thickness of the plastic layer. From Eq. (8), it is possible to find the shear strain rate ξ_{xy} in the form

$$\xi_{xy} = \frac{V}{h} y (h^2 - y^2)^{-1/2}. \quad (9)$$

From this expression, it follows that $\xi_{xy} \longrightarrow \infty$ as $y \longrightarrow h$. Since the remaining components of the strain-rate tensor are finite, Eq. (9) determines the behavior of the equivalent strain rate near a maximum friction surface. By definition, $\xi_{eq} = \left[\frac{2}{3}\xi_{ij}\xi^{ij}\right]$. Consequently, from Eq. (9), we have

$$\xi_{eq} = \sqrt{\frac{2}{3}}\frac{V}{\sqrt{h}}(h - y)^{-1/2} + o[(h - y)^{-1/2}], \quad (10)$$

as $y \longrightarrow h$. Taking into account that $s = h - y$ in the case under consideration and comparing Eq. (10) with Eq. (2), we obtain

$$K_e = \sqrt{\frac{2}{3}}\frac{V}{\sqrt{h}}. \quad (11)$$

Substituting Eq. (11) into Eq. (6), we determine the characteristic size of the large-strain zone:

$$L = \frac{2}{3}\frac{V^2}{h\xi_0^2}. \quad (12)$$

The characteristic value of the velocity V depends on the type of forge-and-pressing machine. In particular, $V = 0.2$, 0.4, 7, and 18 m/s for hydraulic presses, crank mechanisms, rotary-type machines, and hammers, respectively [12]. Taking into account these V values and using the previously obtained ξ_0 value, we can determine from Eq. (12) the relative thickness of the layer of large strains as a function of the thickness of the deformed layer. This function is shown in Fig. 2 for (curve *1*) hydraulic presses and (curve *2*) crank mechanisms and in Fig. 3 for (curve *1*) rotary-type machines and (curve *2*) hammers. As is seen from Figs. 2 and 3, in the range of sample thicknesses under consideration for all types of machines (except for hammers), the thickness of the layer of large strains is much less than the characteristic size h for this process. In the case of treatment by hammers, the thickness of the large-strain layer is comparable with and much less than the char-

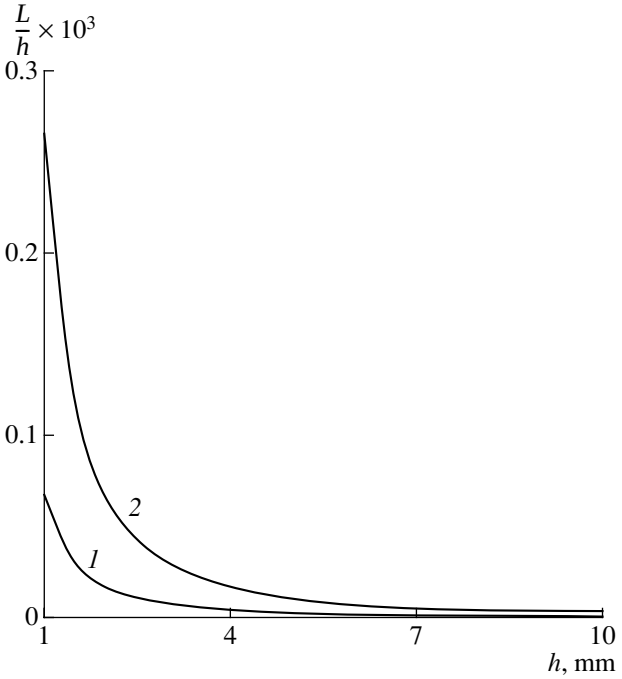

Fig. 2.

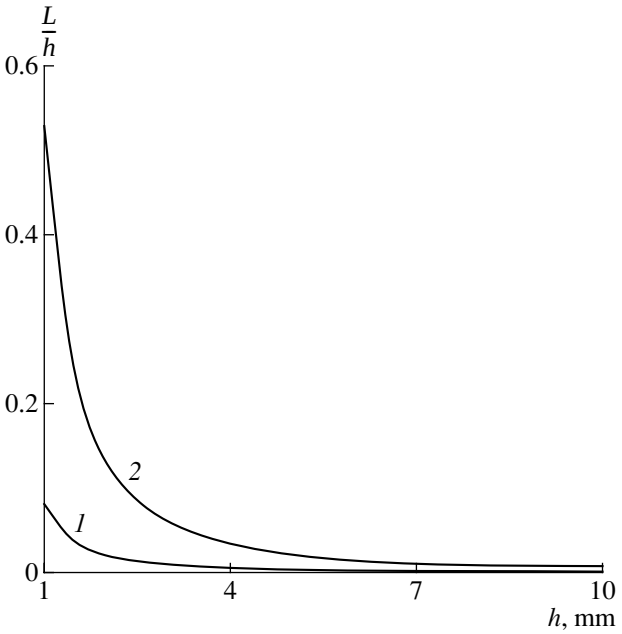

Fig. 3.

acteristic length of the process for deforming sufficiently thin and relatively thick samples, respectively.

When deformation happens at high temperatures, ξ_0 decreases. For example, for an aluminum alloy [13], it was found that $\xi_0 = 220\ s^{-1}$ at typical temperatures for hot pressing. Apparently, under these conditions, the ratio $\frac{L}{h}$ increases by several orders of magnitude, so that the theory proposed above will be inapplicable for a wider velocity range than in the case of cold treatment. On the other hand, the theory can be extended to some incompressible materials, whose yield conditions depend on average stress. In particular, as was shown in [14], for materials satisfying the double-shear model [15], the behavior of the equivalent strain rate near a maximum friction surface is also described by Eq. (2).

ACKNOWLEDGMENTS

This work was supported by the Russian Foundation for Basic Research, project nos. 02-01-00419 and 02-01-06180.

REFERENCES

1. S. Alexandrov and O. Richmond, Int. J. Nonlinear Mech. **36** (1), 1 (2001).
2. S. Alexandrov, *Interrelation between Constitutive Laws and Fracture in the Vicinity of Friction Surfaces. Physical Aspects of Fracture* (Kluwer, Dordrecht, 2001), pp. 179–190.
3. R. E. Dutton, R. L. Goetz, S. Shamasundar, and S. L. Semiatin, Trans. ASME: J. Manuf. Sci. Eng. **120** (4), 764 (1998).
4. T. Aukrust and S. Lazghab, Int. J. Plast. **16** (1), 59 (2000).
5. A. G. Atkins, J. Inst. Met. **97**, 289 (1969).
6. G. I. Barenblatt, Prikl. Mat. Mekh. **22** (3), 434 (1959).
7. G. R. Irwin, in *Handbuch der Physic* (Springer-Verlag, Berlin, 1958), Vol. 6, pp. 551–590.
8. V. M. Vainshel'baum and R. V. Gol'dshtein, Izv. Akad. Nauk SSSR, Mekh. Tverd. Tela, No. 1, 78 (1978).
9. J. G. Oldroyd, Proc. Cambridge Philos. Soc. **43**, 383 (1947).
10. L. M. Flitman, Prikl. Mat. Mekh. **49** (4), 663 (1985).
11. L. M. Kachanov, *Foundations of Plasticity Theory* (GITTL, Moscow, 1956).
12. A. N. Banketov, Yu. A. Bocharov, N. S. Dobrinskiĭ, E. N. Lanskoĭ, V. F. Preis, and I. D. Trofimov, *Forge-Stamping Equipment* (Mashinostroenie, Moscow, 1970).
13. N. Cristescu, Int. J. Mech. Sci. **17**, 425 (1975).
14. S. E. Aleksandrov and E. A. Lyamina, Dokl. Akad. Nauk **383**, 492 (2002) [Dokl. Phys. **47**, 271 (2002)].
15. A. J. M. Spencer, *Deformation of Ideal Granular Materials. Mechanics of Solids* (Pergamon Press, Oxford, 1982), pp. 607–652.

Translated by Yu. Vishnyakov

Doklady Physics, Vol. 48, No. 3, 2003, pp. 134–137. Translated from Doklady Akademii Nauk, Vol. 389, No. 2, 2003, pp. 184–188.

MECHANICS

Method of Factorizing a Solution to Some Boundary-Value Problems

Academician V. A. Babeshko and O. M. Babeshko

Received November 25, 2002

Three-dimensional boundary-value problems for partial differential equations in bounded regions are analyzed. A new approach to solving some boundary-value problems is proposed. The approach is based on the separation of functions into classes according to their supports and their further analysis. This approach represents a solution in a much more descriptive form and enables one to analyze the state of the inner regions of a deformed body and to naturally include objects such as "vibration stability viruses" into consideration of a lithospheric plate [1]. An advantage of this method is that solutions for both simply connected bounded regions and multiply connected unbounded regions are represented in a similar form [1, 2].

Spatial dynamic problems of continuum mechanics for anisotropic prestressed materials with inclusion of temperature, piezoelectric, and electromagnetic properties corresponding to the real media of the Earth's crust and ecological problems are among such problems. Investigations in this direction were begun in [3, 4] in response to the concept of the Earth's block structure, which was proposed by Academician Sadovskiĭ [5]. At present, when the real structure of the Earth's crust can be determined experimentally and mechanical characteristics in the earthquake preparation zone can be calculated, these investigations are of current interest.

Below, we will analyze three-dimensional problems for convex regions with smooth boundaries; the *n*-dimensional case is analyzed similarly.

1. In a bounded convex simply connected region Ω with boundary Γ whose curvatures are twice continuously differentiable, we consider the boundary-value problem for the following system of partial differential equations with constant coefficients:

$$\mathbf{Q}(\partial x_n, \partial x_k)\boldsymbol{\varphi} = 0, \quad \mathbf{x} \in \Omega(R^3),$$
$$\mathbf{R}(\partial x_k)\boldsymbol{\varphi} = \mathbf{f}, \quad \mathbf{x} \in \Gamma.$$

Here, the $\mathbf{Q}$ operator can be represented in the matrix form

$$\mathbf{Q}(\partial x_n, \partial x_k) = \|a_{mrnk}\partial x_n \partial x_k + b_{mrk}\partial x_k + c_{mr}\|. \quad (1)$$

Summation over repeated indices is implied, and the notation is the following:

$$\mathbf{R}(\partial x_k) = \|h_{mrk}\partial x_k + p_{mr}\|,$$
$$\partial x = \frac{\partial}{\partial x}, \quad h_{mrk} = h_{mrk}(\Gamma);$$

$$\boldsymbol{\varphi} = \{\varphi_r\}, \quad r = 1, 2, \ldots, M, \quad m = 1, 2, \ldots, M;$$
$$\mathbf{f} = \{f_r\}, \quad \varphi(\mathbf{x}) = \varphi(x_1, x_2, x_3); \quad (2)$$
$$\mathbf{Q}(\alpha) \equiv \mathbf{Q}(-i\alpha_n, -i\alpha_k), \quad n, k = 1, 2, 3;$$
$$Q = \det\mathbf{Q}(\alpha), \quad \det\|a_{mrnk}\alpha_n\alpha_k\| \neq 0, \quad |\boldsymbol{\alpha}| > 0.$$

We consider that the boundary operator $\mathbf{R}$ satisfies the Shapiro–Lopatinskiĭ conditions and the boundary-value problem is well posed.

This boundary-value problem generates a pseudodifferential operator whose elliptic symbol is the matrix function $\mathbf{Q}(\boldsymbol{\alpha})$. It is known [6, 7] that this pseudodifferential operator acts in the space of slowly increasing generalized functions $H_s(\Omega)$ and is limited from $H_s(\Omega)$ to $H_{s-2}(\Omega)$ for any s, where

$$\|\boldsymbol{\varphi}\|_s^2 = \sum\|\varphi_r\|_s^2, \quad \|\varphi_r\|_s^2 = \iint\int_{-\infty}^{\infty}|F\varphi_r|^2(1 + |\boldsymbol{\alpha}|)^{2s}d\boldsymbol{\alpha},$$
$$r = 1, 2, \ldots, M,$$
$$|\boldsymbol{\alpha}|^2 = \alpha_1^2 + \alpha_2^2 + \alpha_3^2, \quad d\boldsymbol{\alpha} = d\alpha_1 d\alpha_2 d\alpha_3, \quad (3)$$
$$d\mathbf{x} = dx_1 dx_2 dx_3,$$

$$F\varphi_r = \int_{-\infty}^{\infty}\iint\varphi_r(x)e^{i\langle\boldsymbol{\alpha}, x\rangle}dx,$$

$$\varphi_r = \frac{1}{(2\pi)^3}\int_{-\infty}^{\infty}\iint F\varphi_r(x)e^{-i\langle\boldsymbol{\alpha}, x\rangle}d\boldsymbol{\alpha},$$

$$\langle\boldsymbol{\alpha}, \mathbf{x}\rangle = \alpha_1 x_1 + \alpha_2 x_2 + \alpha_3 x_3.$$

Kuban State University, ul. Karla Libknekhta 149, Krasnodar, 350640 Russia
e-mail: babeshko@kubsu.ru

1028-3358/03/4803-0134$24.00

For $s > 0.5$, the reduction operator from Ω to Γ acts as a limited operator from $H_s(\Omega)$ to $H_{s+\frac{1}{2}}(\Gamma)$.

Considering that the generalized vector function is such that $\boldsymbol{\varphi} \in H_s(\Omega)$, we take the triple Fourier transform of system of differential equations (1). Taking the Fourier transform of derivatives and integrating by parts with inclusion of boundaries, we arrive at the relations

$$\begin{aligned} \mathbf{Q}(\alpha)F\boldsymbol{\varphi} &= \iint_{\Gamma} \mathbf{N}(\boldsymbol{\alpha}, \xi)e^{i\langle\boldsymbol{\alpha}\xi\rangle}d\Gamma, \\ \mathbf{N}(\boldsymbol{\alpha}, \boldsymbol{\xi}) &= \mathbf{T}(\boldsymbol{\xi}, \boldsymbol{\alpha})\mathbf{R}(\partial\boldsymbol{\xi})\boldsymbol{\varphi}(\boldsymbol{\xi}) \\ &\quad + \mathbf{G}(\boldsymbol{\xi}, \boldsymbol{\alpha})\mathbf{S}(\partial\boldsymbol{\xi})\boldsymbol{\varphi}(\boldsymbol{\xi}). \end{aligned} \tag{4}$$

Here, matrices $\mathbf{T}(\boldsymbol{\xi}, \boldsymbol{\alpha})$ and $\mathbf{G}(\boldsymbol{\xi}, \boldsymbol{\alpha})$ are known, result from integration, and include the relations between the normals to the surface and axes of the chosen coordinate system [3, 4], while $d\Gamma$ is the element of the oriented surface.

The right-hand side of Eq. (4) involves all $2M$ boundary operators that are admissible by the boundary-value problem and are referred to as natural. In particular, both the boundary operator corresponding to the Dirichlet problem and the Neumann boundary operator appear in the case of the boundary-value problem for the Laplace equation.

Thus, the right-hand side of Eq. (4) involves the set of natural boundary operators, the number of which, due to the appearance of the **S** operator, exceeds the number required for the correct formulation of the boundary-value problem. Solving the system of equations with respect to the $\boldsymbol{\varphi}(\mathbf{x})$ vector, we obtain the representation

$$\boldsymbol{\varphi}(\mathbf{x}) = \frac{1}{8\pi^3}\int_{-\infty}^{\infty}\int\int\mathbf{Q}^{-1}(\boldsymbol{\alpha})\iint_{\Gamma}\mathbf{N}(\boldsymbol{\alpha}, \boldsymbol{\xi})e^{-i\langle\boldsymbol{\alpha}(x-\xi)\rangle}d\Gamma d\boldsymbol{\alpha}. \tag{5}$$

We introduce the vector functions **f** that specify the boundary conditions to the right-hand side of Eq. (5). The **g** vector generated by M independent boundary conditions remains unknown:

$$\mathbf{S}\boldsymbol{\varphi}(\boldsymbol{\xi}) = \mathbf{g}(\boldsymbol{\xi}).$$

Therefore, to determine the $\boldsymbol{\varphi}$ vector function, i.e., to solve the boundary-value problem, it is necessary to find the **g** vector.

The relations necessary for its determination are obtained by factorization, i.e., by separating a class of functions that are equivalent due to the requirement that they have a common support in $\overline{\Omega}$.

Factorization automatically leads to the formulation of the boundary conditions of the given boundary-value problem. When the dimension exceeds one, it is necessary to analyze multidimensional manifolds.

2. Since Ω is a bounded region, it is a compact set. We introduce topology in it, i.e., the covering of the Euclidean space u_λ by open balls. An atlas is constructed by introducing local coordinate systems in each covering element so that the Jacobi determinants of transitions from one coordinate system to another have the same sign [8, 9]. In this case, at each point of the boundary Γ that lies in the overlapping with a ball, its covering Γ_λ and local coordinate system are generated. We take this coordinate system to be orthogonal; one axis is directed along the outer normal, and the other axes are directed along the geodesic lines. In this case, the surface Γ is oriented and is covered by open regions, and the Jacobian of the transition from the local coordinate system in one region to the coordinate system in another region is positive.

The manifold constructed above makes it possible to represent integral relation (5) by means of exterior calculus in terms of the exterior form [7–9]

$$\boldsymbol{\varphi}(\mathbf{x}) = \frac{1}{8\pi^3}\iiint_{\sigma}Q^{-1}(\boldsymbol{\alpha})\mathbf{D}(\boldsymbol{\alpha}) \times \iint_{\Gamma}\mathbf{N}(\boldsymbol{\alpha}, \boldsymbol{\xi})e^{-i\langle\boldsymbol{\alpha}(\mathbf{x}-\boldsymbol{\xi})\rangle}d\Gamma d\alpha_1\Lambda d\alpha_2\Lambda d\alpha_3, \tag{6}$$

$$\mathbf{Q}^{-1}(\boldsymbol{\alpha}) = Q^{-1}(\boldsymbol{\alpha})\mathbf{D}(\boldsymbol{\alpha}).$$

Here, $\mathbf{D}(\boldsymbol{\alpha})$ is the polynomial matrix of the cofactors of the elements of the $\mathbf{Q}(\boldsymbol{\alpha})$ matrix, the degree of the polynomials of matrix elements is no more than $2(M-1)$, σ is the compactified cycle with identified infinite points, and $\mathbf{Q}(\boldsymbol{\alpha})$ is the $2M$-degree polynomial of three complex variables α_k.

Taking into account the fact that the degree of the elements of the $\mathbf{N}(\boldsymbol{\alpha}, \boldsymbol{\xi})$ matrix is no more than unity, we conclude that the elements of the matrix

$$\mathbf{D}(\boldsymbol{\alpha})\mathbf{N}(\boldsymbol{\alpha}, \boldsymbol{\xi}) = \|\mathbf{P}_{mn}(\boldsymbol{\alpha}, \boldsymbol{\xi})\| = \mathbf{P}(\boldsymbol{\alpha}, \boldsymbol{\xi}) \tag{7}$$

are polynomials of the parameters α_k with degrees of no more than $2M-1$.

We require that the vector function $\varphi(\mathbf{x})$ vanish beyond $\overline{\Omega}$; i.e., we factorize it with respect to this support. As a result, it is necessary to analyze the following integrals of meromorphic exterior forms of the three complex variables, which are generated by the elements of the $\mathbf{P}(\alpha, \xi)$ matrix:

$$\boldsymbol{\varphi}(\mathbf{x}) = \frac{1}{8\pi^3} \times \iiint_{\sigma}\iint_{\Gamma}\frac{\mathbf{P}(\boldsymbol{\alpha}, \boldsymbol{\xi})}{Q(\boldsymbol{\alpha})}e^{-i\langle\boldsymbol{\alpha}(x-\xi)\rangle}d\Gamma d\alpha_1\Lambda d\alpha_2\Lambda d\alpha_3, \tag{8}$$

$$\mathbf{x} \notin \overline{\Omega}.$$

In terms of the theory of manifolds, the problem reduces to the analysis of the homology and cohomology groups of these meromorphic exterior forms.

For simplicity, we consider integral (8) under the assumption that the $Q(\boldsymbol{\alpha})$ polynomial has first-order zeros with a codimension of 1.

Since the boundary Γ is a compact set, we realize the unity decomposition by using the topology introduced above [9]. As a result, the surface Γ is covered by a finite set of nonoverlapping open regions Γ_β. We equip each region with orthogonal local coordinates $t_{k\beta}$, $k = 1, 2, 3$ with the $t_{3\beta}$ axis directed along the outer normal, which are mutually disjoint due to the convexity of the region.

Thus, each element Γ_β of covering is equipped with the local coordinate system $t_{k\beta}$ with the origin on this element. This coordinate system corresponds to the coordinates $x_{k\beta}$, $k = 1, 2, 3$ in the original Euclidean coordinate system. The $\overline{\Omega}$ region is in the lower half-space, $t_{3\beta} \le 0$, in the local coordinate systems constructed on the elements Γ_β.

Let the original coordinate system coincide with one of the local coordinate systems $t_{k\lambda}$. Ordering the sequence Γ_β and transforming from one local coordinate system to another, we generate the local coordinate systems α_β of three complex variables $\alpha_{k\lambda}$ by the condition

$$\langle \boldsymbol{\alpha}_\lambda, \mathbf{t}_\lambda \rangle = \langle \boldsymbol{\alpha}_{\lambda+1}, \mathbf{t}_{\lambda+1} \rangle.$$

In the constructed local coordinates, the condition $\mathbf{x} \notin \overline{\Omega}$ is equivalent to the condition $t_{3\beta} > 0$.

In this case, the Leray form residual can be calculated [9, 10]. To calculate it, we note that the $Q(\boldsymbol{\alpha})$ polynomial has $2M$ analytic branches, because the symbol is elliptic: its zeros are $\alpha_{3r}^+('\boldsymbol{\alpha})$ and $\alpha_{3r}^-('\boldsymbol{\alpha})$, such that $\operatorname{Im}\alpha_{3r}^+ \ge 0$ and $\operatorname{Im}\alpha_{3k}^- \le 0$ for $('\alpha) \longrightarrow \pm\infty$. The prime means the absence of $\alpha_{3\beta}$.

Let $t_{3\beta} > 0$. Decomposing the cycle into the basis cycles σ_r and calculating Leray form residuals, we arrive at the relations

$$\frac{1}{4\pi^2}\sum_{r=1}^{M}\int_{\delta_{r\beta}}\iiint_{\Gamma}\frac{\mathbf{P}(\alpha_{3r}^-, \xi)}{\partial\alpha_3 Q(\alpha_1, \alpha_2, \alpha_{3r}^-)}\{\exp i[\alpha_1(\xi_1 - x_1) + \alpha_2(\xi_2 - x_2) + \alpha_3^-(\xi_3 - x_3)]d\Gamma d\alpha_1 \Lambda d\alpha_2 \equiv 0, \mathbf{x} \notin \overline{\Omega}$$

with integration over two-dimensional cycles $\delta_{r\beta}$ that are not homological to zero and that belong to the analytic set of zeros of the locally holomorphic function $Q(\alpha_\beta)$ that lie in the region $\operatorname{Im}\alpha_{3r}^- \le 0$.

Since the terms of the sum are linearly independent, these relations lead to the identities

$$\iint_{\Gamma}\mathbf{P}[\alpha_{1r\beta}, \alpha_{2r\beta}, \alpha_{3r\beta}^-('\alpha_\beta), \xi]e^{\langle\alpha,\xi\rangle}d\Gamma \equiv 0, \qquad (9)$$
$$-\infty < \alpha_{1\beta}, \alpha_{2\beta} < \infty, \quad r = 1, 2, \ldots, M.$$

Thus, we obtain the set of locally analytic functions of two complex variables—integral equations of the boundary value problem.

Note 1. In the case of the convex regions $\overline{\Omega}$ under consideration, in addition to locally analytic functions (9), the following globally analytic functions can be constructed:

$$\iint_{\Gamma}\mathbf{P}(\boldsymbol{\alpha}, \boldsymbol{\xi})e^{\langle\boldsymbol{\alpha},\boldsymbol{\xi}\rangle}d\Gamma, \quad Q(\alpha) = 0.$$

The latter functions can be constructed both by the above factorization method and by using the properties of the Fourier transforms of finite functions in convex regions that have zero sets [11, p. 158].

The above representations, along with those obtained in [1, 2], were constructed in [12, 13] for a number of problems with anisotropy and electroelasticity. Suitable analysis of the possibilities of applying the methods of incorrect problems to these equations was performed in those studies.

To regularize the systems of integral equations, we represent, by using the unity decomposition, the integrals specified by Eq. (9) in the form

$$\iint_{\Gamma}\mathbf{P}_0[\alpha_{1r\beta}, \alpha_{2r\beta}, \alpha_{3r\beta}^-('\alpha_\beta), \boldsymbol{\xi}]e^{\langle\boldsymbol{\alpha},\boldsymbol{\xi}\rangle}d\Gamma$$

$$\equiv \sum_j\int_{\Gamma_j}e_j\mathbf{P}_0[\alpha_{1r\beta}, \alpha_{2r\beta}, \alpha_{3r\beta}^-('\alpha_\beta), \xi]e^{\langle\alpha,\xi\rangle}d\Gamma_j \equiv 0,$$

$$\sum_j e_j = 1, \quad r = 1, 2, \ldots, M.$$

Let us separate the element corresponding to the decomposition e_m and represent the local coordinate systems t_m, α_m associated with this element in the form

$$\iint_{\Gamma_m}[\mathbf{g}(\xi_{1m}, \xi_{2m}) + \mathbf{T}_0(\xi_{1m}, \xi_{2m}, \alpha_{1m}, \alpha_{2m}) \times \mathbf{f}(\xi_{1m}, \xi_{2m})]e_m\exp i(\alpha_{1m}\xi_{1m} + \alpha_{2m}\xi_{2m})d\xi_{1m}\xi_{2m}$$

$$+\sum_j{}'\iint_{\Gamma_j}[\mathbf{G}_0(\xi_{1j}, \xi_{2j}, \alpha_{1m}, \alpha_{2m})\mathbf{g}(\xi_{1j}, \xi_{2j}) + \mathbf{T}_0(\xi_{1j}, \xi_{2j}, \alpha_{1m}, \alpha_{2m})\mathbf{f}(\xi_{1j}, \xi_{2j})]e_j \times \exp\psi_j(\xi_{1j}, \xi_{2j}, \alpha_{1m}, \alpha_{2m})d\Gamma_j = 0, \qquad (10)$$
$$\operatorname{Re}\psi_j < 0, \quad \alpha_{1m}, \alpha_{2m} \to \pm\infty.$$

Here, nonlinear functions $\psi_j(\xi_{1j}, \xi_{2j}, \alpha_{1m}, \alpha_{2m})$ of α_{1m} and α_{2m} represent the transition from the local coordinates of one system to the local coordinates of another system.

The prime means the absence of the $j = m$ element in the sum, while the vector functions $\mathbf{g}(\xi_{1j}, \xi_{2j}) \equiv \mathbf{g}(\xi_{1j}, \xi_{2j}, 0)$ depend only on the first two coordinates of their local systems.

Vector functions $\mathbf{g}(\xi_{1j}, \xi_{2j})$ on the supports of the decomposition e_j are treated as elements of the $\mathbf{H}_{s+\frac{1}{2}}(\Gamma)$ space that is the direct sum of the $\mathbf{H}_{js+\frac{1}{2}}$ spaces with the norm

$$\|\mathbf{g}\|_{\mathbf{H}} = \max\|\mathbf{g}_j\|_{\mathbf{H}_j}, \qquad \mathbf{H} \equiv \mathbf{H}_{s+\frac{1}{2}}(\Gamma_j),$$

$$\mathbf{H}_j \equiv \mathbf{H}_{js+\frac{1}{2}}(\Gamma_j), \quad \mathbf{g} = (\mathbf{g}_1, \mathbf{g}_2, \ldots\},$$

where $\mathbf{g}_j \in \mathbf{H}_{js+\frac{1}{2}}(\Gamma_j)$ if the support belongs to Γ_j.

Applying the Fourier transform in the local coordinate systems (ξ_{1m}, ξ_{2m}), $(\alpha_{1m}, \alpha_{2m})$ to Eqs. (10), we arrive at the relations whose operator representation has the form

$$\mathbf{g} + \mathbf{Ag} = \mathbf{Bf}. \tag{11}$$

Taking into account the properties of matrix functions $\mathbf{G}_0$ entering into Eq. (10), one can prove that, first, the **A** operator is completely continuous in the above spaces and, second, the system of equations is a Fredholm system for **Bf** belonging to this space.

Note 2. Fredholm system (10) was constructed for convex regions $\overline{\Omega}$. However, it can be also constructed for nonconvex regions that admit partition into convex components, i.e., that have block structure. In this case, Fredholm systems are constructed individually for each block with inclusion of matching in the regions of block contacts.

Note 3. To regularize the system of integral equations and construct approximate solutions, decomposition elements can be represented as plane elements due to the smoothness of Γ. The error of approximation is estimated in terms of the derivatives of curvatures of Γ. When the boundary Γ is not smooth, angular points including prismlike points exist, and boundary conditions change in some lines (mixed conditions), it is necessary to additionally regularize the operators entering into **A** for system (11). If their contribution is small, they can be omitted in approximate calculations.

ACKNOWLEDGMENTS

This work was supported by the Ministry of Education of the Russian Federation; the Russian Foundation for Basic Research, R2003YuG (project nos. 03-01-96005, 03-01-96002, 03-01-96012, and 03-01-96007); and the Program “Integratsiya” (project no B0121).

REFERENCES

1. V. A. Babeshko, V. V. Buzhan, and R. Vil’yams, Dokl. Akad. Nauk **385**, 332 (2002) [Dokl. Phys. **47**, 156 (2002)].
2. O. M. Babeshko, O. V. Evdokimova, and S. M. Evdokimov, Dokl. Akad. Nauk **371**, 32 (2000).
3. V. A. Babeshko, Dokl. Akad. Nauk SSSR **284**, 73 (1985).
4. V. A. Babeshko, Dokl. Akad. Nauk SSSR **304**, 318 (1989).
5. M. A. Sadovskiĭ, L. G. Bolkhovitinov, and V. F. Pisarenko, *Deformation of Geophysical Space and Seismic Process* (Nauka, Moscow, 1987).
6. G. I. Éskin, *Boundary Value Problems for Elliptical Pseudodifferential Equations* (Nauka, Moscow, 1973).
7. L. R. Volevich and B. P. Paneyakh, Usp. Mat. Nauk **20** (1), 3 (1965).
8. V. S. Vladimirov, *Methods of the Theory of Functions of Many Complex Variables* (Nauka, Moscow, 1964; MIT Press, Cambridge, Mass., 1966).
9. B. V. Shabat, *Introduction into Complex Analyses* (Nauka, Moscow, 1985), Part 2.
10. L. A. Aĭzenberg and A. P. Yuzhakov, *Integral Presentations and Residues in Many-Dimensional Complex Analyses* (Nauka, Novosibirsk, 1979).
11. V. A. Babeshko, *Complex Method of Factorization in Space Dynamic Mixed Problems of Theory of Elasticity* (Nauka, Moscow, 1984).
12. A. O. Vatul’yan, Dokl. Akad. Nauk **333**, 312 (1993) [Phys. Dokl. **38**, 459 (1993)].
13. A. O. Vatul’yan and A. N. Solov’ev, Prikl. Mat. Mekh. **63** (6), 1035 (1999).

Translated by R. Tyapaev

Doklady Physics, Vol. 48, No. 3, 2003, pp. 138–141. Translated from Doklady Akademii Nauk, Vol. 389, No. 2, 2003, pp. 189–192.

MECHANICS

Global Optimality and Uniqueness in the Problem of Minimizing Loss of Total Pressure

V. N. Malozemov* and A. V. Omel'chenko

Presented by Academician N.F. Morozov September 26, 2002

Received October 14, 2002

The problem of the deceleration of a supersonic flow to subsonic velocities with the minimum loss of total pressure arose in the 1940s in connection with the problem of designing efficient supersonic air intakes [1, 2]. This problem was developed by G.I. Petrov in Russia and by K. Oswatitsch in Germany. They established the appropriateness of decelerating a flow in a system of several oblique shocks and a closing normal shock. It was found that the loss of total pressure in such a system was always lower than that in a single normal shock. In this case, the intensities of a given number of shocks can be chosen so that the loss of total pressure is minimal. Petrov also investigated the behavior of the total pressure in a system consisting of *n* oblique shocks and a closing sonic shock. This system turned out to provide better recovery of total pressure [1].

Petrov numerically determined the oblique-shock intensities in optimal systems and found that these intensities must be approximately equal to each other. Oswatitsch solved the problem of the optimal recovery of total pressure analytically and showed that the oblique-shock intensities must be equal to each other at the point of a possible extremum. However, he did not obtain a solution in an explicit form. Such a solution was presented in study [3] published in 1995. In [4], it was established that the conditions of a strict local minimum are met at the point of a possible extremum. However, the problem of the global optimality and uniqueness of the obtained solution remained an open question.

In this paper, we consider the problem of constructing a shock-wave system that is optimal for the total pressure and consists of several oblique shocks as a discrete optimal-control problem. Using the dynamic-programming method, we find the globally optimal and unique solution to this problem. We investigate the behavior of the optimal system as the number of shocks increases infinitely.

St. Petersburg State University,
Universitetskaya nab. 7/9, St. Petersburg, 199164 Russia
** e-mail: malv@gamma.math.spbu.ru*

1. We consider the plane steady supersonic flow of a perfect inviscid gas with shocks in tandem. For example, as was shown in [3], for a fixed Mach number M_0 in the incident flow and a specific heat ratio $\gamma \in (1, 2]$, the ratio of the total pressure beyond the system to the total pressure in the undisturbed flow can be expressed in terms of the intensities $J_k = \dfrac{p_k}{p_{k-1}}$ of shocks as

$$I_n^{(p_0)} = \prod_{k=1}^{n}\left\{J_k\left[\frac{J_k+\varepsilon}{J_k(1+\varepsilon J_k)}\right]^{\lambda}\right\},$$
$$\lambda = \frac{1+\varepsilon}{2\varepsilon}, \quad \varepsilon = \frac{\gamma-1}{\gamma+1}. \tag{1}$$

Instead of the Mach number, it is more convenient to use the gas-dynamic function $\mu = 1 + \varepsilon(M^2 - 1)$. The ratio of the values of this function behind the shock and in front of it is related to the intensity J_k of the *k*th shock by the relationship [3]

$$\frac{\mu_k}{\mu_{k-1}} = \varphi(J_k), \quad \varphi(t) = \frac{t+\varepsilon}{t(1+\varepsilon t)}. \tag{2}$$

The nondecreasing entropy condition imposes the restriction $J_k \geq 1$ on the *k*th-shock intensity. In addition, for the existence of the $(k+1)$th shock with $k = 1, 2, \ldots, n-1$, the flow behind the *k*th shock must remain supersonic ($\mu_k \geq 1$). This condition is satisfied when $J_k \leq A(\mu_{k-1})$, where

$$A(t) = \frac{t-1}{2\varepsilon} + \sqrt{\frac{(t-1)^2}{4\varepsilon^2} + t}.$$

Behind the last shock, the flow becomes subsonic if the intensity J_n satisfies the inequalities

$$A(\mu_{n-1}) \leq J_n \leq B(\mu_{n-1}), \quad B(t) = \frac{(1+\varepsilon)t-1}{\varepsilon}.$$

Thus, in the general case,

$$J_k \in U_k(\mu_{k-1}), \quad k = 1, 2, \ldots, n. \tag{3}$$

1028-3358/03/4803-0138$24.00 © 2003 MAIK "Nauka/Interperiodica"

As a shock-wave system optimal for the total pressure, we have in mind a system providing the maximum value of goal function (1) under restrictions (2) and (3):

$$\begin{gathered} I_n^{(p_0)} := \prod_{k=1}^{n} \{J_k[\varphi(J_k)]^\lambda\} \to \sup, \\ \mu_k = \mu_{k-1}\varphi(J_k), \quad 1 \le J_k \le A(\mu_{k-1}), \\ k = 1, 2, \ldots, n-1; \\ A(\mu_{n-1}) \le J_n \le B(\mu_{n-1}). \end{gathered} \tag{4}$$

The problem of constructing the optimal shock-wave system is seen to be a discrete optimal-control problem [5]. In this problem, the intensities J_k of the shocks involved in the system are the control parameters, and the quantities μ_k are the phase variables specifying the system state. The shocks in tandem convert the supersonic flow from an initial state with $\mu_0 \ge 1$ to a final state with $\mu_n \le 1$. In this case, the hyperbolic type of equations describing such flows determines the evolutionary nature of this transition, converting the extremum problem under investigation into a discrete optimal-control problem.

The principal result of this study is formulated as follows.

Theorem 1. *For all* $\mu_0 \ge 1$ *and* $n \ge 2$, *the unique solution to problem* (4) *is determined as follows*:

$$J_1^* = J_2^* = \ldots = J_n^* =: J^*, \quad J^* = A(\mu_0^{1/n}).$$

We propose the schematic proof of Theorem 1.

2. The function $\varphi(t)$ with the derivative

$$\varphi'(t) = -\frac{\varepsilon(1 + 2\varepsilon t + t^2)}{[t(1+\varepsilon t)]^2}$$

decreases strictly from $+\infty$ to 0 on the $(0, +\infty)$ semiaxis with $\varphi(1) = 1$ and $\varphi'(1) = -\lambda^{-1}$. The equation $\varphi(t) = \mu^{-1}$ for $\mu > 0$ has a unique solution $t = A(\mu)$. Substituting this solution into the equation, we obtain the equality

$$\varphi(A(\mu)) = \mu^{-1}, \quad \mu > 0. \tag{5}$$

From the relationships $\mu_k = \mu_{k-1}\varphi(J_k)$, $1 \le J_k \le A(\mu_{k-1})$, it follows that $\mu_{k-1} \ge \mu_k \ge 1$ so that $\mu_0 \ge \mu_1 \ge \ldots \ge \mu_{n-1} \ge 1$.

The function $h(t) = t[\varphi(t)]^\lambda$ with the derivative

$$h'(t) = -\frac{(1-\varepsilon)(t-1)^2}{2(t+\varepsilon)(1+\varepsilon t)}[\varphi(t)]^\lambda$$

also decreases strictly from $+\infty$ to 0 on $(0, +\infty)$. In application to problem (4), this means that, in particular, the best value for J_n is $J_n = A(\mu_{n-1})$. According to Eq. (5), $\mu_{n-1}\varphi(J_n) = 1$ and $\mu_0 \prod_{k=1}^{n} \varphi(J_k) = 1$ for such J_n. The goal function for problem (4) takes the form $\mu_0^{-\lambda} A(\mu_{n-1}) \prod_{k=1}^{n-1} J_k$. Discarding the positive factor $\mu_0^{-\lambda}$, we arrive at the extremal problem

$$\begin{gathered} A(\mu_{n-1}) \prod_{k=1}^{n-1} J_k \to \sup, \\ \mu_k = \mu_{k-1}\varphi(J_k), \quad 1 \le J_k \le A(\mu_{k-1}), \\ k = 1, 2, \ldots, n-1. \end{gathered} \tag{6}$$

The feature of restrictions for problem (6) implies that $J_{k+1} = \ldots = J_{n-1} = A(\mu_{n-1}) = 1$ if $J_k = A(\mu_{k-1})$ for certain $k \in \{1, 2, \ldots, n-2\}$.

3. We write problem (6) for $n = 2$:

$$Q_2(J_1) := A(\mu_1)J_1 \to \sup_{J_1 \in [1, A(\mu_0)]}, \quad \mu_1 = \mu_0\varphi(J_1). \tag{7}$$

Let us differentiate the goal function:

$$Q_2'(J_1) = A + J_1 A'(\mu_1)\mu_1'(J_1). \tag{8}$$

According to Eq. (5),

$$\mu_1 = \frac{A(1 + \varepsilon A)}{A + \varepsilon}. \tag{9}$$

After differentiating this identity, we obtain

$$A'(\mu_1) = \frac{(A+\varepsilon)^2}{\varepsilon(1 + 2\varepsilon A + A^2)}. \tag{10}$$

Further, according to the definition of μ_1 and Eq. (9),

$$\begin{aligned} \mu_1'(J_1) &= \mu_1 \frac{\varphi'(J_1)}{\varphi(J_1)} \\ &= -\varepsilon \frac{A(1+\varepsilon A)}{A+\varepsilon} \frac{1 + 2\varepsilon J_1 + J_1^2}{J_1(J_1+\varepsilon)(1+\varepsilon J_1)}. \end{aligned} \tag{11}$$

Substituting Eqs. (10) and (11) into Eq. (8), we obtain the formula

$$\begin{aligned} Q_2'(J_1) &= A \frac{1 + 2\varepsilon J_1 + J_1^2}{(J_1+\varepsilon)(1+\varepsilon J_1)} \\ &\times \left[\frac{(J_1+\varepsilon)(1+\varepsilon J_1)}{1 + 2\varepsilon J_1 + J_1^2} - \frac{(A+\varepsilon)(1+\varepsilon A)}{1 + 2\varepsilon A + A^2}\right]. \end{aligned} \tag{12}$$

Let us designate

$$\chi(t) = \frac{(t+\varepsilon)(1+\varepsilon t)}{1 + 2\varepsilon t + t^2}.$$

In this case, Eq. (12) can be rewritten as

$$Q_2'(J_1) = \frac{A}{\chi(J_1)}[\chi(J_1) - \chi(A(\mu_1))].$$

The function $\chi(t)$ with the derivative

$$\chi'(t) = \frac{(1-\varepsilon^2)(1-t^2)}{(1+2\varepsilon t+t^2)^2},$$

which is negative for $t > 1$, decreases strictly on the semiaxis $[1, +\infty)$. As J_1 varies from 1 to $A(\mu_0)$, the quantity μ_1 varies from μ_0 to 1, and the quantity $A(\mu_1)$, from $A(\mu_0)$ to $A(1) = 1$. Therefore, the difference $\chi(J_1) - \chi(A(\mu_1))$ vanishes at the only point J_1^* in the interval $[1, A(\mu_0)]$, is positive for $J_1 < J_1^*$, and is negative for $J_1 > J_1^*$. Therefore, J_1^* is the unique solution to problem (7).

To determine J_1^*, it is necessary to solve the equation $A(\mu_1) = J_1$. This can be done by means of the equivalent transitions

$$A(\mu_1) = J_1 \Leftrightarrow \mu_1^{-1} = \varphi(J_1) \Leftrightarrow \varphi(J_1) = \mu_0^{-1/2} \Leftrightarrow J_1 = A(\mu_0^{1/2}).$$

Thus, $J_1^* = A(\mu_0^{1/2})$.

4. Let us execute the induction transition from $n-1$ to n, $n \geq 3$. In problem (6), we fix $J_1 \in [1, A(\mu_0)]$ and $\mu_1 = \mu_0\varphi(J_1)$. In the remaining $(n-1)$-shock system, the optimal parameters are $J_2^* = \ldots = J_{n-1}^* =: J^*$, $J^* = A(\mu_1^{1/(n-1)})$ according to the induction assumption. Problem (6) takes the form

$$Q_n(J_1) := J_1[J^*(\mu_1)]^{n-1} \to \sup_{J_1 \in [1, A(\mu_0)]}. \quad (13)$$

Let us differentiate the goal function:

$$Q_n'(J_1) = (J^*)^{n-1} + (n-1)J_1(J^*)^{n-2}\frac{dJ^*}{d\mu_1}\frac{d\mu_1}{dJ_1}. \quad (14)$$

Since $\varphi(J^*) = \mu_1^{-1/(n-1)}$, we have $\mu_1 = [\varphi(J^*)]^{-n+1}$. After differentiating the last identity, we obtain

$$\frac{dJ^*}{d\mu_1} = -\frac{[\varphi(J^*)]^n}{(n-1)\varphi'(J^*)}. \quad (15)$$

At the same time,

$$\frac{d\mu_1}{dJ_1} = -\varepsilon[\varphi(J^*)]^{-n+1}[J_1\chi(J_1)]^{-1}. \quad (16)$$

Substituting Eqs. (15) and (16) into Eq. (14), we arrive at the formula

$$Q_n'(J_1) = \frac{(J^*)^{n-1}}{\chi(J_1)}[\chi(J_1) - \chi(J^*(\mu_1))].$$

Now, similar to the case $n = 2$, we show that the function $Q_n(J_1)$ has the only maximum point J_1^* in the $[1, A(\mu_0)]$ interval, which is the unique root of the equation $J^*(\mu_1) = J_1$ in this interval. We write the sequence of equivalent transitions:

$$J^*(\mu_1) = J_1 \Leftrightarrow \varphi(J_1) = \mu_1^{-1/(n-1)} \Leftrightarrow \varphi(J_1) = \mu_0^{-1/n} \Leftrightarrow J_1 = A(\mu_0^{1/n}).$$

We find that $J_1^* = A(\mu_0^{1/n})$.

5. It is evident that $J^* \longrightarrow 1$ for $n \longrightarrow \infty$. A more exact result is valid.

Lemma. *For $\mu_0 > 1$, the limiting relationship*

$$\lim_{n\to\infty} n(J^* - 1) = \lambda \ln \mu_0 \quad (17)$$

is valid.

To prove this lemma, we rewrite the equality $\varphi(J^*) = \mu_0^{-1/n}$ in the form

$$\mu_0^{-1} = \left\{[1 + (\varphi(J^*) - 1)]^{(\varphi(J^*)-1)^{-1}}\right\}^{[(\varphi(J^*)-\varphi(1))/(J^*-1)](J^*-1)n}. \quad (18)$$

Let us take the logarithm of Eq. (18) and pass to the limit for $n \longrightarrow \infty$. Taking into account the fact that $\varphi'(1) = -\lambda^{-1}$, we obtain Eq. (17).

Theorem 2. *For $\mu_0 > 1$, the relation*

$$\lim_{n\to\infty} (J^*)^n = \mu_0^{\lambda} \quad (19)$$

is valid.

The proof follows from the lemma and the equality

$$(J^*)^n = \left\{(1 + (J^* - 1))^{(J^*-1)^{-1}}\right\}^{(J^*-1)n}.$$

From the physical viewpoint, formula (19) means that the ratio of the static pressure behind the last shock in the optimal system to the pressure in the undisturbed flow tends to the finite value μ_0^{λ}, which is the intensity of a simple compression wave decelerating the flow down

to sonic velocity. Such a system is the best one for minimizing the loss of total pressure. Thus, relationship (19) shows that a qualitative transition occurs in the optimal system as the number of shocks increases infinitely: a system of n oblique shocks becomes an optimal isentropic wave.

ACKNOWLEDGMENTS

This work was supported by the Russian Foundation for Basic Research, project nos. 00-15-96106 and 01-01-00231.

REFERENCES

1. G. I. Petrov, *Selected Works. Aeromechanics of High Speeds and Space Research* (Nauka, Moscow, 1992).
2. R. Germann, *Supersonic Incoming Diffusers* (Fizmatgiz, Moscow, 1960).
3. A. V. Omel'chenko and V. N. Uskov, Izv. Akad. Nauk, Mekh. Zhidk. Gaza, No. 6, 118 (1995).
4. V. N. Malozemov, A. V. Omel'chenko, and V. N. Uskov, Prikl. Mat. Mekh. **62** (6), 1015 (1998).
5. V. G. Boltyanskiĭ, *Optimal Control of Discrete Systems* (Nauka, Moscow, 1973).

Translated by V. Bukhanov

Doklady Physics, Vol. 48, No. 3, 2003, pp. 142–145. Translated from Doklady Akademii Nauk, Vol. 389, No. 2, 2003, pp. 193–196.

MECHANICS

Vibrations of an Elastic Half-Space with a Set of Rigid Inclusions

O. D. Pryakhina, A. V. Smirnova, A. A. Evdokimov, and M. S. Kapustin

Presented by Academician V.A. Babeshko September 27, 2002

Received October 11, 2002

We consider vibrations of a half-space containing an elastic medium. This medium is characterized by density ρ, longitudinal-wave velocity c_1, and transverse-wave velocity c_2. Let a vertical harmonic axisymmetric load $p(r)\exp(-i\omega t)$ be applied to a circular domain ($r \le a$, $z = 0$) of the half-space boundary (r is the circle radius, ω is the vibration frequency, and t is time). We assume that vertically oriented deep inclusions with a length h are distributed over a circle with a radius r_0 at the boundary. In the general case, the inclusions experience both vertical and horizontal vibrations.

Displacements of material points of the medium are described by the Lamé equations [1] (the common factor $\exp(-i\omega t)$ entering into all the characteristics is omitted everywhere)

$$\begin{aligned}
&(\lambda + 2\mu)\left[\frac{\partial^2 U_r}{\partial r^2} + \frac{1}{r}\frac{\partial U_r}{\partial r} - \frac{1}{r^2}U_r\right] \\
&+ (\lambda + \mu)\frac{\partial}{\partial r}\left[\frac{\partial U_z}{\partial z}\right] + \mu\frac{\partial^2 U_r}{\partial z^2} + \rho\omega^2 U_r = X_r, \\
&(\lambda + 2\mu)\frac{\partial^2 U_z}{\partial z^2} + \mu\left[\frac{\partial^2 U_z}{\partial r^2} + \frac{1}{r}\frac{\partial U_z}{\partial r}\right] \\
&+ (\lambda + \mu)\frac{\partial}{\partial z}\left[\frac{\partial U_r}{\partial r} + \frac{1}{r}U_r\right] + \rho\omega^2 U_z = X_z.
\end{aligned} \tag{1}$$

Here, $U_r(r, z)$ and $U_z(r, z)$ are the amplitudes of vertical and horizontal displacements, respectively, and λ and μ are parameters of the medium.

The load (inclusions) distributed over the depth is taken as a localized bulk force with the components $X_r = f_r(z)\delta(r - r_0)$ and $X_z = f_z(z)\delta(r - r_0)$.

Kuban State University, ul. Karla Libknekhta 149, Krasnodar, 350640 Russia

The boundary conditions of the problem have the form

$$\begin{aligned}
z = 0\colon\ &(\lambda + 2\mu)\frac{\partial U_z}{\partial z} + \lambda\left[\frac{\partial U_r}{\partial r} + \frac{1}{r}U_r\right] = \begin{cases} p(r), & r \le a \\ 0, & r > a, \end{cases} \\
&\mu\left[\frac{\partial U_z}{\partial r} + \frac{\partial U_r}{\partial z}\right] = 0;
\end{aligned} \tag{2}$$

$$U_r(r, z),\ U_z(r, z) \to 0, \text{ as } z \to -\infty. \tag{3}$$

Using the integral-transformation method [2], we reduce boundary-value problem (1)–(3) for the system of partial differential equations to the corresponding boundary-value problem for a system of ordinary differential equations, which can be written out in the matrix form

$$\begin{aligned}
&\frac{d\mathbf{Y}}{dz} = \mathbf{A}\mathbf{Y} + \mathbf{F}, \\
&\mathbf{T}\mathbf{Y}|_{z=0} = \mathbf{P}, \quad \mathbf{Y} \to 0; \quad z \to -\infty.
\end{aligned} \tag{4}$$

Here, we use the following notation:

$$\mathbf{Y} = \{u_r,\ u_r',\ u_z,\ u_z'\},$$

$$\mathbf{F} = \left\{0,\ \frac{1}{\rho c_2^2}\eta_r,\ 0,\ \frac{1}{\rho c_1^2}\eta_z\right\},$$

$$\mathbf{A} = \begin{pmatrix} 0 & 1 & 0 & 0 \\ a_{21} & 0 & 0 & a_{24} \\ 0 & 0 & 0 & 1 \\ 0 & a_{42} & a_{43} & 0 \end{pmatrix},$$

$$\mathbf{T} = \begin{pmatrix} \alpha(1 - 2c^2) & 0 & 0 & 1 \\ 0 & \rho c_2^2 & -\alpha\rho c_2^2 & 0 \end{pmatrix},$$

1028-3358/03/4803-0142$24.00

$$\mathbf{P} = \left\{\frac{1}{\rho c_1^2}p(\alpha), 0\right\},$$

$$\eta_r(\alpha, z) = f_r(z)r_0J_1(\alpha r_0),$$
$$\eta_z(\alpha, z) = f_z(z)r_0J_0(\alpha r_0),$$

$$p(\alpha) = \int_0^\infty p(r)rJ_0(\alpha r)dr, \quad a_{21} = c^{-2}\sigma_1^2,$$

$$a_{24} = \alpha(c^{-2}-1), \quad a_{42} = \alpha(c^2-1),$$

$$a_{43} = c^2\sigma_2^2, \quad \sigma_k = \sqrt{\alpha^2 - \aleph_k^2}, \quad k = 1, 2,$$

$$\aleph_k = \frac{\omega}{c_k}, \quad k = 1, 2, \quad c = \frac{c_2}{c_1}.$$

The components of the vector $\mathbf{Y}$ are the Bessel transforms of the displacement amplitudes U_r and U_z and their derivatives, with α being the Bessel transform argument.

We seek a solution to Eqs. (4) as the superposition $\mathbf{Y}(\alpha, z) = \mathbf{Y}_{\text{gen}} + \mathbf{Y}_{\text{part}}$, where $\mathbf{Y}_{\text{gen}}(\alpha, z) = \sum_{k=1}^{4} d_k e^{\gamma_k z}\mathbf{m}_k$ is a general solution to the homogeneous system of equations with $\mathbf{F} = 0$ and $\overline{\mathbf{Y}}_{\text{part}}(\alpha, z) = \sum_{k=1}^{4} t_k(z)e^{\gamma_k z}\mathbf{m}_k$ is a particular solution to the inhomogeneous system.

The quantities γ_k are eigenvalues of the matrix $\mathbf{A}$, with $\gamma_{1,2} = \pm\sigma_1$, $\gamma_{3,4} = \pm\sigma_2$, and $\mathbf{m}_k$ are the corresponding eigenvectors. The variable coefficients $t_k(z)$ are determined by the method of variation of constants:

$$t_s(z) = \frac{r_0}{2\rho\omega^2}\left(\pm\frac{\alpha J_1(\alpha r_0)}{\sigma_1}I_{r1}^{\mp} + J_0(\alpha r_0)I_{z1}^{\mp}\right),$$

$$t_{s+2}(z) = \frac{r_0}{2\rho\omega^2}\left(J_1(\alpha r_0)I_{r2}^{\mp} \pm \frac{\alpha J_0(\alpha r_0)}{\sigma_2}I_{z2}^{\mp}\right),$$

$$s = 1, 2,$$

$$I_{rn}^{\mp} = \int_0^z f_r(\zeta)e^{\mp\sigma_n\zeta}d\zeta, \quad I_{zn}^{\mp} = \int_0^z f_z(\zeta)e^{\mp\sigma_n\zeta}d\zeta.$$

Here, J_0 and J_1 are the zero-order and first-order Bessel functions, respectively. The unknown coefficients d_k are found from boundary conditions (4).

Taking the components $u_r(\alpha, z)$ and $u_z(\alpha, z)$ of the vector $\mathbf{Y}$ and performing the inverse Bessel transformation, we arrive at the integral representation of the solution to problem (1)–(3):

$$U_r(r, z) = \int_0^\infty (D_1(\alpha)P(\alpha, z) + D_2(\alpha)M(\alpha, z) + K_1(\alpha, z))\alpha J_1(\alpha r)d\alpha,$$
$$U_z(r, z) = \int_0^\infty (D_1(\alpha)R(\alpha, z) - D_2(\alpha)S(\alpha, z) + K_2(\alpha, z))\alpha J_0(\alpha r)d\alpha. \quad (5)$$

Here,

$$D_1 = \frac{p(\alpha)}{\rho c_1^2} - 2c^2(Ht_2(-h) + \alpha\sigma_2 t_4(-h)),$$

$$P = \frac{\alpha}{\Delta}(He^{\sigma_1 z} - \sigma_1\sigma_2 e^{\sigma_2 z}),$$

$$D_2 = 2\rho c_2^2(\alpha\sigma_1 t_2(-h) + Ht_4(-h)),$$

$$R = -\frac{\sigma_1}{\Delta}(He^{\sigma_1 z} - \alpha^2 e^{\sigma_2 z}),$$

$$M = \frac{\sigma_2(\alpha^2 e^{\sigma_1 z} - He^{\sigma_2 z})}{\rho c_1^2\Delta},$$

$$S = \frac{\alpha(-\sigma_1\sigma_2 e^{\sigma_1 z} + He^{\sigma_2 z})}{\rho c_1^2\Delta},$$

$$K_1 = \alpha t_1(z)e^{\sigma_1 z} + \alpha N_2 e^{-\sigma_1 z} - \sigma_2 t_3(z)e^{\sigma_2 z} + \sigma_2 N_4 e^{-\sigma_2 z},$$

$$K_2 = -\sigma_1 t_1(z)e^{\sigma_1 z} + \sigma_1 N_2 e^{-\sigma_1 z} + \alpha t_3(z)e^{\sigma_2 z} + \alpha N_4 e^{-\sigma_2 z},$$

$$N_k = t_k(z) - t_k(-h), \quad k = 2, 4,$$

$$\Delta(\alpha) = 2c^2(\alpha^2\sigma_1\sigma_2 - H^2), \quad H = \alpha^2 - 0.5\aleph_2^2.$$

In order to analyze the amplitude–frequency characteristic of the vertical component $U_z(r, 0)$ depending on parameters of the vibration sources that excite the Rayleigh wave, we consider only the displacement-vector component $U_z(r, z)$ entering into general solution (5):

$$U_z(r, 0) = \int_{\Gamma_1} (D_1(\alpha)R(\alpha, 0) + D_2(\alpha)S(\alpha, 0) + K_2(\alpha, 0))H_0^1(\alpha r)\alpha d\alpha. \quad (6)$$

We choose the integration contour Γ_1 in accordance with the principle of ultimate absorption [2] and calculate integral (6) by the theory of residues, after singularities of the integrand have been found and the domain of its decrease has been determined.

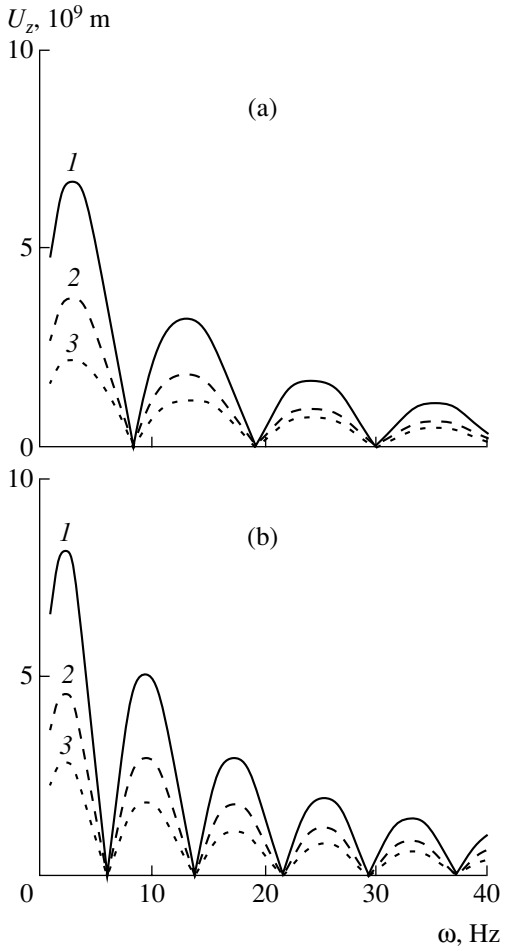

Fig. 1. Amplitude–frequency characteristics of the vertical component for the Rayleigh wave at $p(r) = 0$, $f_z(\zeta) = k\zeta + b$, and $h = 10$ m: (a) $r_0 = 5$ and (b) 7 m; ε = (*1*) 0, (*2*) 0.5, and (*3*) 1.

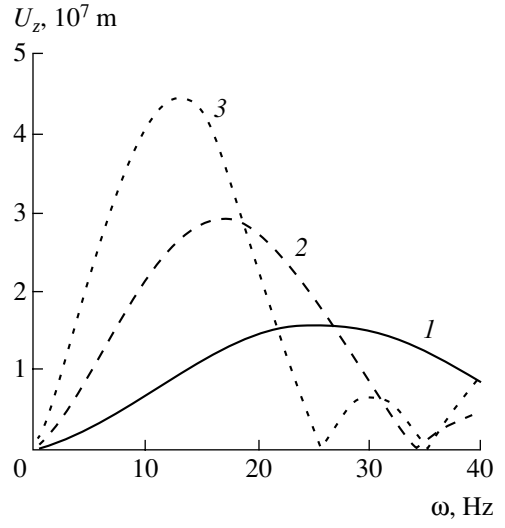

Fig. 2. The same as in Fig. 1 for $p(r) = 100$ N m^{-2} and $f_z(\zeta) = 0$: a = (*1*) 2, (*2*) 3, and (*3*) 4 m.

The analysis shows that the singularities of the integrand are Tsimple poles and branch points $\alpha = \aleph_1$ and $\aleph_2$. The wave number ζ of the Rayleigh wave is a solution to the dispersion equation $\Delta(\alpha) = 0$ [3]. As a result, we arrive at the expression

$$U_z(r, 0) = \frac{\pi i}{\Delta'(\zeta)}[0.5\aleph_2^2\sigma_1(Q_1(\zeta) - 2Q_2(\zeta))\zeta H_0^1(\zeta r)].$$

Here,

$$Q_1(\zeta) = \frac{p(\zeta)}{\rho c_1^2},$$

$$Q_2(\zeta) = 2c^2(H(\zeta)t_2(-h) + \zeta\sigma_2 t_4(-h)),$$

$$\Delta'(\zeta) = 2c^2(2\zeta\sigma_1\sigma_2 + \zeta^3(\sigma_1\sigma_2)^{-1}(\sigma_1^2 + \sigma_2^2) - 4H),$$

and ζ is the Rayleigh pole.

The amplitude of vertical displacements for $z = 0$ was evaluated numerically in the T far-field zone of the source for a medium characterized by parameters typical of the ground ($\rho = 1.4 \times 10^3$ kg m^{-3}, $c_1 = 0.2 \times 10^3$ m s^{-1}, and $c_2 = 0.12 \times 10^3$ m s^{-1}). In Fig. 1, we present the amplitude–frequency characteristics for the vertical component of the Rayleigh wave excited by the anchor columns of a surface-vibration source [$p(r) = 0$ N m^{-2}], with the stress function linear over the source length: $f_z(\zeta) = k\zeta + b$. In this case, $k = \frac{b(\varepsilon - 1)}{h}$ and $b = \frac{2}{h(\varepsilon + 1)}$. Curves *1*, *2*, and *3* correspond to $\varepsilon = 0$, 0.5, and 1, respectively. The columns have the length $h = 10$ m, and the radius of their distribution on the circle is either $r_0 = 5$ or 7 m.

Our calculations indicate that the amplitude of the surface wave excited by the columns increases with their distribution radius (see Fig. 1). In addition, an increase in the number of radiating elements complicates the wave interference pattern and leads to an increase in the number of T blocking frequencies and to variations in their values. The presence of the interference pattern and blocking frequencies is in complete agreement with the general theory [4]. According to this theory, the vibrational energy of surface waves excited by anchor columns of a vibration source is converted into the energy of bulk waves excited by the same elements. As was mentioned above, the stresses distributed over a generatrix of a column may vary with the depth. When performing the numerical calculations, we analyzed the effect of this circumstance on the surface-wave amplitude. As is seen from Fig. 1, the uniformly distributed load ($\varepsilon = 1$) excites vibrations with smaller amplitudes, regardless of values of both frequency and column length.

The function $U_z(r, 0)$ is shown in Fig. 2 for the Rayleigh wave excited by the surface load $p(r) = 100$ N m^{-2} distributed over the circles with the radii $a = 2$, 3, and

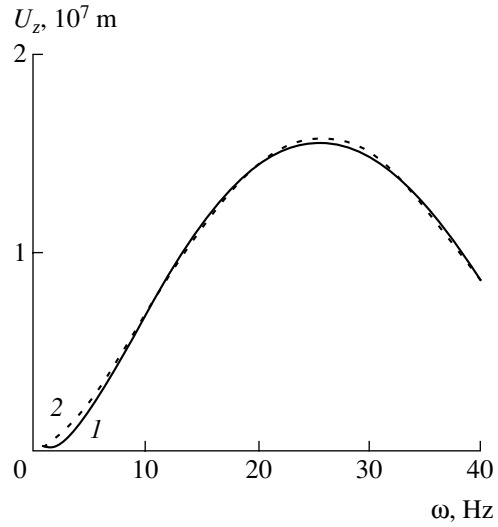

Fig. 3. The same as in Fig. 1 for $p(r) = 100$ N m^{-2}, $a = 2$ m, $\varepsilon = 0$, $h = 10$ m: (*1*) $f_z(\zeta) = k\zeta + b$ and $r_0 = 5$; (*2*) $f_z(\zeta) = 0$.

4 m (curves *1*, *2*, and *3*, respectively). The results presented correspond to a vibrator that has no anchor columns [$f_z(\zeta) = 0$]. An increase in the area of the applied load results in a growth of the vibration amplitudes and changes the interference pattern. As in the previous case, there appear blocking frequencies in the system for which the total energy of mechanical vibrations of the radiating plate is converted into the vibrational energy of the half-space inner points.

It is noteworthy that, at low and intermediate frequencies, the amplitude of an excited surface wave is significant regardless of the vibrator properties. This amplitude decreases sharply with increasing frequency (see Figs. 1 and 2). Moreover, the results presented in these figures indicate that the basic radiated element (plate) of the vibrator excites surface wave whose amplitude–frequency characteristic is greater by a factor of 100 than the amplitude of the displacements due to vibrations of the columns. Figure 3 shows the amplitude–frequency characteristics of the Rayleigh waves excited (*1*) by all the radiating elements of the vibrator and (*2*) by only the basic one.

The results obtained suggest that the effect of anchor columns on the wave field is basically noticeable at low frequencies. Hence, this fact should be taken into account when anchor columns are used for the purpose of increasing loads applied to a radiating plate.

ACKNOWLEDGMENTS

The work was supported in part by the US Civilian Research and Development Foundation (CRDF), project no. REC-004, and by the Russian Foundation for Basic Research, project no. 02-01-00831.

REFERENCES

1. W. Nowacki, *Elasticity Theory* (PWN, Warszawa, 1970; Mir, Moscow, 1975).
2. I. I. Vorovich and V. A. Babeshko, *Dynamic Mixed Problems of the Elasticity Theory for Nonclassical Regions* (Nauka, Moscow, 1979).
3. Yu. A. Amenzade, *Theory of Elasticity* (Vysshaya Shkola, Moscow, 1976).
4. V. A. Babeshko, B. V. Glushkov, and Zh. F. Vinchenko, *Dynamics of Inhomogeneous Linearly Elastic Media* (Nauka, Moscow, 1989).

Translated by V. Chechin

Doklady Physics, Vol. 48, No. 3, 2003, pp. 146–150. Translated from Doklady Akademii Nauk, Vol. 389, No. 2, 2003, pp. 197–202.

MECHANICS

Launching and Impact of a Group of High-Velocity Bodies

I. E. Khorev[1], V. K. Yakushev[1], S. A. Zelepugin[2,*], V. N. Sidorov[2], and Academician V. E. Fortov[3]

Received October 3, 2002

The mathematical simulation of physical interaction between targets and a group of variously sized particles imitating a stream of technogenic fragments in near space is a promising method of gaining reliable data about the dynamics of the total process of a group impact and its consequences [1]. The comprehensive experimental and theoretical analysis of this complicated problem must involve the following components: the development of methods and devices for the launching of a group of particles under laboratory conditions in air and in vacuum, the experimental investigation of an impact of particles with targets and its consequences for protected samples, and numerical simulation with development of an adequate closed procedure for calculation of the impact of a group of fragments with targets imitating the protection of space equipment and directly with the space-apparatus construction.

Among a large variety of possible systems of controlled launching of a fragment stream under laboratory conditions, assemblies using the aerodynamic principle of the step-by-step separation of a launched construction are of considerable interest, because they require no additional power supplies to provide a given orientation of fragments in the group. In this case, it is necessary to organize the process of separation of various trays and leading facilities in a possibly short time interval [2].

1. In this study, we use the launching of a group of particles (from 2 to 12) in air on the basis of the separation of compound systems which were composed of identical bodies sequentially so that their longitudinal axes coincided or were parallel to each other and to the longitudinal axis of the whole system [3]. In this case, we provided the process of the directed ejection of fragments from a container under the action of aerodynamic forces.

The basic experiments were carried out on a ballistic path with gunpowder and light-gas launchers of various calibers. As model technogenic fragments, we took balls and $L/D = 1$ cylinders from engineering materials. In a number of sections on the ballistic path, the flow around for separating assemblies was made visible by the "luminous-point" method [2]. The range of initial velocities of motion for an assembly in air varied within the range 500–3500 m/s. Parametric investigations showed that the motion and the scattering of the compound system as a whole can be purposefully controlled by choosing the corresponding values of aerodynamic and mass–geometric characteristics of constituent bodies of an assembly [4].

To launch a particle group, we fabricated a container that ensured the safety of the fragment-group composition in moving along the barrel channel and their controlled scattering at a given point of a trajectory. The container was cylinder-shaped. Its head section was a flat end, a truncated cone, or a needle. The motion of a group of fragments with the parameters controlled over the front (perpendicularly to the direction of motion) and over the depth (along the trajectory of motion) was provided by two methods of the directed ejection of particles from the container under the action of aerodynamic forces. The first method was ejection through the lateral surface at a certain angle to the direction of motion of the container. Ejection of particles through the lateral surface of the container was investigated for a cylinder with an axial channel that was made through the front-end side and that branched into a number of radial channels. The channels were connected with the cavities in which ejecting fragments were placed. Arranging the axial and radial channels with given diameters, one can obtain various positions of the model particles over front and depth. Figure 1 shows a shadow photograph of the motion of the container and a group of two spherical steel fragments each 7.5 mm in diameter. The velocity of bodies corresponds to the Mach number M = 3.1. It is seen in the photograph that the centers of mass of the particles are at the same depth, yielding a simultaneous impact with the target, the so-called "frontal impact." In the second case, indentations arranged in a given sequence were made at

[1] *Tomsk State University, pr. Lenina 36, Tomsk, 634050 Russia*

[2] *Department of Structural Macrokinetics, Tomsk Research Center, Siberian Division, Russian Academy of Sciences, pr. Akademicheskiĭ 10/3, Tomsk, 634021 Russia*

[3] *Institute for High Temperatures, Russian Academy of Sciences, ul. Izhorskaya 13/19, Moscow, 127412 Russia*

* *e-mail: szel@tbism.tomsk.ru*

1028-3358/03/4803-0146$24.00 © 2003 MAIK "Nauka/Interperiodica"

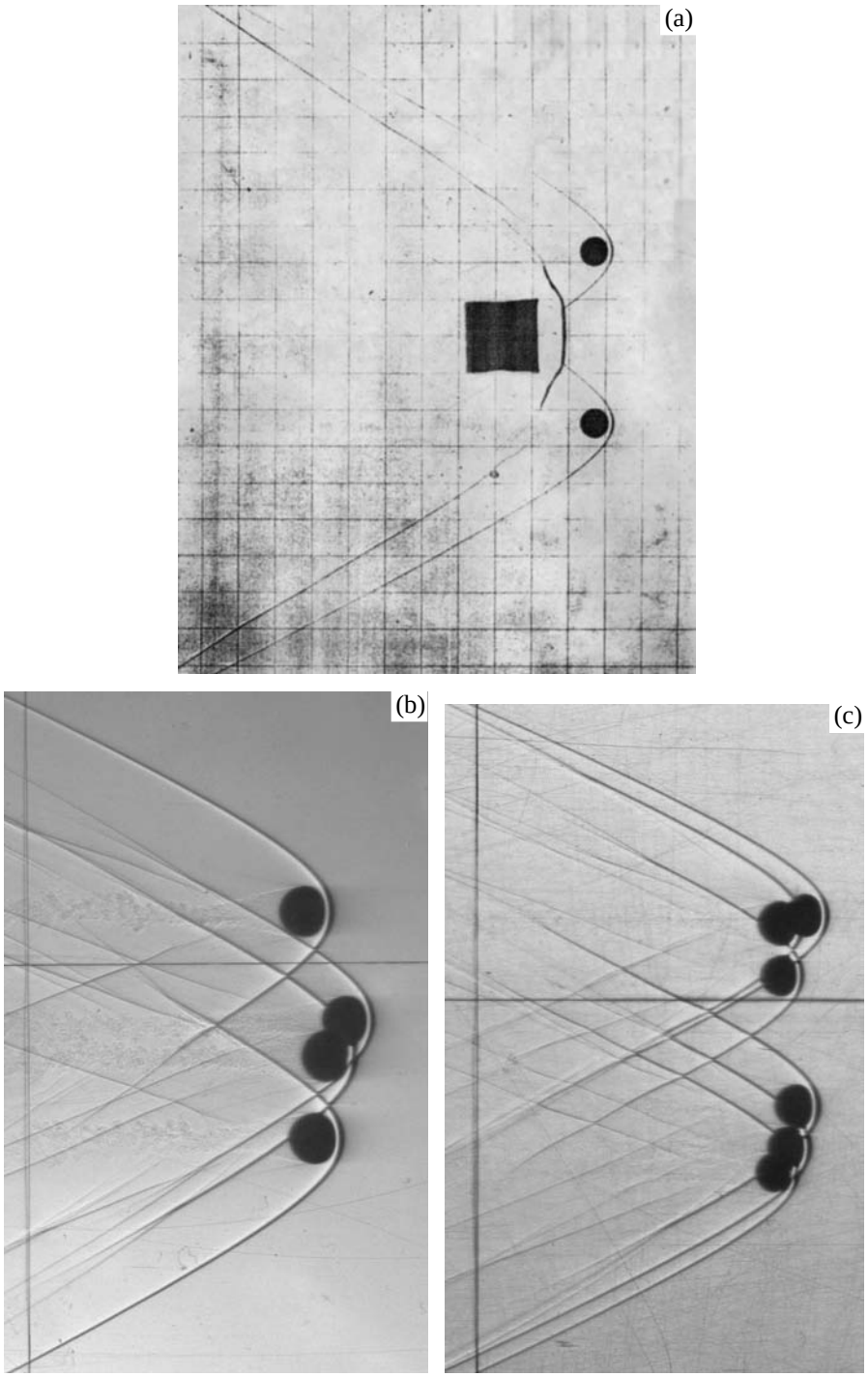

Fig. 1. Shadow photographs of the motion of a container and groups of (a) two, (b) four, and (c) six spherical particles.

the plane front surface, and the ejected model fragments were placed into these cavities. Their number varied from two to six. When the assembly moved in air, the container was decelerated. In this case, the group of particles was separated from the container and moved along a given trajectory, forming the stream configuration corresponding to its primary composition. Figure 1 also shows shadow photographs for the motion of four and six spherical bodies, respectively, at the Mach number M = 3.3. The spatial positions of the particles corresponded to their primary arrangement in the container, where four particles were disposed in the vertices of a regular quadrangle and six particles were arranged as two identical triples at the container ends, i.e., formed a "dumb-bell." Thus, the developed procedures and facilities are well suited for the laboratory

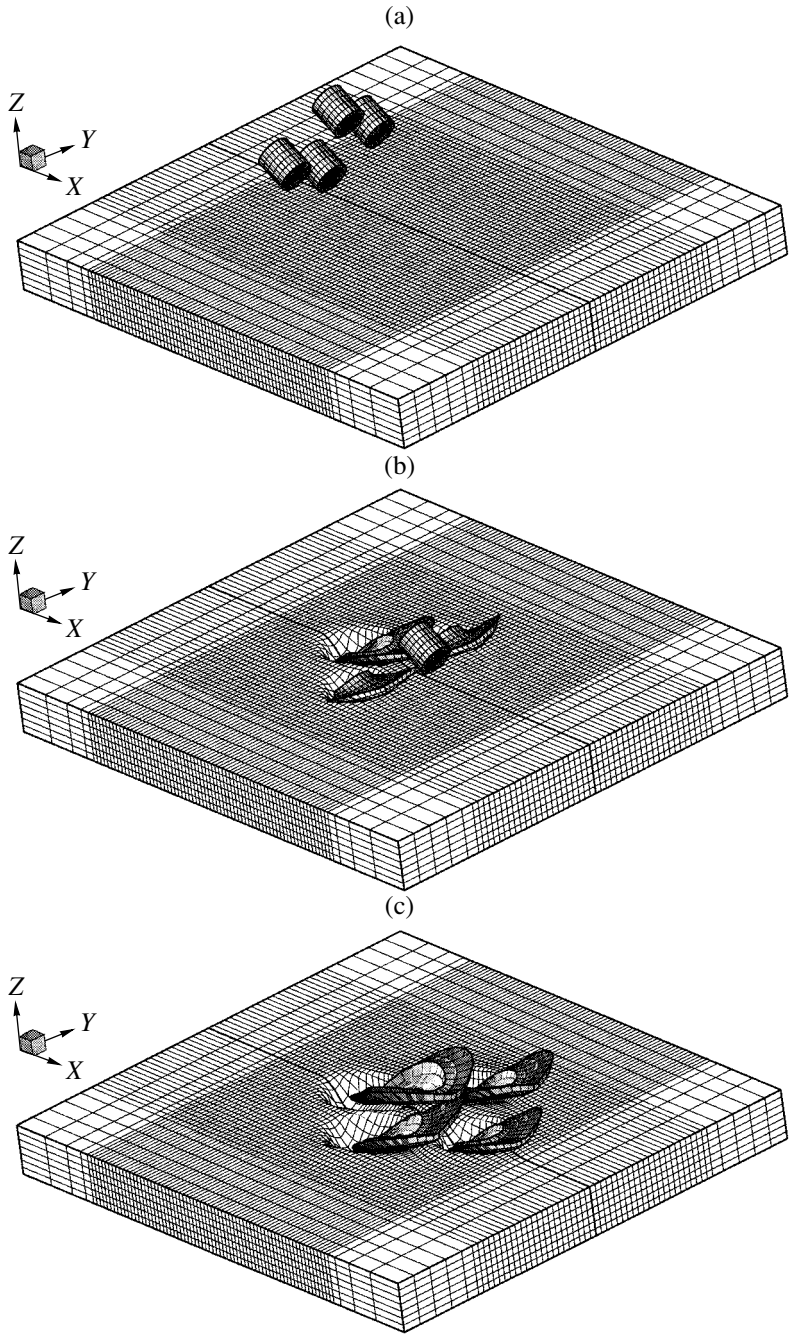

Fig. 2. Computer chronograms of the frontal interaction of the group of four $L/D = 1$ bodies with a plate at an angle of 60° with an initial impact velocity of 2873 m/s.

simulation of the launching and the following action of a fragment debris (with a given distribution of particles in the flow over front and depth) on objects of space equipment.

2. In the three-dimensional formulation, we numerically simulated the processes of the interaction of a group of high-velocity bodies with a target of finite thickness during normal and oblique impacts. The aim of this simulation was to develop a closed procedure for calculating the impact of a fragment stream on constructions that is adequate to the available experimental data, i.e., a method of estimating the ballistic limit of a construction, the area and volume of failure, the presence of spall fragments in the space behind the target inducing the shrapnel effect, etc.

Numerical calculations were focused on investigating the time evolution of processes of high-velocity deformation and failure of bodies and on estimating

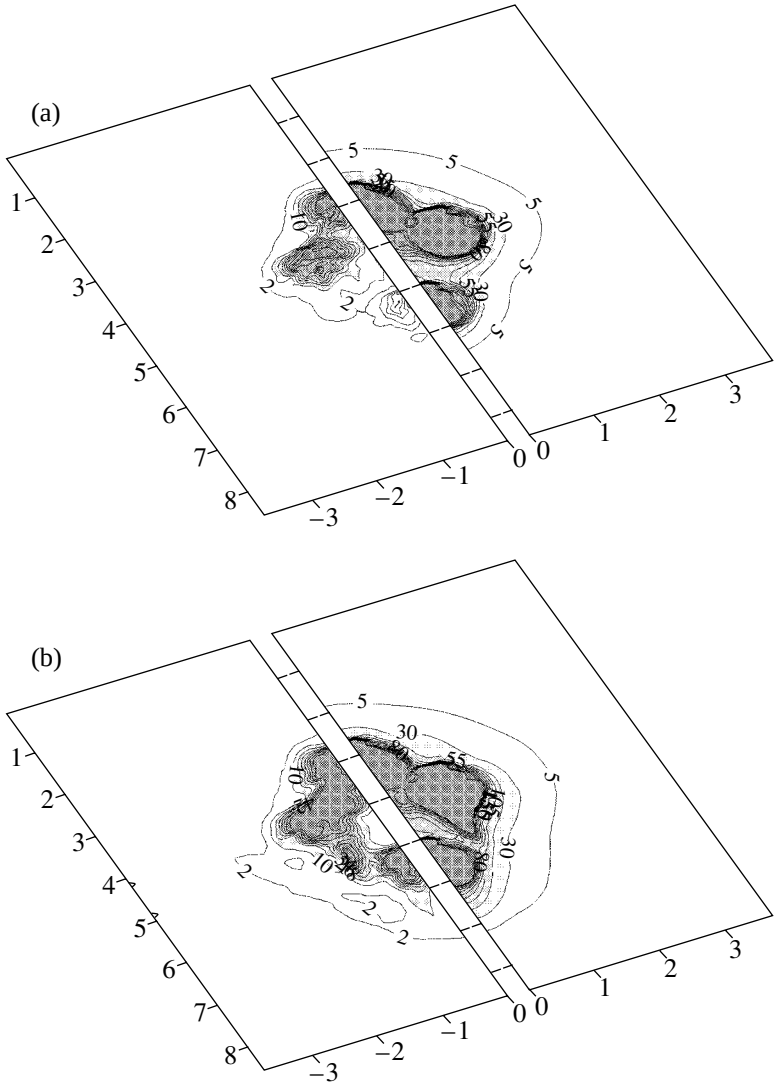

Fig. 3. Contours of the specific volume of microdamages (left-hand sides, with an interval of 8 cm^3/kg) and of the specific energy of shear deformations (right-hand sides, 25 kJ/kg) along the front surface of the plate at the time instants of (a) 7 and (b) 17 μs.

their mutual effect during group impact. In the numerical calculations, we used a model of a damaged medium with microcavities (pores and cracks). The set of equations describing the unsteady adiabatic motions of a compressible medium with allowance for the nucleation and accumulation of microdamages and temperature effects for the case of three spatial variables involved the equations continuity, motion, and energy balance [5]. The failure of a material under high-velocity impact was numerically simulated in a kinetic model of active type [6]. This model determines the growth of microdamages, which continuously modify the properties of the material, inducing the relaxation of stresses. The strength characteristics of the medium (the shear modulus and dynamic yield strength) depended on temperature and on the damage level [7]. In this case, an athermal character of high-velocity deformation was simulated up to temperatures comparable with the melting point of the material [8]. As the criterion of the erosion failure of the material, which occurs in the region of intense interaction and deformation of contacting bodies, we took the critical value of the specific energy of shear deformations [1, 9].

We considered the problem of the impact of four identical $L/D = 1$ cylindrical projectiles, each 6 mm in diameter and in height, with an 8-mm-thick target. The projectiles were arranged in the same plane, which can deviate at a certain angle from the front surface of the target. Initially, the centers of the first and fourth projectiles was separated by 22.3 mm, and the other two were arranged symmetrically between them at a distance of 11.4 mm from the first impacting body and 15 mm from the fourth one. The initial velocities of all projectiles were equal to 2873 m/s in magnitude and directed along their symmetry axes and along the normal to the flight plane (oblique impact). The interacting

bodies were made of a steel whose constants can be found in [5]. Slide conditions were realized at contact surfaces. The problem was numerically solved by a modified finite-element method [10, 11].

Figure 2 shows the chronograms of the process of interaction between the group of four projectiles and a target of finite thickness. In this case, the angle between the particle-front plane and the front surface of the target was equal to 60°. Figure 2a corresponds to the time when the group of elements approaches the target, and Figs. 2b and 2c correspond to times of 7 and 14 μs, respectively, after the onset of interaction between the target and the first impacting body. Figure 2b illustrates the time when two intermediate projectiles just begin to interact with the target, the last, extreme right, impacting body does not yet reach the target, and the first impacting body penetrates the target and experiences significant plastic deformation simulated by including the concept of erosion failure. By 14 μs (Fig. 2c), the impacting body that first began to interact has already rebounded, losing contact with the target. The next two projectiles have also rebounded almost completely by this time, and the last, fourth, impacting body continues to interact with the target.

The description of an impact of a group of particles at a different time, when the initial stage of contact between the target and last particle coincides with the final stages of the interaction of the first particle, requires numerical simulation of the late stages of the high-velocity-interaction process, which are accompanied by significant deformations and failures. In this study, we used the critical value of the specific volume of microdamages and the critical value of the specific energy of shear deformations as the criteria of total failure [9]. The behavior of the failed material was not simulated in further numerical calculations. The use of the criteria for the total failure of the material made it possible to calculate the penetration and the rebound of the entire group of model fragments for arbitrary impact angles and various distances between particles over front and depth.

The calculations show that, under certain conditions of interaction, the processes influence each other, and a united zone of deformation and failure with extrema corresponding to every impacting body is formed in the target. Figure 3 shows the contours for a specific volume of microdamages and for a specific energy of shear deformations for an impact angle of 30° (in each case, half sections of the target surface are shown, because there is a symmetry plane passing through the axes of the first and fourth projectiles) and illustrates the confluence of the zones of microdamages and deformation that are induced by the action of the first and intermediate projectiles. The zone induced by the action of the last impacting body is somewhat distant from the united region due to the large initial distance between the projectiles and the later onset of the impact. Furthermore, in Fig. 3 (t = 17 μs), we can observe the formation of an additional center of microdamages between the last and intermediate projectiles. This center is induced by the mutual influence of bodies and is responsible for the nonuniform "elliptic" structure of plate damage. The three-dimensional calculations of this complicated problem are qualitatively corroborated by the corresponding experiments.

ACKNOWLEDGMENTS

This work was supported by the Russian Foundation for Basic Research, project nos. 00-01-00550 and 00-01-00766.

REFERENCES

1. I. E. Khorev, S. A. Zelepugin, A. A. Konyaev, *et al.*, Dokl. Akad. Nauk **369**, 481 (1999) [Dokl. Phys. **44**, 818 (1999)].
2. *Ballistic Setups and Their Application in Experimental Researches*, Ed. by N. A. Zlatin and G. I. Mishin (Nauka, Moscow, 1974).
3. K. S. Kolesnikov, V. I. Kozlov, and V. V. Kokushkin, *Dynamics of Separation of Stages of Aircrafts* (Mashinostroenie, Moscow, 1977).
4. V. K. Yakushev, V. I. Bimatov, and R. G. Nikolaev, Byull. Izobret. No. 3, Inventor's Certificate No. 2145067 (2000).
5. V. A. Gorel'skiĭ, S. A. Zelepugin, and V. N. Sidorov, Izv. Akad. Nauk, Mekh. Tverd. Tela, No. 3, 45 (1999).
6. G. I. Kanel, S. V. Razorenov, A. V. Utkin, and V. E. Fortov, *Shock Wave Phenomena in Condensed Matter* (Yanus-K, Moscow, 1996).
7. S. A. Zelepugin and V. B. Nikulichev, Fiz. Goreniya Vzryva **36** (6), 186 (2000) [Combust., Explos., Shock Waves **36** (6), 845 (2000)].
8. G. I. Kanel, S. V. Razorenov, A. V. Utkin, and V. E. Fortov, Izv. Akad. Nauk, Mekh. Tverd. Tela, No. 5, 173 (1999).
9. S. A. Zelepugin, Vychisl. Tekhnol. **6** (2), 163 (2001).
10. G. R. Johnson, J. Appl. Mech. **44** (1), 95 (1977).
11. V. A. Gorel'skiĭ, S. A. Zelepugin, and A. Yu. Smolin, Zh. Vychisl. Mat. Mat. Fiz. **37** (6), 742 (1997) [Comput. Math. Math. Phys. **37** (6), 722 (1997)].

Translated by V. Bukhanov

Doklady Physics, Vol. 48, No. 3, 2003, pp. 151–155. Translated from Doklady Akademii Nauk, Vol. 389, No. 3, 2003, pp. 332–337.

MECHANICS

Partial-Equilibrium Positions of Nonlinear Dynamic Systems: Their Stability and Stability with Respect to Some of Variables

V. I. Vorotnikov

Presented by Academician V.V. Rumyantsev November 25, 2002

Received November 25, 2002

For the partial-equilibrium positions of nonlinear nonautonomous systems of general ordinary differential equations, the problem of stability is considered, and the problem of stability and asymptotic stability with respect to some of variables is formulated. Solutions to these problems are obtained in the context of the Lyapunov direct method. In this case,

(i) for the nonuniform stability of partial-equilibrium positions, we introduce a requirement on the Lyapunov function, which is weaker than the known requirement of the infinitely small upper limit with respect to some of variables for the uniform stability of this type;

(ii) the requirements on the Lyapunov function in problems of stability and asymptotic stability of partial-equilibrium positions with respect to some of variables are significantly weakened due to variation of the region where this function is constructed: the function is generally not sign definite with respect to some of variables in the classical sense, and the derivative of this function can be sign changing.

1. STABILITY OF PARTIAL-EQUILIBRIUM POSITIONS

In the framework of partial-stability theory [1–14], the problem of the stability of sets that are the partial-equilibrium positions of dynamic systems is studied [5, 9, 11–13]. Recently, interest in the problem of partial stability has increased considerably. Moreover, the more general problem of input-to-output stability was considered [15], which before covered only the analysis of input–output operator relations for describing systems.

Nizhni Tagil Technological Institute,
Ural State Technical University,
Nizhni Tagil, 622031 Russia
e-mail: vorot@ntiustu.ru

For a precise formulation of the problem, let us consider the nonlinear nonautonomous system of ordinary differential equations

$$\dot{\mathbf{y}} = \mathbf{Y}(t, \mathbf{y}, \mathbf{z}), \quad \dot{\mathbf{z}} = \mathbf{Z}(t, \mathbf{y}, \mathbf{z}) \tag{1}$$

and, as usual in the theory of partial stability (**y** stability) [1–13], assume that system (1) is continuous in the region

$$t \geq 0, \quad \|\mathbf{y}\| \leq h, \quad \|\mathbf{z}\| < \infty, \tag{2}$$

and that its solution is unique and **z**-extendable. Let the condition

$$\mathbf{Y}(t, \mathbf{0}, \mathbf{z}) \equiv \mathbf{0} \tag{3}$$

be valid. In the case of the uniqueness of the solution of system (1), this condition means that the $\mathbf{y} = \mathbf{0}$ position is an *invariant set* of this system and its partial-equilibrium position.

Let $\mathbf{x} = (\mathbf{y}^t, \mathbf{z}^t,)^t$ ("t" means transposition) and $\mathbf{x}(t; t_0, \mathbf{x}_0)$ be a solution of system (1) with the initial condition $\mathbf{x}_0 = \mathbf{x}(t_0; t_0, \mathbf{x}_0)$.

Definition 1 [5, 9, 12]. The partial-equilibrium position $\mathbf{y} = \mathbf{0}$ of the system of Eqs. (1) and (3) is

(i) *stable* if, for any $\varepsilon > 0$ and $t_0 \geq 0$, there is $\delta(\varepsilon, t_0) > 0$ such that $\|\mathbf{y}(t; t_0, \mathbf{x}_0)\| < \varepsilon$ for all $t \geq t_0$, when $\|\mathbf{y}_0\| < \delta$ and $\|\mathbf{z}_0\| < \infty$;

(ii) *uniformly stable* if δ is independent of t_0.

When

$$\mathbf{Y}(t, \mathbf{0}, \mathbf{0}) \equiv \mathbf{0}, \quad \mathbf{Z}(t, \mathbf{0}, \mathbf{0}) \equiv \mathbf{0} \tag{4}$$

system (1) has the total-equilibrium position $\mathbf{x} = \mathbf{0}$.

Definition 2 [5, 12, 13]. The equilibrium position $\mathbf{x} = \mathbf{0}$ of the system of Eqs. (1) and (4) is

(i) **y**-*stable for all* $\mathbf{z}_0$ if, for any $\varepsilon > 0$ and $t_0 \geq 0$, there is $\delta(\varepsilon, t_0) > 0$ such that $\|\mathbf{y}(t; t_0, \mathbf{x}_0)\| < \varepsilon$ for all $t \geq t_0$, when $\|\mathbf{y}_0\| < \delta$ and $\|\mathbf{z}_0\| < \infty$;

(ii) *uniformly* **y** *-stable for all* $\mathbf{z}_0$ if $\delta = \delta(\varepsilon)$.

In what follows, the problems of stability (*nonuniform*) of the total and partial-equilibrium positions of system (1) will be treated in the sense of the first parts

1028-3358/03/4803-0151$24.00

of Definitions 1 and 2, and the common conditions of their solvability will be compared with the conditions of *uniform* stability that were previously obtained for the same problems in [5, 9] (second parts of Definitions 1 and 2) and with the results reported in [13].

We consider (i) continuous functions $a(r)$ and $b(r)$ that increase monotonically for $r \in [0, h]$ and satisfy the condition $a(0) = b(0) = 0$, (ii) function $V(t, \mathbf{x})$, which is continuously differentiable in region (2) and satisfies the condition $V(t, \mathbf{0}) \equiv 0$ and its derivative $\dot{V}$ in view of system (1), and (iii) function $V^*(t, \mathbf{y})$, which is continuous in region (2) and satisfies the condition $V^*(t, \mathbf{0}) \equiv 0$.

Theorem 1. *Let there exist functions V and V* that satisfy the conditions*

$$a(\|\mathbf{y}\|) \le V(t, \mathbf{y}, \mathbf{z}) \le V^*(t, \mathbf{y}), \tag{5}$$

$$\dot{V}(t, \mathbf{y}, \mathbf{z}) \le 0 \tag{6}$$

for system (1) *in region* (2). *Then,* (i) *condition* (3) *is satisfied for system* (1) *and the partial-equilibrium position* $\mathbf{y} = \mathbf{0}$ *is stable*; (ii) *in case* (4), *the equilibrium position* $\mathbf{x} = \mathbf{0}$ *of system* (1) *is* $\mathbf{y}$*-stable for all* $\mathbf{z}_0$.

Proof is divided into two steps.

1. We demonstrate that, when conditions (5) and (6) are satisfied, condition (3) is also satisfied. To that end, we consider the solution $\mathbf{x}(t; t_0, \mathbf{0}, \mathbf{z}_0)$ of system (1) for arbitrary $t_0 \ge 0$ and $\mathbf{z}_0$. In view of Eq. (5), we have $V(t_0, \mathbf{0}, \mathbf{z}_0) \equiv 0$. Taking into account the equality

$$V(t, \mathbf{x}(t; t_0, \mathbf{x}_0)) = V(t_0, \mathbf{x}_0) + \int_{t_0}^{t} \dot{V}(\tau, \mathbf{x}(\tau; t_0, \mathbf{x}_0))\, d\tau \tag{7}$$

and inequalities $V \ge 0$ and (6), we arrive at the identity

$$V(t, \mathbf{x}(t; t_0, \mathbf{0}, \mathbf{z}_0)) \equiv 0, \tag{8}$$

which, in view of Eq. (5), leads to the identity

$$\mathbf{y}(t; t_0, \mathbf{0}, \mathbf{z}_0) \equiv \mathbf{0}. \tag{9}$$

Let us prove that identities (3) and (9) are equivalent. In view of Eq. (9) and the arbitrariness of $t_0 \ge 0$ and $\mathbf{z}_0$, the substitution of the solution $\mathbf{x}(t; t_0, \mathbf{0}, \mathbf{z}_0)$ into system (1) provides identity (3). Conversely, if identity (3) is valid, system (1) has the stability position $\mathbf{y} = \mathbf{0}$. Taking into account the assumption that the solution of system (1) is unique, we arrive at identity (9).

2. We demonstrate that, when conditions (5) and (6) are satisfied, the partial-equilibrium position $\mathbf{y} = \mathbf{0}$ of system (1) is $\mathbf{y}$-stable. Since the functions V and V^* are continuous and conditions $V(t, \mathbf{0}) \equiv V^*(t, \mathbf{0}) \equiv 0$ are valid for any $\varepsilon > 0$ and $t_0 \ge 0$, there is a $\delta(\varepsilon, t_0) > 0$ such that $V(t_0, \mathbf{x}_0) \le V^*(t_0, \mathbf{y}_0) < a(\varepsilon)$ when $\|\mathbf{y}_0\| < \delta$ and $\|\mathbf{z}_0\| < \infty$.

Taking Eqs. (6) and (7) into account, we have

$$a(\|\mathbf{y}(t; t_0, \mathbf{x}_0)\|) \le V(t, \mathbf{x}(t; t_0\mathbf{x}_0)) \le V(t_0, \mathbf{x}_0) \le V^*(t_0, \mathbf{y}_0) < a(\varepsilon) \tag{10}$$

for all $t \ge t_0$. In view of the properties of the function $a(r)$ and inequalities (10), we conclude that $\|\mathbf{y}(t; t_0, \mathbf{x}_0)\| < \varepsilon$ for all $t \ge t_0$ and any $\varepsilon > 0$ and $t_0 \ge 0$, when $\|\mathbf{y}_0\| < \delta$ and $\|\mathbf{z}_0\| < \infty$. Q.E.D.

Discussion of theorem 1. (i) If Eq. (5) is replaced by the more stringent conditions [5, 9]

$$a(\|\mathbf{y}\|) \le V(t, \mathbf{y}, \mathbf{z}) \le b(\|\mathbf{y}\|), \tag{11}$$

stability in theorem 1 is *uniform.*

(ii) Being weaker than the property $V(t, \mathbf{y}, \mathbf{z}) \le V^*(t, \mathbf{y})$, the property $V(t, \mathbf{y}, \mathbf{z}) \le b(\|\mathbf{y}\|)$ is more stringent than the property $V(t, \mathbf{0}, \mathbf{z}) \equiv 0$, which guarantees the stability of the partial-equilibrium position $\mathbf{y} = \mathbf{0}$ and $\mathbf{y}$-stability of the total equilibrium position $\mathbf{x} = \mathbf{0}$ [when conditions (4) are satisfied] only for *large* $\mathbf{z}_0$ [10, 12, 13] rather than for all $\mathbf{z}_0$.

(iii) When conditions (5) and (6) are satisfied, the system does not need to have the equilibrium position $\mathbf{x} = \mathbf{0}$.

Example 1. Let system (1) consist of the equations

$$\dot{y}_1 = -\frac{1}{2}y_1 - e^t y_1^2 \cos z_1, \qquad \dot{z}_1 = 2e^t y_1(2 + \sin z_1) - \cos z_1. \tag{12}$$

We introduce the auxiliary function

$$V(t, y_1, z_1) = e^t y_1^2 (2 + \sin z_1), \tag{13}$$

which satisfies the conditions

$$y_1^2 \le V(t, y_1, z_1) \le V^*(t, y_1) = 3e^t y_1^2, \qquad \dot{V} = -e^t y_1^2 \cos^2 z_1 \le 0$$

in region (2). According to theorem 1, the partial-equilibrium position $y_1 = 0$ of system (12) is stable. At the same time, system (12) does not admit the total-equilibrium position $y_1 = z_1 = 0$, and the function V specified by Eq. (13) does not satisfy conditions (11).

2. PARTIAL STABILITY OF PARTIAL-EQUILIBRIUM POSITIONS

For the problem of stability with respect to some of variables for the partial-equilibrium position $\mathbf{y} = \mathbf{0}$ of system (1), we introduce the notation $\mathbf{x} = (\mathbf{y}^t, \mathbf{z}^t)^t$ and $\mathbf{y} = (\mathbf{y}_1^t, \mathbf{y}_2^t)^t$. Let system (1) be continuous in the region

$$t \ge 0, \quad \|\mathbf{y}_1\| \le h, \quad \|\mathbf{y}_2\| < \infty, \quad \|\mathbf{z}\| < \infty, \tag{14}$$

its solution be unique and $(\mathbf{y}_2, \mathbf{z})$-extendable, and condition (3) be satisfied for system (1).

Definition 3. The partial-equilibrium position $\mathbf{y} = \mathbf{0}$ of the system of Eqs. (1) and (3) is

(i) $\mathbf{y}_1$-*stable* if, for any $\varepsilon > 0$ and $t_0 \geq 0$, there is $\delta(\varepsilon, t_0) > 0$ such that $\|\mathbf{y}_1(t; t_0, \mathbf{x}_0)\| < \varepsilon$ for all $t \geq t_0$, when $\|\mathbf{y}_0\| < \delta$ and $\|\mathbf{z}_0\| < \infty$;

(ii) *uniformly* $\mathbf{y}_1$-*stable* if δ is independent of t_0.

In what follows, we will consider that the function V is continuously differentiable and that the function V^* and vector function $\mathbf{W}(t, \mathbf{x})$ such that $\mathbf{W}(t, \mathbf{0}) \equiv \mathbf{0}$ are continuous in region (14).

Theorem 2. *Let there exist the scalar* V^* *and vector* $\mathbf{W}$ *functions that, in the region*

$$t \geq 0, \ \|\mathbf{y}_1\| + \|\mathbf{W}(t, \mathbf{x})\| \leq h, \ \|\mathbf{y}_2\| < \infty, \ \|\mathbf{z}\| < \infty \quad (15)$$

satisfy the conditions

$$V(t, \mathbf{y}_1, \mathbf{y}_2, \mathbf{z}) \geq a(\|\mathbf{y}_1\| + \|\mathbf{W}(t, \mathbf{x})\|), \quad \dot{V} \leq 0 \quad (16)$$

for system (1). *In this case, the partial-equilibrium position* $\mathbf{y} = \mathbf{0}$ *of the system of Eqs.* (1) *and* (3) *is* (i) $\mathbf{y}_1$-*stable if* $V \leq V^*(t, \mathbf{y})$ *and* (ii) *uniformly* $\mathbf{y}_1$-*stable if* $V \leq b(\|\mathbf{y}\|)$.

Proof. Since V, V^*, and b are continuous functions and satisfy the conditions $V(t, \mathbf{0}) \equiv V^*(t, \mathbf{0}) \equiv b(0) \equiv 0$, for any $\varepsilon > 0$ and $t_0 \geq 0$, there are (i) $\delta(\varepsilon, t_0) > 0$ and (ii) $\delta(\varepsilon) > 0$ such that, if $\|\mathbf{y}_0\| < \delta$ and $\|\mathbf{z}_0\| < \infty$, (i) $V(t_0, \mathbf{x}_0) \leq V^*(t_0, \mathbf{y}_0) < a(\varepsilon)$ and (ii) $V(t_0, \mathbf{x}_0) \leq b(\|\mathbf{y}_0\|) < a(\varepsilon)$, respectively. Using Eq. (7) and taking into account that $\dot{V} \leq 0$, we have Eqs. (10) and, in view of the properties of $a(r)$, conclude that, for any $\varepsilon > 0$ and $t_0 \geq 0$, $\|\mathbf{y}_1(t; t_0, \mathbf{x}_0)\| < \varepsilon$ for all $t \geq t_0$ in both cases, if $\|\mathbf{y}_0\| < \delta$ and $\|\mathbf{z}_0\| < \infty$. Q.E.D.

Discussion of theorem 2. (i) For $\mathbf{W} \equiv \mathbf{0}$, conditions (16) are replaced by the conditions

$$V(t, \mathbf{y}_1, \mathbf{y}_2, \mathbf{z}) \geq a(\|\mathbf{y}_1\|), \quad \dot{V} \leq 0 \quad (17)$$

in region (14). These conditions can be treated as a natural extension of Rumyantsev's classical conditions [1] for the stability of the equilibrium position $\mathbf{x} = \mathbf{0}$ of system (1) with respect to some of variables to the problem considered in this section.

(ii) For $\mathbf{W} \neq \mathbf{0}$, the introduction of the $\mathbf{W}$ function to the formulation of theorem 2 makes it possible to vary the region where the basic Lyapunov $\mathbf{V}$ function is constructed. We emphasize that the satisfaction of conditions (16) in region (15) does not generally mean the satisfaction of any of conditions (17) in region (14).

Example 2. Let system (1) consist of the equations

$$\begin{aligned} \dot{y}_1 &= -\frac{1}{2}(e^{-t} + 1)y_1 + \frac{1}{2}e^t y_2 y_3 \sin z_1, \\ \dot{y}_2 &= y_2^2 y_3 \sin z_1, \\ \dot{y}_3 &= -y_3 - (e^t y_1 + 1)y_3 \cos z_1, \\ \dot{z}_1 &= (e^t y_1 + 1)\sin z_1. \end{aligned} \quad (18)$$

We introduce the auxiliary functions

$$\begin{aligned} V(t, \mathbf{y}, z_1) &= e^t y_1^2 + \frac{1}{2}y_2^2 y_3^2 \sin^2 z_1, \quad W_1 = y_2 y_3 \sin z_1, \\ \mathbf{y} &= (y_1, y_2, y_3)^t, \quad \mathbf{y}_2 = (y_2, y_3)^t, \end{aligned} \quad (19)$$

which satisfy the conditions

$$y_1^2 + W_1^2 = V(t, \mathbf{y}, z_1) \leq V^*(t, \mathbf{y}) = e^t y_1^2 + \frac{1}{2}y_2^2 y_3^2,$$

$$\dot{V} = -y_1^2 + y_1 W_1 - W_1^2 + W_1^3 \leq 0$$

in region (15) for small h. According to the first part of Theorem 2, the partial-equilibrium position $\mathbf{y} = (y_1, y_2, y_3)^t = \mathbf{0}$ of system (18) is stable in y_1, although the derivative $\dot{V}$ of function (19) is alternating in region (14).

3. SOME MODIFICATIONS OF THE CONCEPTS OF PARTIAL STABILITY

We consider some modifications of the concepts of stability of the partial-equilibrium position $\mathbf{y} = \mathbf{0}$ of system (1) with respect to some of variables under the assumptions introduced in Section 2.

Definition 4. The partial-equilibrium position $\mathbf{y} = \mathbf{0}$ of the system of Eqs. (1) and (3) is

(i) $\mathbf{y}_1$-*stable for all* $\mathbf{y}_{20}$ if, for any $\varepsilon > 0$ and $t_0 \geq 0$, there is a $\delta(\varepsilon, t_0) > 0$ such that $\|\mathbf{y}_1(t; t_0, \mathbf{x}_0)\| < \varepsilon$ for all $t \geq t_0$, when $\|\mathbf{y}_{10}\| < \delta$, $\|\mathbf{y}_{20}\| < \infty$, and $\|\mathbf{z}_0\| < \infty$;

(ii) $\mathbf{y}_1$-*stable for large* $\mathbf{y}_{20}$ if, for any $\varepsilon > 0$, $t_0 \geq 0$, and $L > 0$, there is a $\delta(\varepsilon, t_0, L) > 0$ such that $\|\mathbf{y}_1(t; t_0, \mathbf{x}_0)\| < \varepsilon$ for all $t \geq t_0$, when $\|\mathbf{y}_{10}\| < \delta$, $\|\mathbf{y}_{20}\| < L$, and $\|\mathbf{z}_0\| < \infty$;

(iii) $\mathbf{y}_1$-*stable for large* $\mathbf{z}_0$ if, for any $\varepsilon > 0$, $t_0 \geq 0$, and $L > 0$, there is a $\delta(\varepsilon, t_0, L) > 0$ such that $\|\mathbf{y}_1(t; t_0, \mathbf{x}_0)\| < \varepsilon$ for all $t \geq t_0$, when $\|\mathbf{y}_0\| < \delta$ and $\|\mathbf{z}_0\| < L$;

(iv) $\mathbf{y}_1$-*stable for all* $\mathbf{y}_{20}$ *and large* $\mathbf{z}_0$ if, for any $\varepsilon > 0$, $t_0 \geq 0$, and $L > 0$, there is a $\delta(\varepsilon, t_0, L) > 0$ such that $\|\mathbf{y}_1(t; t_0, \mathbf{x}_0)\| < \varepsilon$ for all $t \geq t_0$, when $\|\mathbf{y}_{10}\| < \delta$, $\|\mathbf{y}_{20}\| < \infty$, and $\|\mathbf{z}_0\| < L$;

(v) $\mathbf{y}_1$-*stable for large* $\mathbf{y}_{20}$ *and* $\mathbf{z}_0$ if, for any $\varepsilon > 0$, $t_0 \geq 0$, and $L > 0$, there is a $\delta(\varepsilon, t_0, L) > 0$ such that $\|\mathbf{y}_1(t; t_0, \mathbf{x}_0)\| < \varepsilon$ for all $t \geq t_0$, when $\|\mathbf{y}_{10}\| < \delta$, $\|\mathbf{y}_{20}\| < L$, and $\|\mathbf{z}_0\| < L$.

Theorem 3. *Let there exist functions* V *and* V^* *such that conditions* (17) *for system* (1) *are satisfied in region* (14). *In this case, the partial-equilibrium position* $\mathbf{y} = \mathbf{0}$ *of system* (1) *is* $\mathbf{y}_1$-*stable*

(i) *for all* $\mathbf{y}_{20}$ *if the condition*

$$V(t, \mathbf{y}_1, \mathbf{y}_2, \mathbf{z}) \leq V^*(t, \mathbf{y}_1) \quad (20)$$

is valid in region (14);

(ii) *for large* $\mathbf{y}_{20}$ *if*

$$V(t, \mathbf{y}_1, \mathbf{y}_2, \mathbf{z}) \leq V^*(t, \mathbf{y}_1, \mathbf{y}_2), \quad V^*(t, \mathbf{0}, \mathbf{y}_2) \equiv 0; \quad (21)$$

(iii) *for large* $\mathbf{z}_0$ *if*

$$V(t, \mathbf{0}, \mathbf{0}, \mathbf{z}) \equiv 0; \quad (22)$$

(iv) *for all* $\mathbf{y}_{20}$ *and large* $\mathbf{z}_0$ *if*

$$V(t, \mathbf{y}_1, \mathbf{y}_2, \mathbf{z}) \le V^*(t, \mathbf{y}_1, \mathbf{z}), \quad V^*(t, \mathbf{0}, \mathbf{z}) \equiv 0; \quad (23)$$

(v) *for large* $\mathbf{y}_{20}$ *and* $\mathbf{z}_0$ *if*

$$V(t, \mathbf{0}, \mathbf{y}_2, \mathbf{z}) \equiv 0. \quad (24)$$

In cases (i), (ii), (iv), *and* (v), *system* (1) *also has the partial-equilibrium position* $\mathbf{y}_1 = 0$, *which is stable* (i) *for all* $\mathbf{y}_{20}$ *and* $\mathbf{z}_0$, (ii) *for large* $\mathbf{y}_{20}$ *and all* $\mathbf{z}_0$, (iv) *for all* $\mathbf{y}_{20}$ *and large* $\mathbf{z}_0$, *and* (v) *for large* $\mathbf{y}_{20}$ *and* $\mathbf{z}_0$, *respectively.*

Proof. Since V and V^* are continuous functions and satisfy the conditions $V(t, \mathbf{0}) \equiv V^*(t, \mathbf{0}) \equiv 0$, and conditions (20)–(24) are valid for cases (i)–(v), respectively, for any $\varepsilon > 0$ and $t_0 \ge 0$ [and any $L > 0$ for cases (ii)–(v)], there is [for case (i)] $\delta(\varepsilon, t_0) > 0$ and [for cases (ii)–(v)] a 0 ($\delta(\varepsilon, t_0, L) > 0$ such that $V(t_0, \mathbf{x}_0) < a(\varepsilon)$ if

$$\|\mathbf{y}_{10}\| < \delta, \quad \|\mathbf{y}_{20}\| < \infty, \quad \|\mathbf{z}_0\| < \infty, \quad (25)$$

$$\|\mathbf{y}_{10}\| < \delta, \quad \|\mathbf{y}_{20}\| < L, \quad \|\mathbf{z}_0\| < \infty, \quad (26)$$

$$\|\mathbf{y}_{10}\| < \delta, \quad \|\mathbf{y}_{20}\| < \delta, \quad \|\mathbf{z}_0\| < L, \quad (27)$$

$$\|\mathbf{y}_{10}\| < \delta, \quad \|\mathbf{y}_{20}\| < \infty, \quad \|\mathbf{z}_0\| < L, \quad (28)$$

$$\|\mathbf{y}_{10}\| < \delta, \quad \|\mathbf{y}_{20}\| < L, \quad \|\mathbf{z}_0\| < L, \quad (29)$$

for cases (i)–(v), respectively. Using Eq. (7) and taking into account that $\dot{V} \le 0$, we have Eqs. (10) and, in view of the properties of $a(r)$, conclude that, for any $\varepsilon > 0$ and $t_0 \ge 0$ [and any $L > 0$ for cases (ii)–(v)], $\|\mathbf{y}_1(t; t_0, \mathbf{x}_0)\| < \varepsilon$ for all $t \ge t_0$ when corresponding conditions (25)–(29) are satisfied.

The existence of the partial-equilibrium position $\mathbf{y}_1 = \mathbf{0}$ for cases (i), (ii), (iv), and (v), as well as its stability (of the corresponding types), is proven similarly to the proof of Theorem 1. Q.E.D.

4. PARTIAL ASYMPTOTIC STABILITY OF PARTIAL-EQUILIBRIUM POSITIONS

We accept the assumptions introduced in Section 2.

Definition 5. The partial-equilibrium position $\mathbf{y} = \mathbf{0}$ of the systems of Eqs. (1) and (3) is *uniformly asymptotically* $\mathbf{y}_1$*-stable* if it is uniformly $\mathbf{y}_1$-stable in the sense of Definition 1 and there is a $\Delta > 0$ such that the relation

$$\lim \|\mathbf{y}_1(t; t_0, \mathbf{x}_0)\| \to 0, \quad t \to \infty, \quad (30)$$

is satisfied uniformly in t_0 and $\mathbf{x}_0$ for any solution of the system of Eqs. (1) and (3) with $\|\mathbf{y}_0\| < \Delta$ and $\|\mathbf{z}_0\| < \infty$;

(ii) *uniformly asymptotically* $\mathbf{y}_1$*-stable for large* $\mathbf{z}_0$ if it is uniformly $\mathbf{y}_1$-stable for large $\mathbf{z}_0$ in the sense of Definition 4 (where δ is independent of t_0) and there is a $\Delta(L) > 0$ such that relation (30) is satisfied uniformly in t_0 and $\mathbf{x}_0$ for any solution of the systems of Eqs. (1) and (3) with $\|\mathbf{y}_0\| < \Delta$ and $\|\mathbf{z}_0\| < L$.

In addition to the functions V and $\mathbf{W}$, we consider the functions $c(r)$ and $d(r)$ similar to $a(r)$ and the vector function $\mathbf{U}(\mathbf{x})$, which is continuous in region (14) and satisfies the relation $\mathbf{U}(\mathbf{0}) \equiv \mathbf{0}$.

Theorem 4. *Let there exist scalar function* V *and two vector functions* $\mathbf{W}$ *and* $\mathbf{U}$ *that satisfy the conditions*

$$a(\|\mathbf{y}_1\| + \|\mathbf{W}(t, \mathbf{x})\|) \le V(t, \mathbf{y}_1, \mathbf{y}_2, \mathbf{z}) \le b(\|\mathbf{y}_1\| + \|\mathbf{U}(\mathbf{x})\|), \quad (31)$$

$$\dot{V} \le -c(\|\mathbf{y}_1\| + \|\mathbf{U}(\mathbf{x})\|)$$

in region (15). *In this case, the partial-equilibrium position* $\mathbf{y} = \mathbf{0}$ *is* (i) *uniformly asymptotically* $\mathbf{y}_1$*-stable if* $V \le d(\|\mathbf{y}\|)$ *and* (ii) *uniformly asymptotically* $\mathbf{y}_1$*-stable for large* $\mathbf{z}_0$ *if* $V(t, \mathbf{0}, \mathbf{0}, \mathbf{z}) \equiv 0$.

Proof. Uniform $\mathbf{y}_1$-stability for case (i) follows from Theorem 2. Uniform $\mathbf{y}_1$-stability for large $\mathbf{z}_0$ for case (ii) is proven similarly to the proof of the third part of Theorem 3 by taking into account the fact that $V \le b(\|\mathbf{x}\|)$ under conditions (31).

Let us prove that relations (30) are uniformly satisfied: for some $\Delta > 0$ [and for any given $L > 0$ in case (ii)] and any $\varepsilon > 0$, there is (i) $T(\varepsilon) > 0$ or (ii) $T(\varepsilon, L) > 0$ such that $\|\mathbf{y}_1(t; t_0, \mathbf{x}_0)\| < \varepsilon$ for all $t \ge t_0 + T$, when $t_0 \ge 0$, $\|\mathbf{y}_0\| < \Delta$, and $\|\mathbf{z}_0\| <$ (i) ∞ or (ii) L.

Since (i) $V \le b(\|\mathbf{y}_1\| + \|\mathbf{U}(\mathbf{x})\|)$ and $V \le d(\|\mathbf{y}\|)$ or (ii) $V(t, \mathbf{0}, \mathbf{0}, \mathbf{z}) \equiv 0$, there is (i) a $\Delta > 0$ or (ii) a $\Delta(L) > 0$ such that $\|\mathbf{y}_{10}\| + \|\mathbf{U}(\mathbf{x}_0)\|) < b^{-1}(a(h))$ when $\|\mathbf{y}_0\| < \Delta$ and $\|\mathbf{z}_0\| <$ (i) ∞ or (ii) L. This Δ value is taken to prove the uniform satisfaction of relation (30).

If $t_0 \ge 0$, $\|\mathbf{y}_0\| < \Delta$, and $\|\mathbf{z}_0\| <$ (i) ∞ or (ii) L, we have

$$a(\|\mathbf{y}_1(t; t_0, \mathbf{x}_0)\| + \|\mathbf{W}(t; \mathbf{x}(t; t_0, \mathbf{x}_0))\|)$$

$$\le Vt, \mathbf{x}, (t; (t_0, \mathbf{x}_0)) \le V(t_0, \mathbf{x}_0) \le b(\|\mathbf{y}_{10}\| + \|\mathbf{U}(\mathbf{x}_0)\|)$$

$$< b(b^{-1}(a(h))) = a(h)$$

because $V \le b(\|\mathbf{y}_1\| + \|\mathbf{U}(\mathbf{x})\|)$ and $\dot{V} \le 0$. Therefore,

$$\|\mathbf{y}_1(t; t_0, \mathbf{x}_0)\| + \|\mathbf{W}(t; \mathbf{x}(t; t_0, \mathbf{x}_0))\| < h$$

for $t \ge t_0$. Let $0 < \varepsilon < \Delta$. We denote

$$T(\varepsilon) = [a(h) - a(\varepsilon)]c^{-1}(b^{-1}(a(\varepsilon)))$$

and demonstrate that $V(t_*, \mathbf{x}(t_*; t_0, \mathbf{x}_0)) < a(\varepsilon)$ for a certain $t_* \in (t_0, t_0 + T)$. Indeed, otherwise we have

$$a(\varepsilon) \le V(t, \mathbf{x}(t; t_0, \mathbf{x}_0)) \le b(\|\mathbf{y}_1(t; t_0, \mathbf{x}_0)\| + \|\mathbf{U}(\mathbf{x}(t; t_0, \mathbf{x}_0))\|)$$

for $t_* \in (t_0, t_0 + T)$ and therefore,

$$\|\mathbf{y}_1(t; t_0, \mathbf{x}_0)\| + \|\mathbf{U}(\mathbf{x}(t; t_0, \mathbf{x}))\| \geq b^{-1}(a(\varepsilon))$$

for the same t. If this is the case,

$$a(\varepsilon) \leq V(t_0 + T, \mathbf{x}(t_0 + T; t_0, \mathbf{x}_0)) \leq V(t_0, \mathbf{x}_0)$$

$$-c(b^{-1}(a(\varepsilon)))T \leq a(h) - c(b^{-1}(a(\varepsilon)))T < a(\varepsilon),$$

which is impossible. Therefore, the existence of t_* has been proven.

Since $\dot{V} \leq 0$, we have

$$a(\|\mathbf{y}_1(t; t_0, \mathbf{x}_0)\| + \|\mathbf{W}(t; \mathbf{x}(t; t_0, \mathbf{x}_0))\|) \leq V(t_*, \mathbf{x}(t_*; t_0, \mathbf{x}_0)) < a(\varepsilon)$$

for $t \geq t^*$ and therefore $\|\mathbf{y}_1(t; t_0, \mathbf{x}_0)\| < \varepsilon$ for $t \geq t_0 + T > t_*$ if $t_0 \geq 0$, $\|\mathbf{y}_0\| < \Delta$, and $\|\mathbf{z}_0\| <$ (i) ∞ or (ii) L. Q.E.D.

Discussion of Theorem 4. (i) When $\mathbf{W} \equiv \mathbf{0}$ and $\mathbf{U} = \mathbf{y}_2^*$ ($\mathbf{y}_2^*$ involves all $\mathbf{y}_2$ components or some of them), conditions (31) are replaced by the conditions

$$a(\|\mathbf{y}_1\|) \leq V(t, \mathbf{y}, \mathbf{z}) \leq b(\|\mathbf{y}_1\| + \|\mathbf{y}_2^*\|), \quad \dot{V} \leq -c(\|\mathbf{y}_1\| + \|\mathbf{y}_2^*\|) \tag{32}$$

in region (14). These conditions can be treated as a natural transfer of Rumyantsev's classical conditions [1, 5] for stability with respect to some of variables to the problem under consideration.

(ii) For $\mathbf{W} \neq \mathbf{0}$, the satisfaction of conditions (31) in region (15) does not generally mean the satisfaction of conditions (32) in region (14), and the function $\dot{V}$ can be alternating in region (14).

Example 3. Let a system (1) consist of the equations

$$\dot{y}_1 = -y_1 + y_2 y_3 \sin z_1, \quad \dot{y}_2 = y_2^2 y_3 \sin z_1,$$

$$\dot{y}_3 = -y_3 - (e^t y_1 + 1) y_3 \cos z_1, \tag{33}$$

$$\dot{z}_1 = (e^t y_1 + 1)\sin z_1.$$

We introduce the auxiliary functions

$$V(\mathbf{y}, z_1) = \frac{1}{2}(y_1^2 + y_2^2 y_3^2 \sin^2 z_1),$$

$$W_1 = U_1 = y_2 y_3 \sin z_1,$$

which satisfy the conditions

$$V(y, \mathbf{z}_1) = y_1^2 + W_1^2 = y_1^2 + U_1^2,$$

$$V(\mathbf{y}, z_1) \leq d(\|\mathbf{y}\|),$$

$$\dot{V} = -y_1^2 + y_1 U_1 - U_1^2 + U_1^3 \leq -\gamma(y_1^2 + U_1^2),$$

$$\gamma = \text{const} > 0$$

in region (15) for small h. According to Theorem 4, the partial-equilibrium position $\mathbf{y} = (y_1, y_2, y_3)^t = \mathbf{0}$ of system (33) is uniformly asymptotically stable in $\mathbf{y}_1$, although the derivative $\dot{V}$ is alternating in region (14).

ACKNOWLEDGMENTS

This work was supported by the Russian Foundation for Basic Research and by the Ministry of Education of the Russian Federation.

REFERENCES

1. V. V. Rumyantsev, Vestn. Mosk. Univ., Ser. Mat. Mekh. Fiz. Astron. Khim., No. 4, 9 (1957).
2. C. Corduneanu, Rev. Roum. Math. Pures Appl. **9** (3), 229 (1964).
3. A. Halanay, *Differential Equations: Stability, Oscillations, Time-Lags* (Academic, New York, 1966).
4. K. Peiffer and N. Rouche, J. Mec. **8** (2), 323 (1969).
5. V. V. Rumyantsev and A. S. Oziraner, *Stability and Stabilization of Motion Related with Respect to Some of Variables* (Nauka, Moscow, 1987).
6. L. Hatvani, Alkalm. Mat. Lap. **15** (1/2), 1 (1990/1991).
7. A. S. Andreev, Prikl. Mat. Mekh. **54** (4), 539 (1991).
8. V. I. Vorotnikov, Avtom. Telemekh. **54** (3), 3 (1993).
9. M. M. Khapaev, *Averaging in Stability Theory* (Kluwer, Dordrecht, 1993).
10. V. I. Vorotnikov, *Partial Stability and Control* (Birkhauser, Boston, 1998).
11. A. L. Fradkov, I. V. Miroshnik, and V. O. Nikiforov, *Nonlinear and Adaptive Control of Complex Systems* (Kluwer, Dordrecht, 1999).
12. V. I. Vorotnikov and V. V. Rumyantsev, *Stability and Control in Some Coordinates of the Phase Vector of Dynamic Systems: Theory, Methods, and Applications* (Nauchnyi Mir, Moscow, 2001).
13. V. I. Vorotnikov, Dokl. Akad. Nauk **384** (1), 47 (2002).
14. A. N. Michel, A. P. Molchanov, and Y. Sun, Nonlinear Anal.: TMA **52** (4), 1295 (2003).
15. E. D. Sontag and Y. Wang, Syst. Control. Lett. **38** (4/5), 235 (1999).

Translated by R. Tyapaev

Doklady Physics, Vol. 48, No. 3, 2003, pp. 156–158. Translated from Doklady Akademii Nauk, Vol. 389, No. 3, 2003, pp. 338–340.

MECHANICS

Two Integrable Systems on a Two-Dimensional Sphere

I. S. Mamaev

Presented by Academician V.V. Kozlov November 19, 2002

Received December 2, 2002

GENERALIZED EULER PROBLEM FOR TWO CENTERS

As was shown in [1], an integrable analogue of the plane Euler problem of particle motion in the field of two fixed Newtonian centers can be formulated on a two-dimensional sphere S^2. Integrability was proved by the method of separation of variables. The integrability of this problem in the three-dimensional case, i.e., for a particle moving on a three-dimensional sphere S^3, was proven in [2]. The proof consists of the elimination of a cyclic variable so that the three-dimensional problem on S^3 reduces to a two-dimensional problem on S^2. But in this case an additional Hookean center originates at the pole on the perpendicular to the equatorial plane of the two centers. In this paper, we explicitly write out algebraic integrals in the more general case of a material point moving in the field of two Newtonian centers and three Hookean centers placed on mutually orthogonal axes so that two of the Hookean centers lie on the plane of the Newtonian centers and the third one on the perpendicular to this plane (see Fig. 1).

In order to write out the integrals, we use the well-known analogy to rigid-body dynamics to introduce corresponding variables $\mathbf{M}$, $\gamma \in \mathbb{R}^3$, which are analogues of the angular moment vector and vertical unit vector, respectively.

Indeed, in terms of $\mathbf{M} = \mathbf{p} \times \mathbf{q}$ and $\boldsymbol{\gamma} = \mathbf{q}$, where $\mathbf{p} = (p_1, p_2, p_3)$ and $\mathbf{q} = (q_1, q_2, q_3)$ are the canonical momentum and coordinates of a point on the sphere $|\mathbf{q}|^2 = 1$, respectively, the equations of motion for an arbitrary potential $V(\mathbf{q}) \equiv V(\gamma)$ can be represented as Hamilton equations with the Poisson bracket determined by the algebra $e(3) = so(3) \oplus_s \mathbb{R}^3$:

$$\{M_i, M_j\} = \varepsilon_{ijk} M_k, \quad \{M_i, \gamma_j\} = \varepsilon_{ijk}\gamma_k, \quad \{\gamma_i, \gamma_j\} = 0. \tag{1}$$

The corresponding Hamiltonian is

$$H = \frac{1}{2}(\mathbf{M}, \mathbf{M}) + V(\boldsymbol{\gamma}). \tag{2}$$

The equations determined by Poisson bracket (1) and Hamiltonian (2) coincide with the equations of motion of a spherical top in the potential $V(\gamma)$. Poisson bracket (1) is degenerate and has the two Casimir functions $F_1 = (\mathbf{M}, \boldsymbol{\gamma}) = c_1$ and $F_2 = (\boldsymbol{\gamma}, \boldsymbol{\gamma}) = 1$. For our purposes, the condition $(\mathbf{M}, \boldsymbol{\gamma}) = 0$ must be satisfied; i.e., only a particular integral must be found.

Omitting the physical justifications of the possibility of extending Newtonian and Hookean potentials to the case of a sphere (see [2]), we write out the above-mentioned potential of two Newtonian and three Hookean centers in the form

$$U = -\mu_1 \cot\theta_1 - \mu_2 \cot\theta_1 + \frac{1}{2}\left(\frac{c_1}{\gamma_1^2} + \frac{c_2}{\gamma_2^2} + \frac{c_3}{\gamma_3^2}\right). \tag{3}$$

Here, μ_1 and μ_2 are constants for the Newtonian centers; c_1, c_2, and c_3 are constants for the Hookean centers; and θ_i is the angle between the radius vector of the

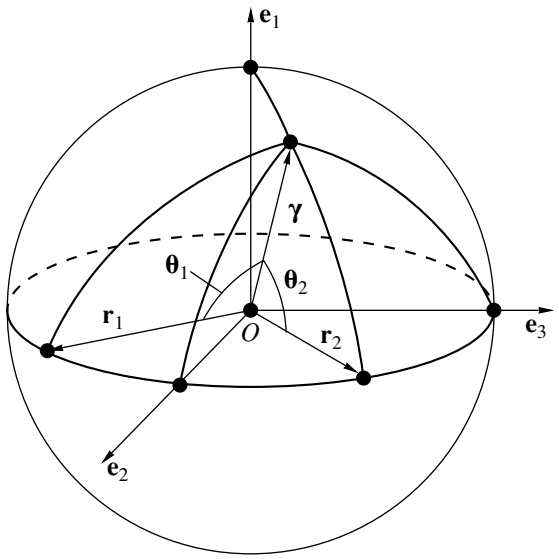

Fig. 1.

Udmurt State University, Izhevsk, 426069 Russia
e-mail: mamaev@rcd.ru

1028-3358/03/4803-0156$24.00

particle and that of the *i*th center. Assuming the Newtonian centers to be at the points $\mathbf{r}_1 = (0, \alpha, \beta)$ and $\mathbf{r}_2 = (0, -\alpha, \beta)$ and introducing an additional Neumann-type potential on the sphere, we find that the following quadratic (in $\mathbf{M}$) functions commute [i.e., $\{H, F\} = 0$] on the level determined by the condition $(\mathbf{M}, \boldsymbol{\gamma}) = 0$:

$$H = \frac{1}{2}\mathbf{M}^2 - \mu_1\frac{\beta\gamma_3 + \alpha\gamma_2}{\sqrt{\gamma_1^2 + \beta^2\gamma_2^2 + \alpha^2\gamma_3^2 - 2\alpha\beta\gamma_2\gamma_3}}$$

$$-\mu_2\frac{\beta\gamma_3 - \alpha\gamma_2}{\sqrt{\gamma_1^2 + \beta^2\gamma_2^2 + \alpha^2\gamma_3^2 + 2\alpha\beta\gamma_2\gamma_3}} + \frac{1}{2}c_1\frac{\gamma_2^2 + \gamma_3^2}{\gamma_1^2} \quad (4)$$

$$+\frac{1}{2}c_2\frac{\gamma_1^2 + \gamma_3^2}{\gamma_2^2} + \frac{1}{2}c_3\frac{\gamma_1^2 + \gamma_2^2}{\gamma_3^2} + C(\alpha^2\gamma_2^2 - \beta^2\gamma_3^2),$$

$$F = \alpha^2 M_2^2 - \beta^2 M_3^2 + 2\alpha\beta(V_1 - V_2)$$

$$-\frac{c_1}{\gamma_1^2}(\beta^2\gamma_2^2 - \alpha^2\gamma_3^2) - \frac{c_2}{\gamma_2^2}\beta^2\gamma_1^2 + \frac{c_3}{\gamma_3^2}\alpha^2\gamma_1^2 + 2C\alpha^2\beta^2\gamma_1^2.$$

Here, μ_1, μ_2, α, β, c_1, c_2, c_3, and C are constants and

$$V_1 = \frac{\mu_1(\beta\gamma_2 + \alpha\gamma_3)}{\sqrt{\gamma_1^2 + \beta^2\gamma_2^2 + \alpha^2\gamma_3^2 - 2\alpha\beta\gamma_2\gamma_3}},$$
$$V_2 = \frac{\mu_2(\beta\gamma_2 - \alpha\gamma_3)}{\sqrt{\gamma_1^2 + \beta^2\gamma_2^2 + \alpha^2\gamma_3^2 + 2\alpha\beta\gamma_2\gamma_3}}. \quad (5)$$

The function H is a Hamiltonian, and the function F is an additional quadratic integral. In this case, the system under consideration is of the Liouville type and can be integrated in spheroconical coordinates [1, 2]. It is worth noting that finding integrals (4) in an algebraic form is a tricky problem that involves the inversion of a spheroconical transformation.

PROBLEM OF *n* HOOKEAN CENTERS ON A SPHERE

We now present a new integrable case of the problem of particle motion in the field of Hookean potentials $\frac{c_i}{(\boldsymbol{\gamma}, \mathbf{r}_i)^2}$. In this case, the Hookean attracting centers $\mathbf{r}_i$ ($i = 1, 2, \ldots, n$) are placed arbitrarily over the equator rather than positioned on mutually orthogonal axes. For the sake of simplicity, we consider the case of a two-dimensional sphere S^2. In this case, the Hamiltonian and additional integral [for $(\mathbf{M}, \boldsymbol{\gamma}) = 0$] take the form

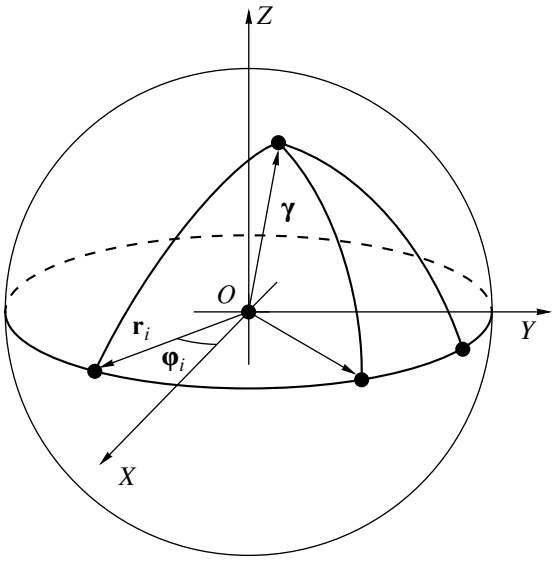

Fig. 2.

$$H = \frac{1}{2}\mathbf{M}^2 + \frac{1}{2}\sum_{i=1}^{n}\frac{c_i}{(\mathbf{r}_i, \boldsymbol{\gamma})^2} + U(\gamma_3),$$
$$F = M_3^2 + (1 - \gamma_3^2)\sum_{i=1}^{n}\frac{c_i}{(\mathbf{r}_i, \boldsymbol{\gamma})^2}. \quad (6)$$

An arbitrary function $U(\gamma_3)$ in Eqs. (6) corresponds to an arbitrary central field, whose center is on the perpendicular to the plane of the Hookean centers (see Fig. 2). In particular, one more Hookean center can be placed at the pole. In this case, as follows from [2], the three-dimensional problem of particle motion in the field of n Hookean centers placed on the equator of a sphere S^3 is also integrable.

In Euclidean space, the problem under consideration is trivial, because variables can be separated even in Cartesian coordinates for arbitrary arrangements of Hookean centers (the problem reduces to the problem of n coupled linear oscillators). In a curved space, even for a two-dimensional sphere, the problem of motion in the field of three arbitrarily positioned Hookean centers is nonintegrable. This statement was not proven strictly, but relevant numerical simulations showed a chaotic motion. The other quadratic integral of motion F presented in Eqs. (6) appears due to the separation of the variables of the problem in spherical coordinates (θ, φ). Indeed, the Hamiltonian H can be written in the form

$$H = \frac{1}{2}\left(p_\theta^2 + \frac{p_\varphi^2}{\sin^2\theta}\right) + \frac{1}{2}\sum_{i=1}^{n}\frac{c_i}{\sin^2\theta\cos^2(\varphi - \varphi_i)}$$

$$+ U(\theta) = \frac{1}{2}p_\theta^2 \qquad (7)$$

$$+ \frac{1}{2\sin^2\theta}\left[p_\varphi^2 + \sum_{i=1}^{n}\frac{c_i}{\cos^2(\varphi - \varphi_i)}\right] + U(\theta),$$

where θ and φ are the spherical coordinates of a moving material point and φ_i is the angular coordinate of the ith Hookean center on the equator (Fig. 2). The expression in square brackets is an additional integral of motion presented in Eqs. (6). It is worth noting that the problem under consideration is nonintegrable if the Hookean centers (for $n > 2$) are off of a great circle (e.g., on a parallel) of the sphere.

ACKNOWLEDGMENTS

I am grateful to A.V. Borisov for his attention to this work and stimulating discussions.

REFERENCES

1. V. V. Kozlov and A. O. Harin, Celest. Mech. Dyn. Astron. **54**, 393 (1992).
2. A. V. Borisov and I. S. Mamaev, *Poisson Structures and Lee Algebras in Hamiltonian Mechanics* (Izd. RKhD, Izhevsk, 1999).

Translated by V. Chechin